**T.R.**

**GEBZE TECHNICAL UNIVERSITY**

**GRADUATE SCHOOL OF NATURAL AND APPLIED SCIENCES**

# DESIGN AND OPTIMIZATION OF HIGH VOLTAGE TRANSFORMERS FOR LLC CONVERTER

**UMUT ÖNDİN**

**A THESIS SUBMITTED FOR THE DEGREE OF**

**DOCTOR OF PHILOSOPHY**

**DEPARTMENT OF ELECTRONICS ENGINEERING**

**GEBZE**

**2023**

**T.R.**

**GEBZE TECHNICAL UNIVERSITY**

**GRADUATE SCHOOL OF NATURAL AND APPLIED SCIENCES**

# DESIGN AND OPTIMIZATION OF HIGH VOLTAGE TRANSFORMERS FOR LLC CONVERTER

**UMUT ÖNDİN**

**A THESIS SUBMITTED FOR THE DEGREE OF DOCTOR OF PHILOSOPHY**

**DEPARTMENT OF ELECTRONICS ENGINEERING**

THESIS SUPERVISOR

PROF. DR. ABDULKADİR BALIKÇI

**GEBZE**

**2023**

**T.C.**
**GEBZE TEKNİK ÜNİVERSİTESİ**
**FEN BİLİMLERİ ENSTİTÜSÜ**

# LLC DÖNÜŞTÜCÜLER İÇİN YÜKSEK GERİLİM TRANSFORMATÖRLERİNİN TASARIMI VE OPTİMİZASYONU

**UMUT ÖNDİN**

**DOKTORA TEZİ**
**ELEKTRONİK MÜHENDİSLİĞİ ANABİLİM DALI**

DANIŞMANI
PROF. DR. ABDULKADİR BALIKÇI

**GEBZE**
**2023**

| | |
|---|---|
| GEBZE TEKNİK ÜNİVERSİTESİ | **DOKTORA JÜRİ ONAY FORMU** |

GTÜ Fen Bilimleri Enstitüsü Yönetim Kurulu'nun 07/02/2023 tarih ve 2023/11 sayılı kararıyla oluşturulan jüri tarafından 20/3/2023 tarihinde tez savunma sınavı yapılan UMUT ÖNDİN'in tez çalışması Elektronik Mühendisliği Anabilim Dalında DOKTORA tezi olarak kabul edilmiştir.

**JÜRİ**

| | |
|---|---|
| ÜYE (TEZ DANIŞMANI) | : Prof. Dr. Abdulkadir BALIKÇI |
| ÜYE | : Prof.Dr. M.Hakan HOCAOĞLU |
| ÜYE | : Prof.Dr. A.Faruk BAKAN |
| ÜYE | : Dr. Öğr. Üyesi Tuba GÖZEL |
| ÜYE | : Doç. Dr. YUNUS UZUN |

**ONAY**

Gebze Teknik Üniversitesi ……. Enstitüsü Yönetim Kurulu'nun ……/……./...…. tarih ve …..…/…..... sayılı kararı.

# SUMMARY

A particular application of resonant converters is high-voltage DC-DC applications. The high-voltage DC-DC converters include a high-voltage transformer with high values of non-ideal elements, such as parasitic capacitances, due to the high turn ratio of the transformer. The high value of winding capacitances affects the selection of the resonant topology.

LLC resonant converter contains very high sensitivity to transformer parasitic capacitances. Therefore, the LLC resonant converter is limited to high-voltage applications. Using an LLC resonant converter in high-voltage applications is possible by reducing the effects and values of the main parasitic element.

This thesis proposes to decrease parasitic capacitance on high-voltage transformers using a multi-winding transformer with a winding arrangement, minimise the arrangement's influence on winding losses and test a proposed winding arrangement with an LLC resonant converter.

The comparative experimental analyses are performed for the proposed multi-winding transformer and the multi-layer transformer designed in the same geometry. The result of the measurement shows that the transfomer parasitic capacitance is significantly reduced by proposed multi-winding transformer. The experimental analyses are performed using the proposed multi-winding transformer with an integrated rectifier in the LLC resonant converter. The experimental results indicate that the LLC resonant converter is suitable for high-voltage applications due to the minimized parasitic capacitances of the high-voltage transformer, which enhances its reliability. The experimental results indicate that the output voltage regulation is provided under any load conditions in a wide operating range, and the LLC resonant converter works in accordance with FHA in high-voltage application.

**Key Words: High-voltage Transformers, Parasitic Capacitance, Resonant Power Conversion, Transformer Model, Multi-winding Transformer.**

# ÖZET

Rezonans dönüştürücülerin özel bir uygulaması, yüksek gerilim DC-DC uygulamalarıdır. Yüksek gerilim DC-DC dönüştürücüleri, transformatörün yüksek dönüş oranı nedeniyle parazitik kapasitanslar gibi ideal olmayan elemanların yüksek değerlerine sahip bir yüksek gerilim transformatörü içerir. Parazitik kapasitanslarının yüksek değeri, rezonans topolojisinin seçimini etki etmektedir.

LLC rezonans dönüştürücü, transformatörün parazitik kapasitanslarına karşı çok yüksek hassasiyet içerir. Bu nedenle, yüksek gerilim uygulamalarında LLC rezonans dönüştürücü kullanımı sınırlıdır. Yüksek gerilim uygulamalarında bir LLC rezonans dönüştürücü kullanımı ancak ana parazitik elemanların etkilerini ve değerlerini azaltmakla mümkündür.

Bu tez, sargı düzenlemesi ile çok sargılı bir transformatör kullanarak yüksek gerilim transformatörlerindeki parazitik kapasitansları azaltmayı, düzenlemenin sargı kayıpları üzerindeki etkisini en aza indirmeyi ve önerilen bir sargı düzenlemesini LLC rezonans dönüştürücü ile yüksek gerilim uygulamasında kullanmayı önermektedir.

Önerilen çok sargılı transformatör ve aynı geometride tasarlanan çok katmanlı transformatör için karşılaştırmalı deneysel analizler yapılmıştır. Ölçümün sonucu, önerilen çok sargılı trafo tarafından trafo parazitik kapasitansının önemli ölçüde azaldığını göstermektedir. Deneysel analizler, LLC rezonans dönüştürücüde entegre bir doğrultucu ile önerilen çok sargılı transformatör kullanılarak deneysel analizler gerçekleştirilir. Deneysel sonuçlar, LLC rezonans dönüştürücünün, yüksek gerilim transformatörünün güvenilirliğini artıran azaltılmış parazit kapasitansları nedeniyle yüksek gerilim uygulamaları için uygun olduğunu göstermektedir. Deneysel sonuçlar, çıkış gerilim regülasyonunun her türlü yük koşulunda sağlandığını, LLC rezonans dönüştürücünün yüksek gerilim uygulmasında FHA'ya uygun olarak çalıştığı görülmektedir.

**Anahtar Kelimeler: Yüksek Gerilim Transformatörü, Parasitik Kondansatör, Rezonanat Güç Dönüştürücü, Transformatör Modeli, Çok Sargılı Transformatör.**

# ACKNOWLEDGEMENTS

I would like to express my deep gratitude to my supervisor and research guide, Prof. Dr. Abdulkadir BALIKÇI, for his support, immense knowledge, motivation and obviously patience. His suggestions and valuable supervision helped me in all the time of this research.

Besides my advisor, I would like to thank the rest of my thesis committee, Prof. Dr. M. Hakan HOCAOĞLU, for his sincere counsel and guidance, and Prof. Dr. A. Faruk BAKAN, for his insightful comments and encouragement. Also, I offer my sincere appreciation for the learning opportunities provided by Assoc. Prof. Dr. Uğur HASIRCI.

I thank to my fellow colleagues and friends, Türev SARIKURT, Ceyhun SEZENOĞLU, Murat CEYLAN and Ali SARI, whom I gained a lot from, through their personal and scholarly interactions, their recommendations and our constructive discussions. I also thank to all the lab mates in Power Systems Laboratory.

I owe a lot to my parents, who encouraged and helped me at every stage of my life, and I longed to see this achievement come true. I thank them for their persistent support and prayers.

Finally, I want to thank my wife, Funda ÖNDİN, for the inspiration she has been to me through her perspective on life and for her love and support. And I want to thank my daughters, Erva Meryem ÖNDİN and Azra Betül ÖNDİN, for their love and prayers.

# TABLE of CONTENTS

# LIST of ABBREVIATIONS AND ACRONYMS

| Abbreviations and Acronyms | | Explanations |
|---|---|---|
| $A_t$ | : | The parallel surface area |
| $A_w$ | : | The cross section area |
| B | : | Maximum flux density |
| $b_w$ | : | Width of layer for a winding |
| $C_{ab}$ | : | The capacitance between parallel plates |
| $C_{ac}$ | : | AC capacitance of stored energy in the electric field for a transformer |
| $C_{dc}$ | : | DC capacitance of stored energy in the electric field for a transformer |
| $C_n$ | : | The ratio of series and parallel capacitances |
| $C_f$ | : | The output capacitance |
| $C_j$ | : | The rectifier network junction capacitance |
| $C_j'$ | : | The rectifier network junction capacitance referred to primary |
| $C_{j1}$-$C_{j4}$ | : | The junction capacitance of secondary rectifier network diodes |
| $C_P$ | : | The primary winding capacitance |
| $C_{pp}$ | : | The parallel resonant capacitance |
| $C_p'$ | : | The Equivalent primary winding capacitance referred to the primary |
| $C_{pz}'$ | : | The Equivalent primary winding capacitance referred to the primary for the multi-winding transformer |
| $C_{P-S}$ | : | The primary-secondary coupling capacitance |
| $C_{Q1}$, $C_{Q2}$ | : | The parasitic capacitance of power switches |
| $C_r$ | : | The resonant capacitance |
| $C_{stray}$ | : | The stray capacitance |
| $C_s$ | : | The secondary winding capacitance |
| $C_{ss}$ | : | The series resonant capacitance |

| | | |
|---|---|---|
| $C'_s$ | : | The equivalent secondary winding capacitance referred to the primary |
| $C'_{sz}$ | : | The equivalent secondary winding capacitance referred to the primary for the multi-winding transformer |
| $C_{s-s}$ | : | The secondary-secondary coupling capacitance |
| $C_{tr}$ | : | The equivalent transformer capacitance referred to the primary |
| D | : | The duty cycle |
| d | : | The distance of parallel conductive plates |
| $D_Q$ | : | Body diode of power switches |
| $D_1$-$D_4$ | : | The secondary rectifier network diodes |
| $\varepsilon_o$ | : | The permeability of air |
| $\varepsilon_r$ | : | The permeability of the isolation material |
| $E_{in}$ | : | The energy transferred from $V_{in}$ |
| $E_o$ | : | The energy observed by $R_o$ |
| $f_f$ | : | The fundamental frequency |
| $f_n$ | : | The normalized frequency |
| $f_P$ | : | The parallel resonant frequency of the converter |
| $f_{paralel}$ | : | The parallel resonance frequency of the transformer |
| $F_R$ | : | The ratio of $R_{ac}$ to $R_{dc}$ |
| $f_{r1}$, $f_{r2}$ | : | The no-load frequencies of the LCLC resonant converter |
| $f_{R1}$ | : | The series resonant frequencies of the LLC resonant converter |
| $f_{R2}$ | : | The parallel resonant frequencies of the LLC resonant converter |
| $f_0$ | : | The series resonant frequency of the converter |
| $f_{series}$ | : | The series resonant frequency of the transformer |
| $f_{SW}$ | : | The switching frequency of the converter |
| $f_{pp}$ | : | The frequency of parasitic resonant circuit |
| H | : | Insulator thickness between secondary windings |
| $h_n$ | : | Insulator thickness between secondary winding to airgap |
| $h_{p-s}$ | : | Insulator thickness between primary and secondary |
| $I'_s$ | : | The AC secondary current referred to the primary |
| $I_m$ | : | The magnetising current |
| $I_{off}$ | : | The main switch turn-off current |

| | | |
|---|---|---|
| $I_{pri}$ | : | The primary winding current measurement |
| $I_r$ | : | The resonant current |
| $I_R$ | : | The main resonant current measurement |
| $I_{s(RMS)}$ | : | The RMS value of AC secondary current referred to the primary |
| $I_{SW}$ | : | The main power switch current measurement |
| $I_{r(peak)}$ | : | The peak value of resonant current |
| $I_{r(RMS)}$ | : | The RMS value of resonant current |
| $I_{rms}$ | : | The rms-value of the converter current |
| $I'_{rms}$ | : | The rms-value of the first derivative of the converter current |
| $I_0$ | : | The output current of the converter |
| $I_s$ | : | The secondary current |
| $I_{seci}$ | : | The secondary i winding current measurement |
| $i_i$ | : | The output current for each secondary winding |
| $i$ | : | The current vector of multi-winding transformer |
| $J$ | : | The current density |
| $k$ | : | The coupling coefficient matrix |
| $k_{i-j}$ | : | The coupling coefficient between winding i and j |
| $k_{leak}$ | : | The coupling coefficient matrix leakage transformer |
| $k_{p-si}$ | : | The cross-coupling coefficient between they primary winding and the secondary winding $i$ |
| $k_{sj-si}$ | : | The cross-coupling coefficient between the secondary winding $j$ and the secondary winding $i$ |
| L | : | The inductance matrix for multi-winding transformer |
| $L_{C(i-j)}$ | : | The Coupled inductance between secondary winding i and j |
| $L_{ii}$ | : | The self-inductance for each winding |
| $L_{leak}$ | : | The leakage inductance matrix |
| $L_{lk}$ | : | The equivalent leakage inductance |
| $L_{lki}$ | : | The leakage inductance for the secondary winding j |
| $L_{lkp}$ | : | The primary winding leakage inductance |
| $L_{lks}$ | : | The secondary winding leakage inductance |
| $L_m$ | : | The mutual inductance |
| $L_{mcore}$ | : | The mutual inductance of core |

| | | |
|---|---|---|
| $L_{msj}$ | : | The mutual inductance for the secondary winding j |
| $L_n$ | : | The ratio of series and parallel inductances |
| $L_r$ | : | The serial resonant inductance of the LCC converter |
| $L_s$ | : | The series resonant inductance |
| $L_p$ | : | The parallel resonant inductance |
| $M_{LCC}$ | : | The voltage gain of the LCC converter |
| $M_{LCLC}$ | : | The voltage gain of the LCLC resonant converter |
| $M_{LLC}$ | : | The voltage gain of the LLC resonant converter |
| $M_{i-j}$ | : | The coupling inductances between winding i and j |
| $M_{PRC}$ | : | The voltage gain of the PRC |
| $M_{SRC}$ | : | The voltage gain of the SRC |
| N | : | The turn ratio of the transformer |
| $N_p$ | : | The number of turns for the primary winding |
| $N_s$ | : | The number of turns for thesecondary winding |
| $N_{S-Layer}$ | : | The number of turns in each layer of transformer prototype |
| $N_{si}$ | : | Number of turns for the secondary winding i |
| $p^{th}$ | : | The number of layers for foil conductors |
| $P_{loss}$ | : | The total loss |
| $P_o$ | : | The output power |
| $P_p$ | : | The sum of primary side switching and transmission losses |
| $P_s$ | : | The secondary side rectifier and transmission losses |
| $P_T$ | : | The transformer losses |
| Q | : | The quality factor |
| $Q_1$ , $Q_2$ | : | The main power switches |
| $Q_p$ | : | The parallel quality factor |
| $Q_s$ | : | The series quality factor |
| $R$ | : | The winding resistance |
| $R_{ac}$ | : | The AC resistance of a winding |
| $R_{dc}$ | : | The DC resistance of a winding |
| $R_{ds(on)}$ | : | Primary switch (MOSFETs) on resistances |
| $R_{eq}$ | : | The equiavalant load resistance |
| $R_{gap}$ | : | The resistance of close proximity air gap |

| | | |
|---|---|---|
| $R_{Lr}$ | : | Resonant inductor winding resistance |
| $R_o$ | : | The load resistance |
| $R_p$ | : | The primary winding resistance |
| $R_s$ | : | The secondary winding resistance |
| $R_{tot}$ | : | The total winding resistance |
| $t$ | : | Foil thickness |
| T | : | The converter operation period |
| TR1 | : | The multi-layer transformer prototype |
| TR2 | : | The multi-winding transformer prototype |
| $T_d$ | : | The dead time period |
| $T_{fall}$ | : | The MOSFET's current fall time |
| $t_p$ | : | The foil thickness of the primary windings |
| $t_r$ | : | The current rise time of the converter. |
| $t_s$ | : | The foil thickness of the secondary windings |
| $T_{SW}$ | : | The switching period |
| $T_{R1}$ | : | The series resonant period of the LLC resonant converter |
| $T_{pp}$ | : | The period of parasitic resonant frequency |
| $v$ | : | The voltage vector of multi-winding transformer |
| $V_a$ | : | The square wave voltage |
| $V_A$ | : | The switching network voltage measurement |
| $V_1, V_2$ | : | The voltage level of the conductive plates |
| $V_{cr}$ | : | The voltage of resonant capacitor |
| $V_{ds}$ | : | The drain-source voltage of power switches |
| $V_{DS}$ | : | The drain-sourve voltage measurement for power switches |
| $V_{in}$ | : | The input voltage |
| $V_{lr}$ | : | The voltage of resonant inductor |
| $V'_s$ | : | The AC output voltage referred to the primary side |
| $V_s$ | : | The AC output voltage |
| $V_{out}$ | : | The output voltage |
| $V_{OUT}$ | : | The output voltage measurement |
| $V_T$ | : | The core volume |
| $w$ | : | Fundemental frequency |

| | | |
|---|---|---|
| w | : | Width of the conductor |
| $W_E$ | : | The electric field energy |
| z | : | Number of winding for multi-winding transformer |
| $Z_{in}$ | : | The input impedance |
| $Z_n$ | : | The normalised input impedance |
| $Z_o$ | : | The characteristic impedance |
| $Z_{O1}$ | : | The open-circuit impedance |
| $Z_{S-Layer}$ | : | The number of turns in each layer of transformer prototype |
| Θ | : | The phase angle of $I_r$ an $V_a$ |
| α | : | The frequency loss |
| β | : | The magnetic loss of transformer core |
| η | : | The converter efficiency |
| Δ | : | The ratio of t to δ |
| $\Delta_{opt}$ | : | The optimum value of Δ |
| Δv | : | The coupled inductor in the secondary winding |
| δ | : | The skin depth |
| ρ | : | The resistivity of the conductor |
| $\varepsilon_o$ | : | The permeability of air |
| $\varepsilon_r$ | : | The permeability of the isolation material |
| AC | : | Alternative current |
| DC | : | Direct current |
| EMI | : | The electromagnetic interference |
| FEA | : | Finite Element Analysis |
| FHA | : | First Harmonic Approximation |
| LCC | : | The Inductor capacitor capacitor series parallel resonant converter |
| LCLC | : | Inductor capacitor ınductor series parallel resonant converter |
| LLC | : | Inductor ınductor capacitor series parallel resonant converter |
| MLT | : | The mean length of turns |
| MMF | : | Magneto motive force |
| OVD | : | Output voltage distribution |
| PRC | : | Parallel resonant converter |
| RMS | : | Root mean square |
| SRC | : | Series resonant converter |

| | | |
|---|---|---|
| VDE | : | Voltage distribution error |
| V | : | Volt |
| ZCS | : | Zero-current switching |
| ZVS | : | Zero-voltage switching |

# LIST of FIGURES

# LIST of TABLE

# 1. INTRODUCTION

In high-frequency power-converter applications, the weight and volume of the converter decrease by increasing operating frequency. However, increasing the frequency also increases effects of the non-ideal elements of the circuit. The non-ideal elements can increase switching losses of power switches and rectifier diodes, and decreases energy transfer efficiency of transformer. The non-ideal elements are parasitic elements such as leakage inductance and winding capacitance of the transformer, and junction capacitance of rectifier diodes. In case of hard switching, parasitic elements cause parasitic oscillations and limit the power transfer. Resonant converters can reduce switching losses significantly. A resonant converter can operate zero-voltage switching (ZVS) and zero-current switching (ZCS) [1]. The parasitic elements affect the selection of resonant topology and the operating frequency. The negative effects of parasitic elements in high-voltage applications is much more than low-voltage applications. Therefore, the effects of all parasitic elements on the converter should be analyzed. Section 1.1 provides an explanation of basic resonant converter topologies that effectively utilize parasitic elements.

## 1.1. Basic Resonant Networks

This section explains the characteristics of basic resonant networks. The resonant converters contain L-C networks. L-C networks filter the higher harmonics of square wave voltage ($V_a$) and converges the converter current to a sinusoidal waveform [2]. The five basic resonant networks are presented in Figure 1.1. Converter behaviour can be predicted by First Harmonic Approximation (FHA) according to resonant network parameters [3].

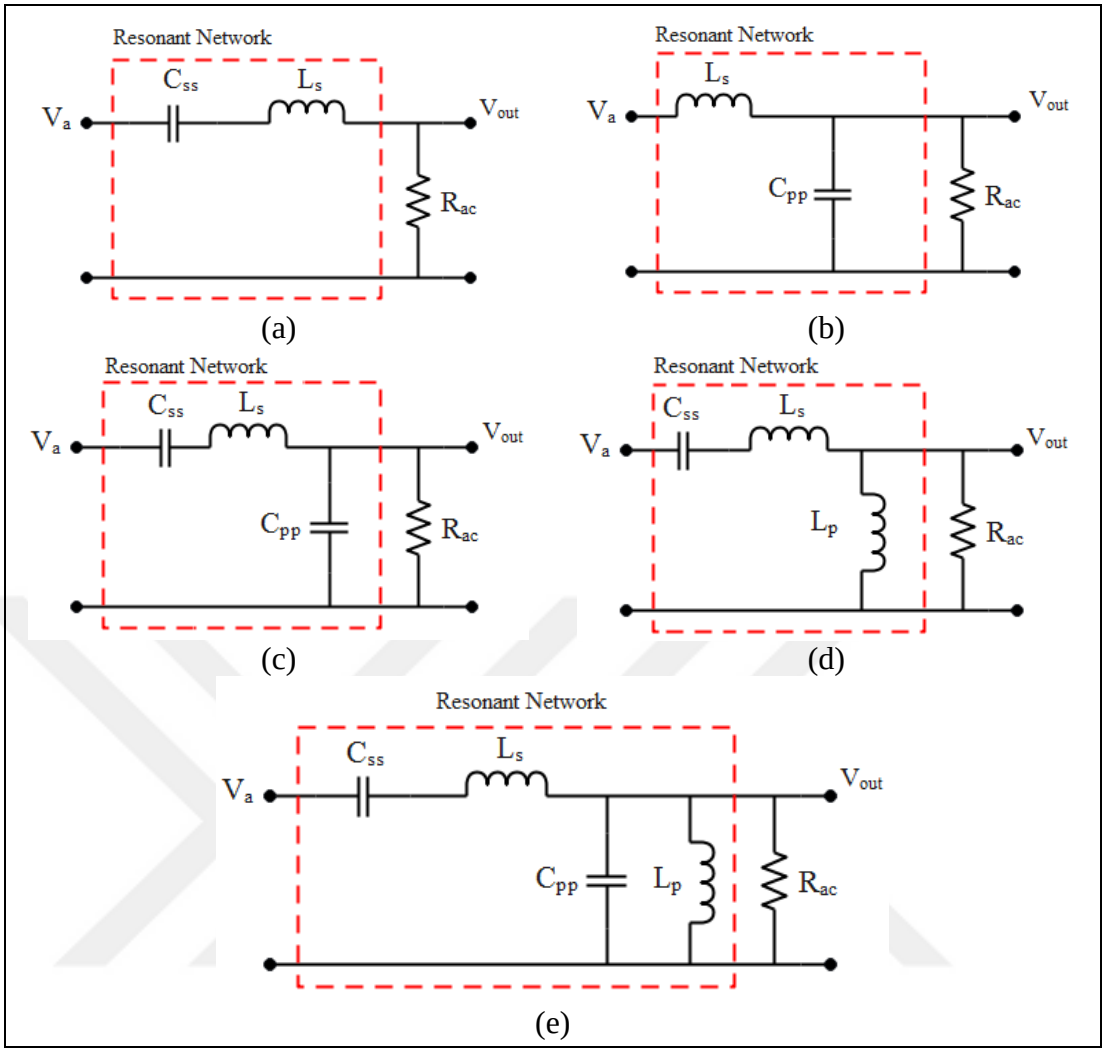


Figure 1.1: Resonant converter configurations: (a) Series resonant, (b) Parallel resonant, (c) LCC resonant, (d) LLC resonant, (e) LCLC resonant.

### 1.1.1. Series Resonant Converter

Series Resonant Converter (SRC) is presented in Figure 1.2. The SRC resonant network includes a resonant inductance ($L_s$), a resonant capacitance ($C_{ss}$). The switching network includes primary switches ($Q_1$, $Q_2$) and generate square wave voltage ($V_a$) from input voltage, $V_{in}$. The rectifier network includes rectifier diodes ($D_1$- $D_4$) and output capacitance ($C_f$).

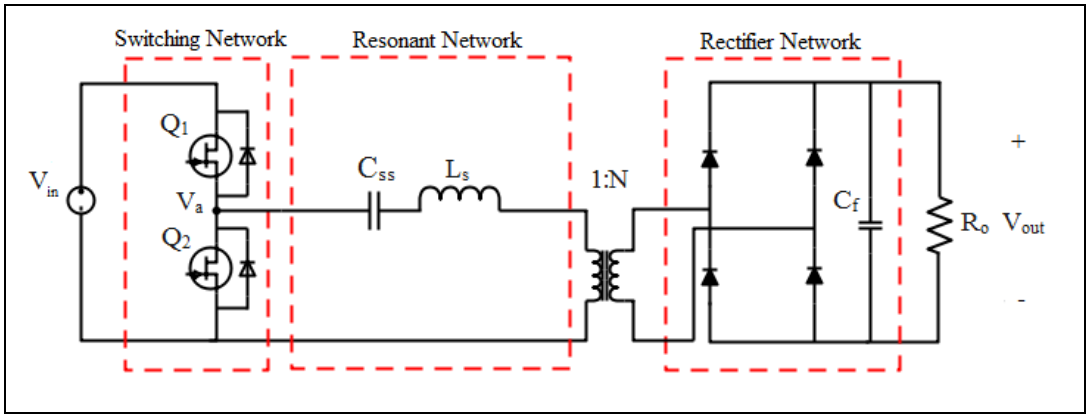


Figure 1.2: Series resonant converter.

$R_o$, $R_{eq}$, N and $Q_s$ are the load resistance, equivalent load resistance, the turn ratio of the transformer and quality factor of the converter, respectively. The normalised frequency ($f_n$) is the ratio of the converter switching frequency ($f_{sw}$) to the series resonant frequency ($f_o$). The voltage gain ($M$) is the ratio of output voltage ($V_{out}$) to $V_{in}$. The voltage gain equations of the SRC are given below [4].

$$|M_{SRC}| = \left| \frac{V_{out}}{N\left(V_{in}/2\right)} \right| = \frac{1}{\sqrt{1 + Q_S^2 \left[ f_n - \frac{1}{f_n} \right]^2}} \tag{1.1}$$

$$R_{eq} = \frac{8R_o}{N^2\pi^2} \tag{1.2}$$

$$Q_s = \sqrt{\frac{L_s}{C_{ss}}} \frac{1}{R_{eq}} \tag{1.3}$$

$$f_o = \frac{1}{2\pi\sqrt{L_s C_{ss}}} \tag{1.4}$$

$$f_n = \frac{f_{sw}}{f_o} \tag{1.5}$$

The voltage gain characteristics of the SRC are presented in Figure 1.3. SRC acts as a voltage divider by selecting transformer mutual inductance as very high. The main advantage of the SRC is short-circuit capability. At the resonant frequency, the voltage

gain is maximum and independent from the load. The main disadvantage of the SRC is the regulation problems at no load condition.

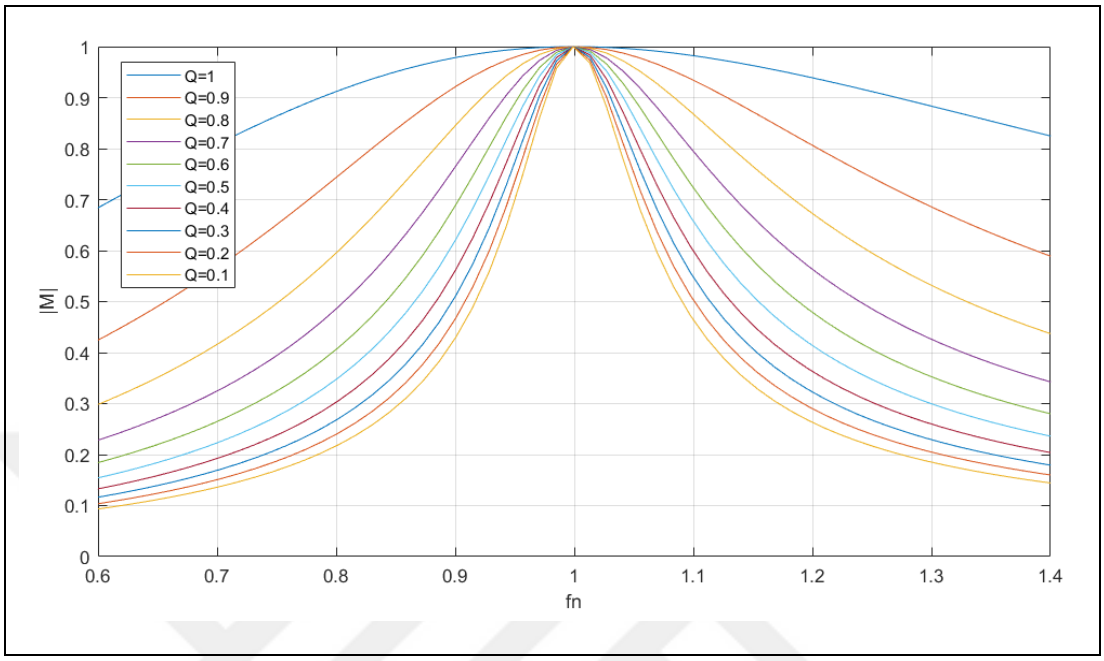


Figure 1.3: The voltage gain characteristics of SRC.

## 1.1.2. Paralel Resonant Converter

Parallel Resonant Converter (PRC) is presented in Figure 1.4. The PRC resonant network includes a resonant inductance ($L_s$), a resonant capacitance ($C_{pp}$).

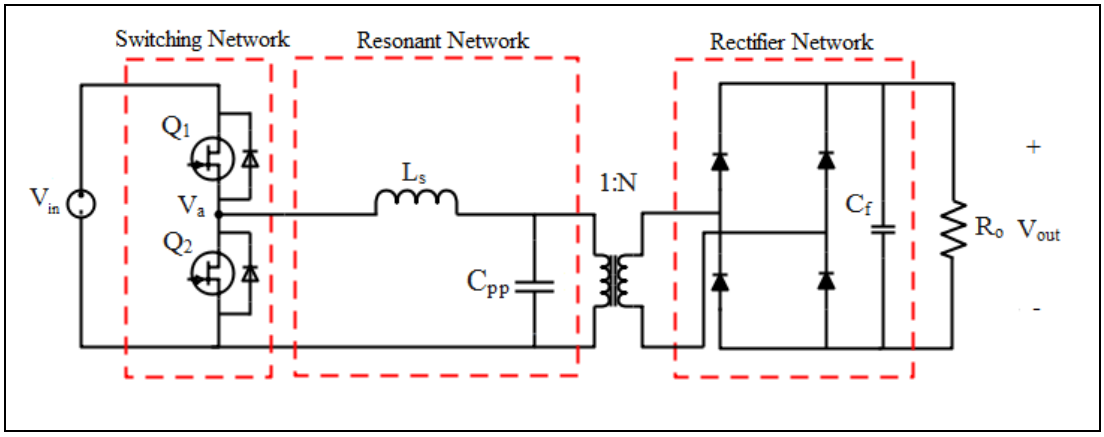


Figure 1.4: Parallel resonant converter.

$Q_p$ is the quality factor of the PRC. The voltage gain equations of the PRC are given below [4].

$$|M_{prc}| = \left| \frac{V_{out}}{N\left(V_{in}/2\right)} \right| = \frac{1}{\sqrt{[1 - f_n^2]^2 + \left[f_n Q_p\right]^2}} \tag{1.6}$$

$$f_o = \frac{1}{2\pi\sqrt{L_s C_{pp}}} \tag{1.7}$$

$$\mathrm{Q}_p = \frac{\mathrm{R}_{eq}}{\sqrt{L_s/C_{pp}}} \tag{1.8}$$

The main advantage of the PRC is the regulation capability at no load condition at the above resonant frequency. At the resonant frequency, the voltage gain is a function of the load. The PRC has a partial short-circuit capability depending on the value of $L_r$ [2]. The main disadvantage of the PRC is the circulation current in the resonant network, which is independent from the load and causes an increase of conduction losses of the switching network [2]. The circulation current can be limited by adding an inductive output filter [5]. The characteristic voltage gain variation of the PRC is presented in Figure 1.5.

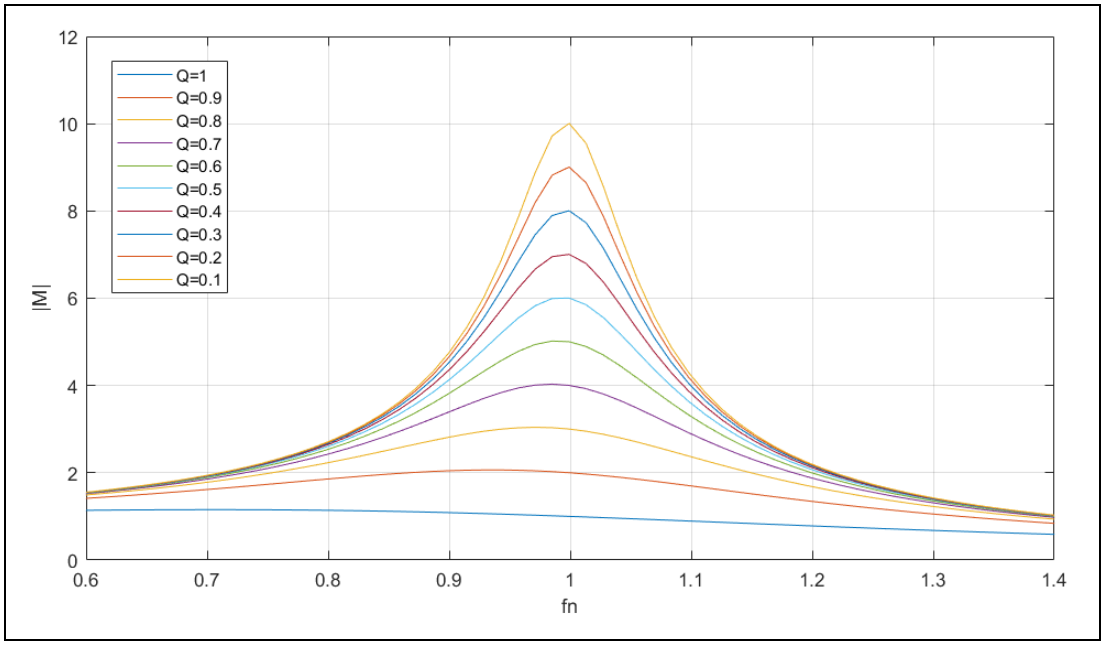


Figure 1.5: The voltage gain characteristics of the PRC.

### 1.1.3. LCC Resonant Converter

LCC resonant converter is presented in Figure 1.6. The LCC resonant network includes a resonant inductance ($L_s$), a series resonant capacitance ($C_{ss}$) and a parallel resonant capacitance ($C_{pp}$).

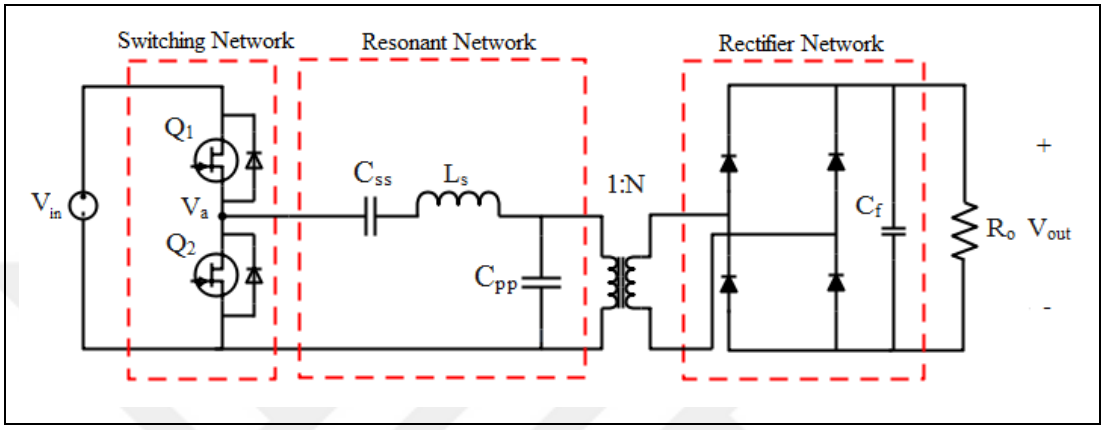


Figure 1.6: LCC resonant converter.

LCC resonant converter has a serial resonant frequency $f_o$ and a parallel resonant frequency $f_p$. $C_n$ is defined as the ratio of $C_{pp}$ to $C_{ss}$. The voltage gain equations of LCC resonant converter are given below [6].

$$|M_{LCC}| = \left| \frac{V_{out}}{N\left(V_{in}/2\right)} \right| = \frac{1}{\sqrt{\left[C_n\left(1-{f_n}^2\right)+1\right]^2 + {Q_p}^2\left(f_n - \frac{1}{f_n}\right)^2}} \tag{1.9}$$

$$f_o = \frac{1}{2\pi\sqrt{L_s C_{ss}}} \tag{1.10}$$

$$f_p = \frac{1}{2\pi\sqrt{L_s \frac{C_{ss}C_{pp}}{C_{ss}+C_{pp}}}} \tag{1.11}$$

$$C_n = \frac{C_{pp}}{C_{ss}} \tag{1.12}$$

In heavy load conditions, the LCC resonant converter behaves like the SRC close to $f_o$. In the light load conditions, the effect of $C_p$ increases, and the LCC resonant converter acts like the PRC close to $f_p$. Thus, the LCC converter reduces the drawbacks of the SRC and PRC [2]. The voltage gain characteristics of the LCC resonant converter are presented in Figure 1.7.

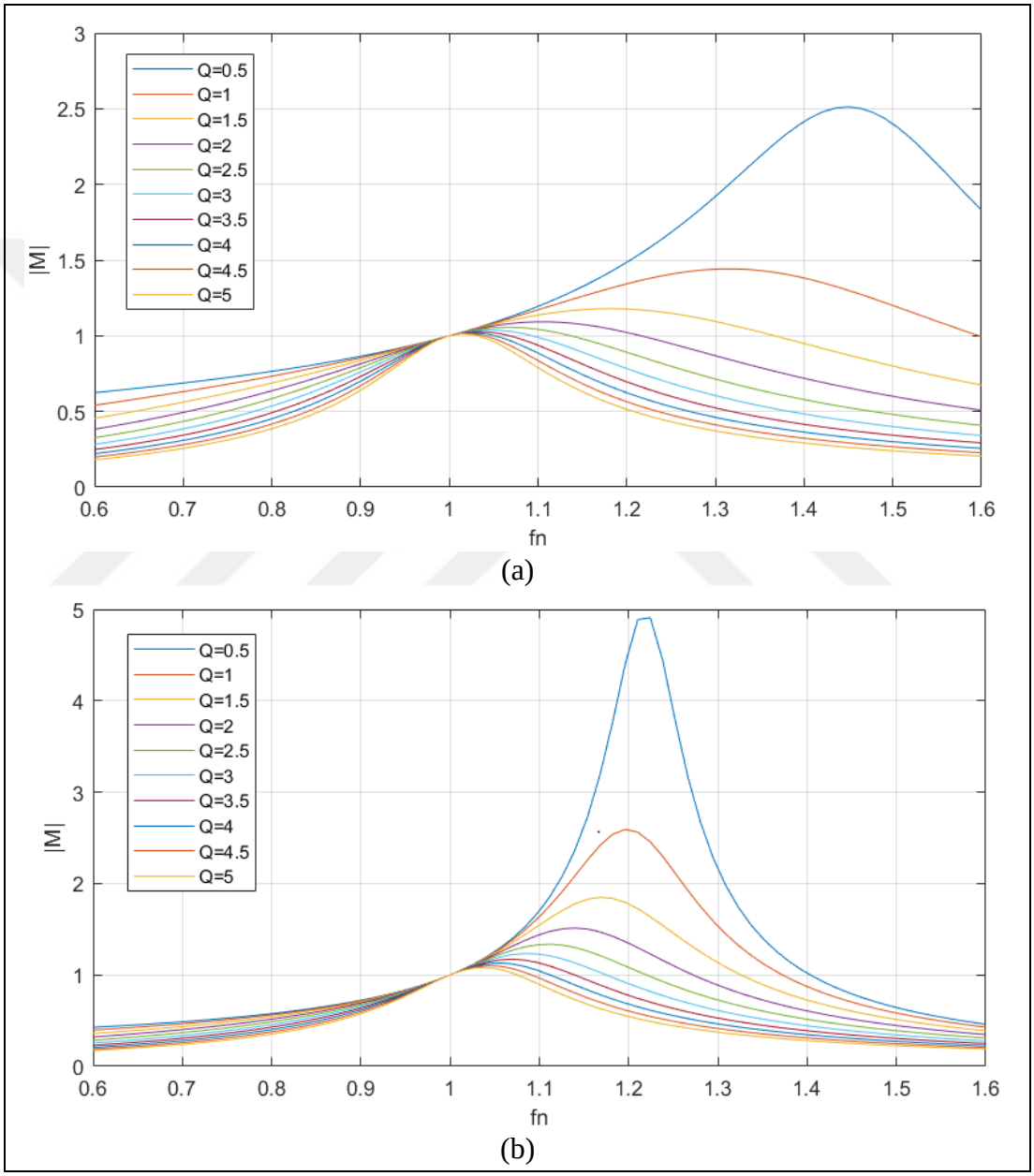


Figure 1.7: The voltage gain characteristics of LCC resonant converter: (a) $C_n = 0.8$ , (b) $C_n = 2$.

LCC resonant converter characteristic highly depends on $C_n$. Increasing $C_n$ also increases the voltage gain and circulation current at light load conditions, and reduces

converter efficiency. The LCC resonant converter needs to operate at very high frequencies, which causes larger EMI filter requirements [4]. The LCC resonant converter neglects the effects of transformer mutual inductance. Since primary turns are limited in high-frequency applications, the impedance of mutual inductance can not be ignored [7].

### 1.1.4. LLC Resonant Converter

LLC (Series-Parallel) resonant converter is presented in Figure 1.8. The LLC resonant network includes a series resonant inductance ( $L_s$ ), parallel resonant inductance ($L_p$) and series resonant capacitance ($C_{ss}$).

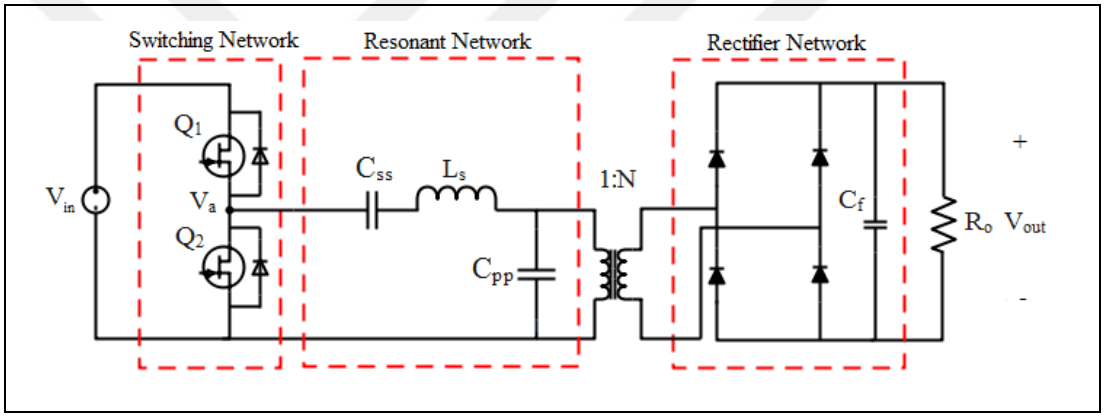


Figure 1.8: LLC resonant converter.

The LLC resonant converter has a serial resonant frequency $f_o$ and a parallel resonant frequency $f_p$. $L_n$ is defined as the ratio of $L_s$ to $L_p$. The voltage gain equations of the LLC resonant converter are given below [6]. The voltage gain characteristics of the LLC resonant converter are presented in Figure 1.9.

$$|M_{LLC}| = \left| \frac{V_{out}}{N\left({}^{V_{in}}/_{2}\right)} \right| = \frac{1}{\sqrt{\left(L_n + 1 - \frac{L_n}{f_n^2}\right)^2 + {Q_s}^2 (f_n - \frac{1}{f_n})^2}} \tag{1.13}$$

$$f_o = \frac{1}{2\pi\sqrt{L_s C_{ss}}} \tag{1.14}$$

$$f_p = \frac{1}{2\pi\sqrt{(L_s + L_p)C_{ss}}} \tag{1.15}$$

$$L_n = \frac{L_p + L_s}{L_s} \tag{1.16}$$

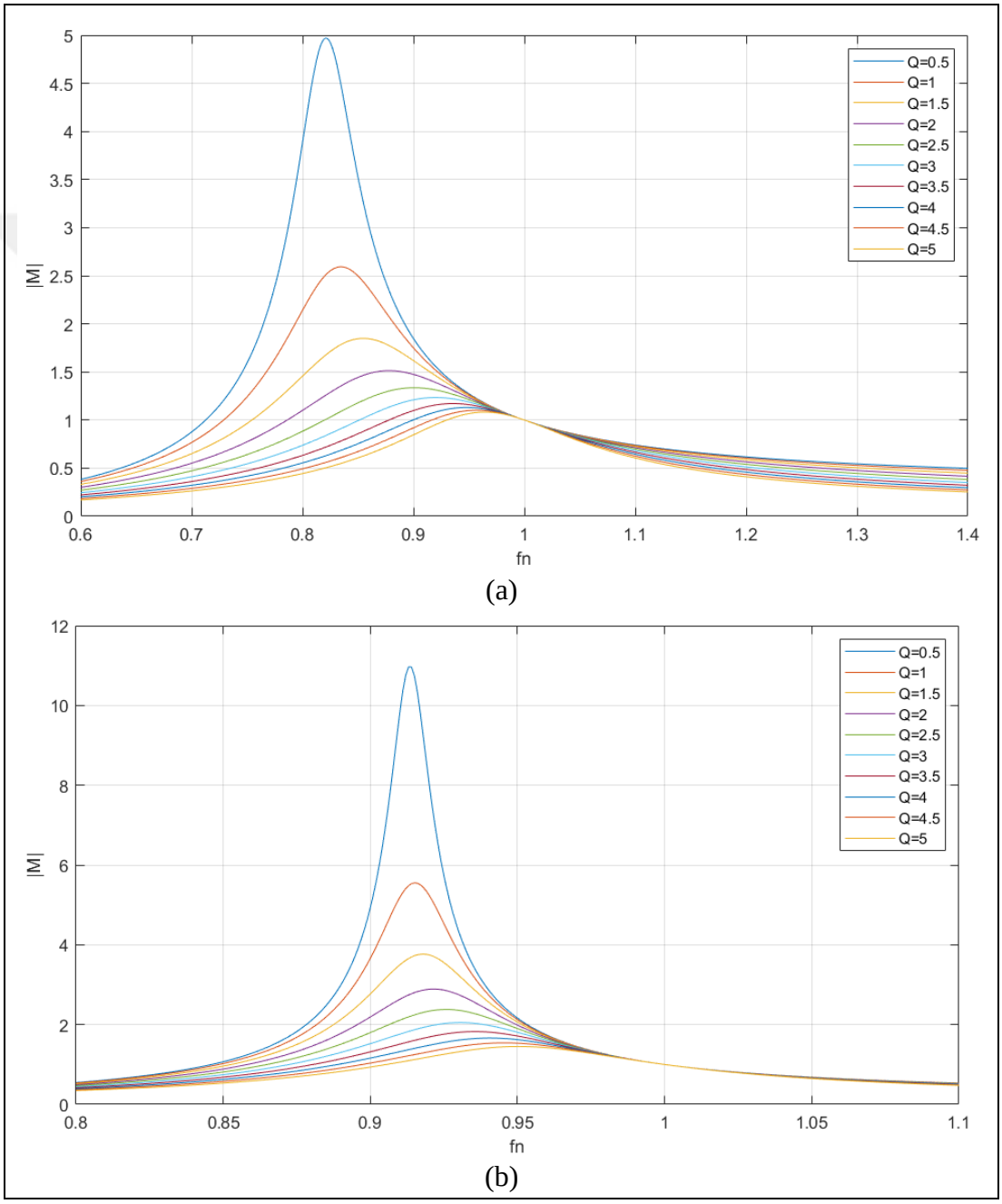


Figure 1.9: The voltage gain characteristics of the LLC resonant converter: (a) $L_n = 2$ , (b) $L_n = 5$.

The LLC resonant converter offers load and line regulation for wide load and voltage ranges [4]-[6], short-circuit capability and high efficiency. The LLC resonant converter has a very high sensitivity to transformer parasitic capacitive effects [7].

### 1.1.5. LCLC Resonant Converter

The LCLC resonant converter is presented in Figure 1.10. The LCLC resonant network includes a series resonant inductance ($L_s$), a series resonant capacitance ($C_{ss}$), parallel resonant inductance ($L_p$) and series resonant capacitance ($C_{ss}$).

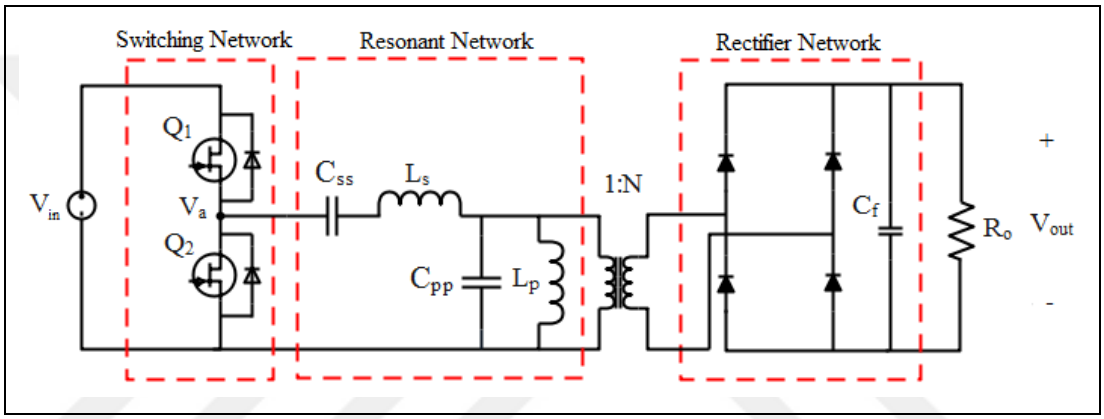


Figure 1.10: LCLC resonant converter.

The LCLC resonant converter has four resonant frequencies. $f_o$ and $f_p$ are serial resonant frequency and parallel resonant frequency, respectively. $f_{r1}$ and $f_{r2}$ are the no-load frequencies [8]. The voltage gain of the LCLC is expressed as [4]:

$$|M_{LCLC}| = \frac{1}{\sqrt{\left(1 + L_n + C_n - C_n f_n^2 - \frac{L_n}{f_n^2}\right)^2 + Q_p^2 (f_n - \frac{1}{f_n})^2}} \tag{1.17}$$

$$f_o = \frac{1}{2\pi\sqrt{L_s C_{ss}}} \tag{1.18}$$

$$f_p = \frac{1}{2\pi\sqrt{L_p C_{pp}}} \tag{1.19}$$

$$f_{r1} = \frac{1}{2\pi\sqrt{(L_s + L_p)C_{ss} + L_p C_{pp}}} \tag{1.20}$$

$$f_{r2} = \frac{f_o\, f_p}{f_{r1}} \tag{1.21}$$

The gain characteristics of the LCLC resonant converter are presented in Figure 1.11 when $L_n$ is equal to $C_n$, and in Figure 1.12 when $L_n$ is not equal to $C_n$.

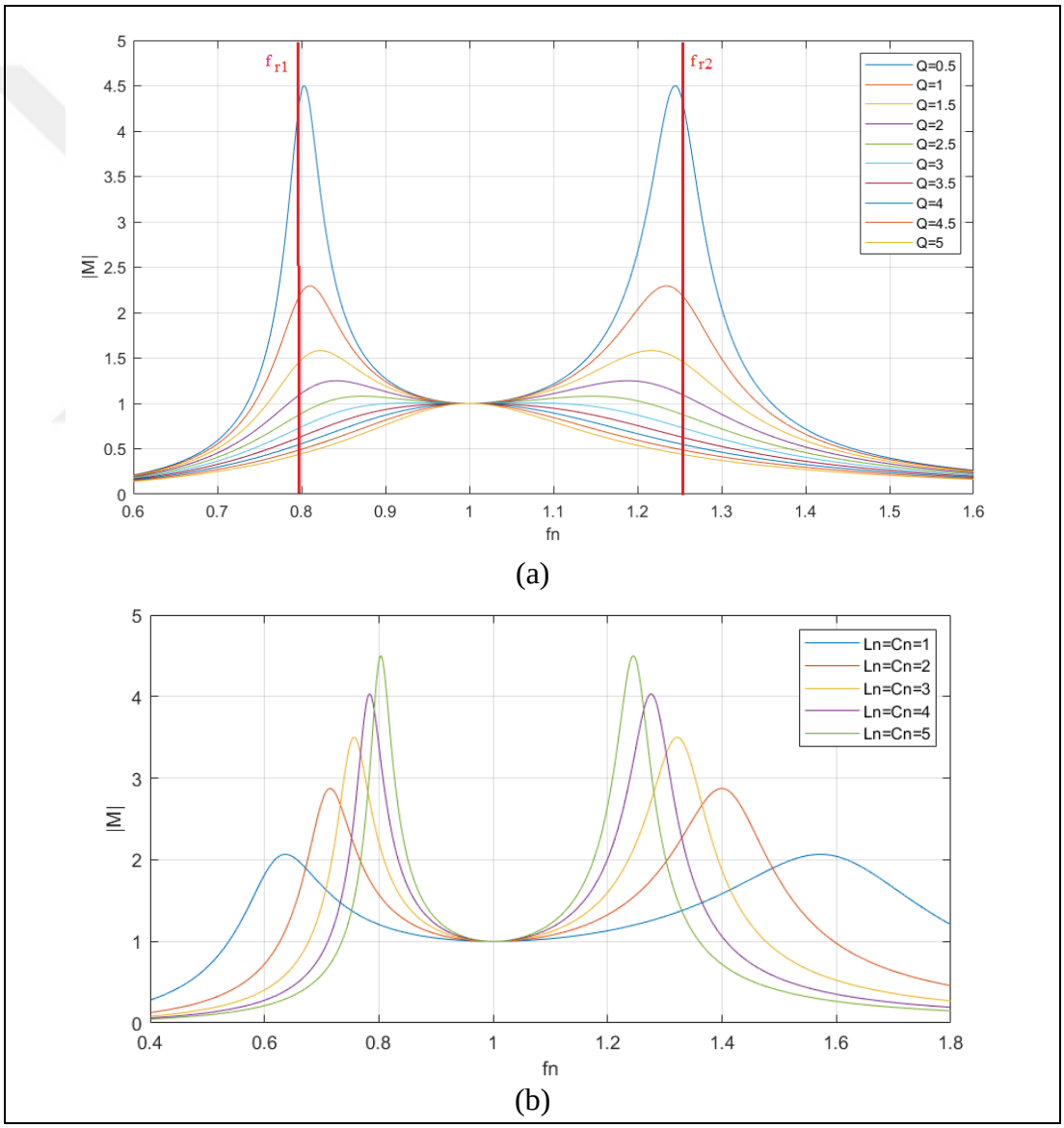


Figure 1.11: The voltage gain characteristic of the LCLC resonant converter: (a) when $L_n = C_n = 5$ and $Q$ is varied , (b) when $Q = 0.5$ and $L_n = C_n$ are varied.

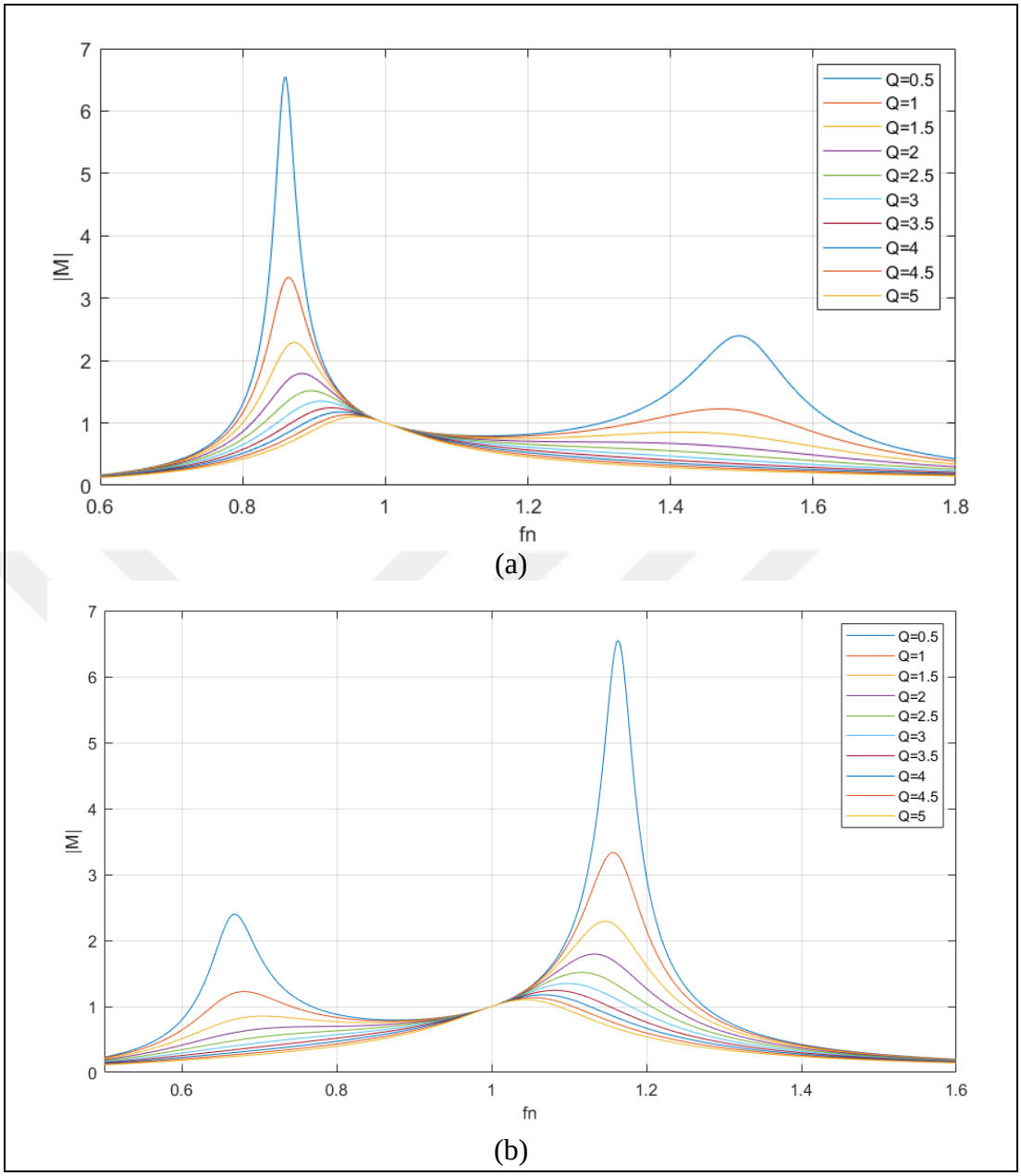


Figure 1.12: The voltage gain characteristic of the LCLC resonant converter: (a) when $L_n = 5,\ C_n = 2$ and $Q$ is varied, (b) when $L_n = 2,\ C_n = 5$ and $Q$ is varied.

The LCLC resonant converter operates like an LLC resonant converter where $L_n > C_n$ and $f_n \approx 1$. The LCLC resonant converter operates like an LCC resonant converter where $L_n > C_n$ and $f_{sw} \approx f_p$.

### 1.1.6. Selection of Resonant Network

In the previous section resonant network elements are assumed ideal and parasitic elements are not considered. However, in practice parasitic componets affects the operation of the converter. The choice of resonant network depends on which circuit element values force the current waveform into sinewave at the operating frequency, and determined by the interaction of the resonant network components and the parasitic components. The increasing number of main resonant components causes difficulty in designing and analyzing the converter [9]. The selection criteria of the resonant network depending on the main resonant components is presented in Figure 1.13.

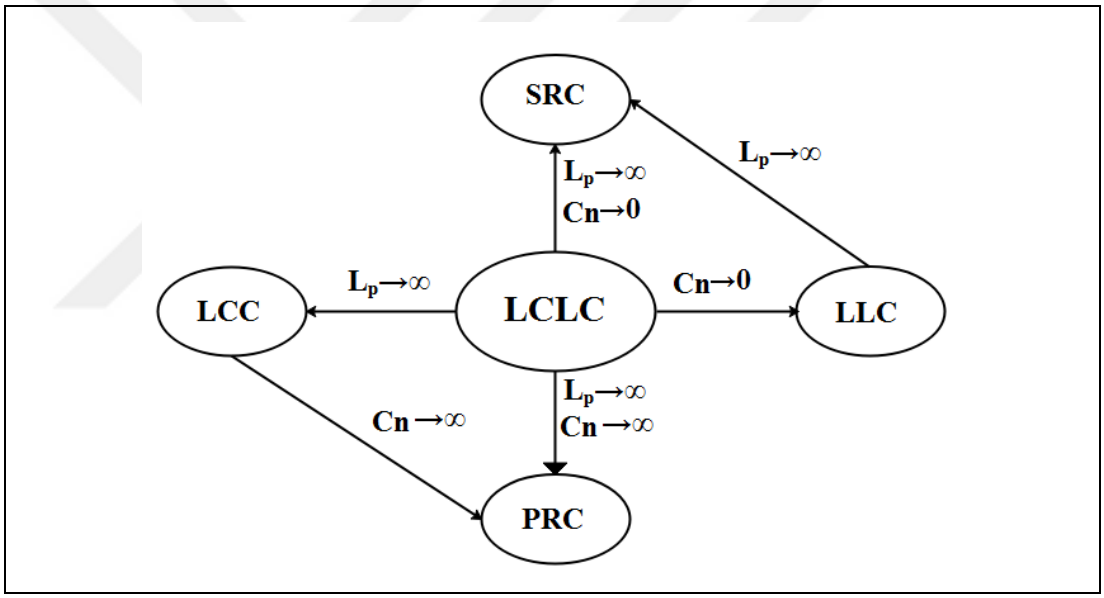


Figure 1.13: The selection criteria of the resonant network depending on the main resonant components.

### 1.1.7. Background

In high-frequency DC-DC power converter applications, the weight and volume of the converter decrease if operating frequency is increased. However, increasing the frequency also increases the deterioration effects of parasitic elements. The parasitic elements must be considered or adopted as the main elements of the resonant circuit [10].

The parasitic capacitances of the transformer are caused by stored energy in the electric field in a transformer. The parasitic capacitance of a two-port transformer was modeled experimentally, measured by frequency response in [11] and by step response in [12], [13]. The energy-based model was evaluated and validated by PSPICE simulation in [14]. The parasitic capacitance of a two-port sectional transformer was analytically modeled and experimentally measured in [15]. The influence of the electrostatic shielding on the capacitance of the transformer was evaluated and simulated in [16]. The numerical model of the parasitic capacitance of a high-frequency multi-winding transformer was assessed with electrostatic equations in [17] and validated by Finite Element Analysis (FEA) in [18]. The electric field characteristics of multi-winding transformers were simulated in [19]. The parasitic capacitance model for multi-winding transformer was simplified in [20] and analyzed in [21].

The two-port transformer parasitic capacitance was evaluated and reduced by the winding arrangement using the parallel plate method in [22], [23], which is difficult to use in high-voltage applications. The stored energy in the electric field in a transformer includes two components; one changes during the switching period while the other does not change. The parasitic capacitance of a multi-winding transformer was experimentally reduced using rectifier integration by separating stored energy in the electric field to AC and DC components in [24]. The effects of the rectification network selection, the number of layers, the magnetic field, and the leakage transformer were not discussed.

The AC winding losses are described for the sinusoidal current in the high-frequency transformers by Dowell and Ferreira, and the variation of winding losses was modeled in [25], [26]. The effects of winding configuration and layer porosity on AC winding losses were modeled in [27]. Analytical optimisation for winding losses was examined in [28]. A comparison of foil and round conductors for AC winding losses was performed in [29], and optimization for foil conductors is simulated in [30]. The effects of airgap and notch area on winding losses were analytically modeled in [31]. Effects of foil conductor thickness on winding losses for a gapped inductor were examined in [32]. The impacts of foil conductor width and winding arrangement on losses for a gapped inductor were evaluated in [33]. Analytical optimization of winding losses was modeled for non-sinusoidal current in the high-frequency transformers [34]. Reducing winding losses using interleaving winding arrangement

was provided in [22], [35], [36]. In high-voltage transformers, the interleaving winding arrangement is not possible because of the isolation requirements. In all studies, the winding loss is a function of thickness for foil conductors or diameter for round conductors. Thus, the winding losses can be optimized.

The multi-winding transformer includes a leakage transformer that acts like a coupled inductor and causes different couplings in the windings. Thus, the coupled inductor causes unbalanced power transfer between windings. The equivalent circuit for a multi-winding transformer was defined and modeled in [37]. The magnetic part of the equivalent circuit for a multi-winding transformer was presented in [38]. The leakage flux of a multi-winding transformer was experimentally modeled, and the relationship between leakage inductances and magnetising inductances was defined in [39]. A leakage measurement of the multi-winding transformer was performed, and a useful simulation model was provided in [40]. The characterization of the leakage transformer was modeled in [41]. The eddy current effect in a multi-winding transformer was modeled by using R matrix in [42]. A generalized circuit model for the eddy current effect on the multi-winding transformer was presented [43]. Configuration optimization of the multi-winding transformer was modeled using FEA in [44]. The winding arrangement effect on the multi-winding transformer model was given in [40], [45], [46]. The high coupled inductor was analyzed in [47], and the model of the multi-winding transformer by separating mutual and leakage inductances was presented and analyzed in [48]. The equivalent circuit of the leakage flux was given with the principle of duality between the electric and the magnetic circuits in [45]. A comprehensive assessment of the multi-winding transformer was given in [49]. The rectifier network diodes junction capacitance impact of the transformer capacitance was provided in [50], [51].

The resonant converters were modeled using the FHA [3]. A comparison of resonant topologies was given in [2], [4], [5]. The PRC resonant converter is suitable for high-voltage applications and used experimentally by considering the transformer parasitic capacitive effects [2]. The SRC resonant converter is suitable for high-voltage applications and used experimentally in many applications [52], [53]. The LCC resonant converter is suitable for high-voltage applications and experimentally investigated by considering the transformer parasitic capacitive effects [54], [55]. The LCC resonant converter is used in high-voltage applications with a multi-winding transformer [56] and a multi-transformer [57]. The LCLC resonant converter is

suitable for high-voltage applications and experimentally investigated by considering the transformer parasitic capacitive effects and magnetising inductance [7].

The steady-state analysis of the LLC resonant converter was presented in [9], [58]. The LLC resonant converter can operate in a wide output voltage range by optimization of the $L_n$ and $C_{ss}$ values [12], [59]. The impact of selecting the resonant capacitor ($C_{ss}$) value was examined and compared in [60]; as a result, a lower value of $C_s$ decreases turn-off losses of main power switches. The impact of selecting $L_n$ and quality factor values for the LLC resonant converter was analyzed using impedance characterization of the converter in [61]. The steady-state analysis of the LLC resonant converter considering internal resistances was presented in [62]. The influence of the parasitic components on the LLC resonant converter, which causes oscillations and voltage spikes, was examined in [63]. An accurate design algorithm considering the parasitic elements of power switches is proposed in [64], [65]. Adding an auxiliary resonant circuit as a variable inductor decreases the impact of the parasitic elements [66]. An accurate design and detailed time domain analysis considering the impact of the parasitic components are performed by limiting the maximum value of $L_p$ in [67], [68].

LLC resonant converter has a very high sensitivity to parasitic capacitances [7]. The parasitic capacitances include junction capacitances of power switches, transformer parasitic capacitances, and secondary side rectifier junction capacitances. The soft switching condition of the LLC resonant converter depends on the stored energy in the parasitic capacitances must be absorbed during the dead time period by $L_p$. The value of $L_p$ is generally adjusted with air gap. The transformer efficiency decreases by adding more air gap.

The impact of parasitic capacitances of the transformer for high-voltage applications is higher than for low-voltage applications. Thus, the LLC resonant converter has serious limitations for high-voltage applications because of the higher parasitic capacitance of the high-voltage transformer. LLC resonant converter is preferred in low-voltage applications [6]. There are simulation-based studies about LLC resonant converters for high-voltage applications [69], [70].

## 1.2. Thesis Motivation and Objectives

In high-voltage applications, the LCC converter is widely used due to inherit structure of the transformer parasitic capacitance. The motivation of this thesis is to use the LLC resonant converter in high-voltage applications because of higher efficiency and better voltage regulation than the LCC converter.

In order to use the LLC resonant converter in high-voltage applications, it is necessary to decrease the parasitic capacitance of the high-voltage transformer to negligible values with the winding arrangement. The objective of this thesis is decreasing the value of capacitive elements on high voltage transformer with the winding arrangement, minimize that arrangement influence to winding losses and experiment proposed winding arrangement with LLC resonant converter which is sensitive to capacitive elements.

## 1.3. Thesis Structure and Content

The thesis study is divided into 5 sections. Section 2 explains a detailed analysis of the LLC resonant converter. The circuit description, impedance characterization, analysis of operation regions and converter conduction states are given. The effect of the parasitic capacitances and soft switching conditions are also described. The time domain and frequency domain simulations are performed. The impact of the transformer and the rectifier network capacitances on the LLC resonant converter and circuit limitations are discussed.

Section 3 is about the parasitic element of the transformer model. The model of high-frequency transformer and integration of the rectifier network to transformer are analyzed. Moreover, the analysis of the multi-winding transformer model is performed.

In Section 4, the proposed winding arrangement of the multi-winding transformer is described, and FEA simulation is performed to quantify the performance.

The experimental verification of the established model, comparative measurements, and application of the LLC resonant converter for high-voltage applications are presented in Section 5. The results of the study were published in [71].

Finally, the last section of the thesis provides conclusions and suggestions for future work.

# 2. ANALYSIS OF THE LLC RESONANT CONVERTER

This section presents a design procedure and analysis for the LLC converter. The converter circuit is described, and then the analytical description and operation behaviour is discussed based on the FHA. Furthermore, the effects of the capacitive parasitic elements of the transformer on the LLC resonant converter are shown. Moreover, the stress of the main switching components and their analytical description are presented. Numerical simulation results are also provided for the operation modes.

## 2.1. Circuit Description

This section presents the description of the elements of the half-bridge LLC converter. The half-bridge LLC resonant converter is shown in Figure 2.1. There are differences compared to the LLC resonant converter basic structure presented in Figure 1.7. because the parasitic elements of the transformer, switching MOSFETs and rectifier network are considered.

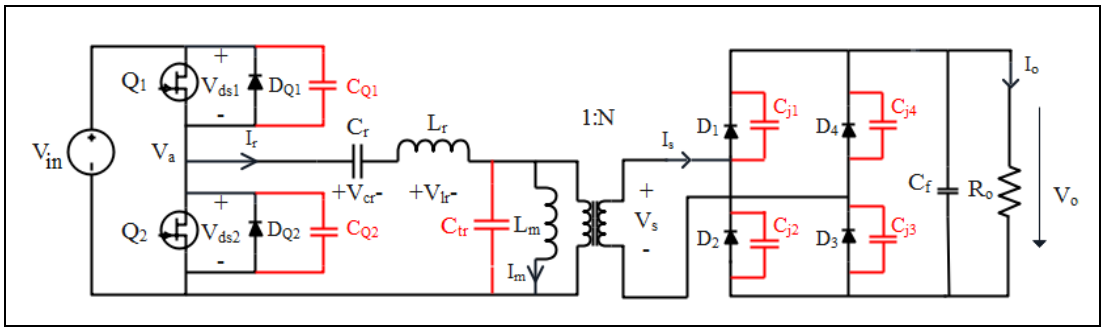


Figure 2.1: The LLC resonant converter including the transformer parasitic components.

Besides the resonant elements conventionally used in the LLC topology, $L_m$ is the mutual inductance, $L_r$ is the leakage inductance and $C_r$ is the resonant capacitance. $Q_1$ and $Q_2$ are the power switches. $C_Q$, $D_Q$ and $V_{\mathrm{ds}}$ are the parasitic capacitance, body diode and the drain-source voltage of power switches, respectively. $D_1$-$D_4$ and $C_{j1}$-$C_{j4}$ are the secondary rectifier network diodes and junction capacitances of diodes, respectively. $I_r$, $I_m$ and $I_s$ are the resonant current, magnetising current and secondary current, respectively. $V_{cr}$, $V_{lr}$ and $V_s$ are the voltage of $C_r$, the voltage of $L_r$ and the

AC output voltage, respectively. $V_o$, $C_f$ and $R_o$ are the output voltage, output capacitance and load resistance.

## 2.2. Theoretical Analysis

### 2.2.1. Impedance Characteristics

The LLC resonant circuit can be modelled using a characteristic impedance model to simplify the analysis. The simplest model is the AC resistance model [3]. A simplified LLC resonant converter is presented in Figure 2.2. The parasitic components are neglected. The effects of the parasitic components will be discussed in Section 2.2.4.

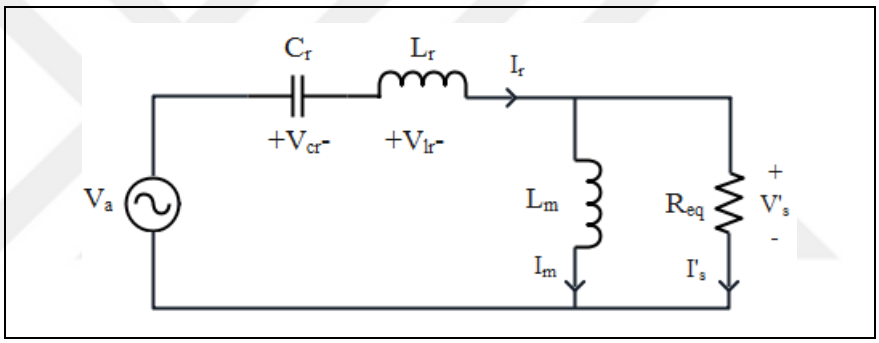


Figure 2.2: The simplified circuit of the LLC resonant converter.

The LLC resonant converter circuit expressions are given below. $R_{eq}$, $Z_O$ and Q are the equivalent load resistance, characteristic impedance and quality factor of the circuit. The normalised frequency ($f_n$) is the ratio of the resonant converter switching frequency ($f_{SW}$) and the series resonant frequency ($f_{R1}$). The parallel resonant frequency ($f_{R2}$) is the resonant frequency of $L_p = L_r + L_m$ and $C_r$.

$$R_{eq} = \frac{8\,R_o}{N^2\pi^2} \tag{2.1}$$

$$Z_O = \sqrt{\frac{L_r}{C_r}} \tag{2.2}$$

$$\mathrm{Z}_{O1} = \sqrt{\frac{L_p}{C_r}} \tag{2.3}$$

$$\mathrm{Q} = \mathrm{Z}_O \frac{1}{\mathrm{R}_{eq}} \tag{2.4}$$

$$f_{R1} = \frac{1}{2\pi\sqrt{L_r C_r}} \tag{2.5}$$

$$f_{R2} = \frac{1}{2\pi\sqrt{L_p C_r}} \tag{2.6}$$

$$f_n = \frac{f_{SW}}{f_{R1}} \tag{2.7}$$

$$L_n = \frac{L_p}{L_s} \tag{2.8}$$

The normalised input impedance $(\mathrm{Z}_n)$ is the ratio of input impedance $(\mathrm{Z}_{in})$ and the characteristic impedance $(\mathrm{Z}_o)$. $\mathrm{Z}_{O1}$ is the open-circuit impedance. Figure 2.3 shows the frequency characteristic of $\mathrm{Z}_n$. The equations for $\mathrm{Z}_n$ and $\mathrm{Z}_{in}$ are given below.

$$Z_{in} = sL_r + \frac{1}{sC_r} + sL_m // \mathrm{R}_{eq} \tag{2.9}$$

$$\mathrm{Z}_n = \frac{Z_{in}}{Z_0} = \left(\frac{{f_n}^2 {L_n}^2 \mathrm{Q}}{1 + {f_n}^2 {L_n}^2 \mathrm{Q}^2}\right) + j\left(f_n - \frac{1}{f_n} + \frac{f_n L_n}{1 + {f_n}^2 {L_n}^2 \mathrm{Q}^2}\right) \tag{2.10}$$

When $f_n$ converges to 0 or ∞, $\mathrm{Z}_n$ reaches very high values in any load condition. If Q gets closer to 0, $\mathrm{Z}_n$ converges to $\mathrm{Z}_{o1}$, and $f_{SW}$ converges to $f_{R2}$. When Q gets closer ∞, $\mathrm{Z}_n$ converges to $\mathrm{Z}_o$, and $f_{SW}$ converges to $f_{R1}$. The critical value of $\mathrm{R}_{eq}$ must be greater than $\mathrm{Z}_{O1}$, and in the operating region, $L_n$ and Q values must be selected as below [61].

$$\sqrt{L_n}\mathrm{Q} \leq 1 \tag{2.11}$$

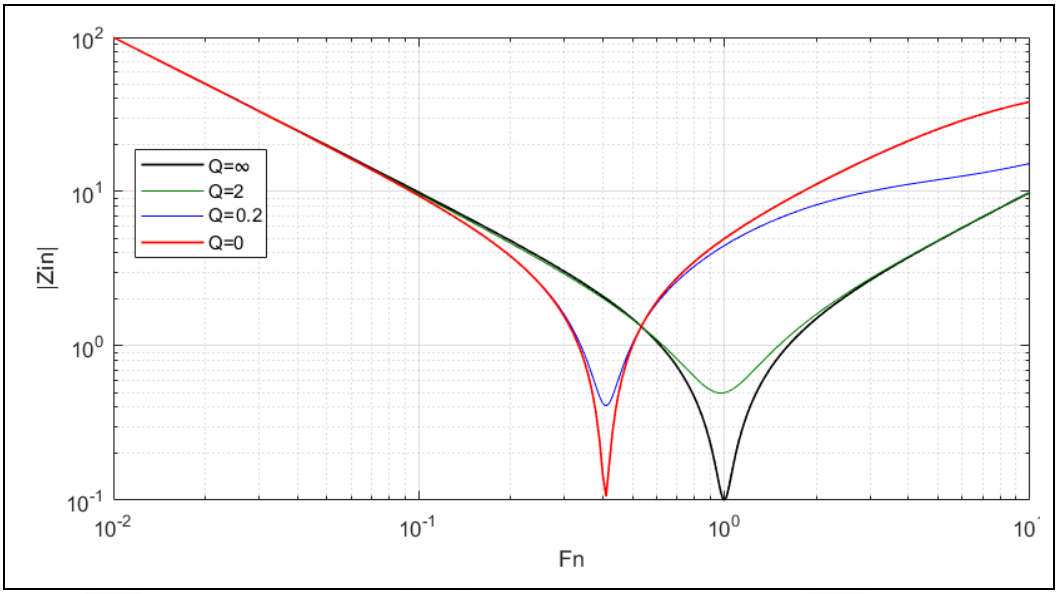


Figure 2.3: The frequency characteristic of normalised input impedance for the LLC resonant converter.

### 2.2.2. Operation Regions

The most common control strategy for LLC resonant converters is frequency control [63]. The frequency characteristic of voltage gain for the resonant converter is obtained by using equation (2.12) and presented in Figure 2.4. The converter has three operating regions. The converter operates in the inductive region when $I_r$ is lagging $V_a$ ($V_{lr} > V_{cr}$). The converter operates in the capacitive region when $V_a$ is lagging $I_r$ ($V_{cr} > V_{lr}$). The converter operates in the resistive region when $I_r$ and $V_a$ are in the same phase ($V_{lr} = V_{cr}$). Regions 1 and 2 are the inductive regions, and Region 3 is the capacitive region, as described below. The boundary of Regions 2 and 3 is the resistive region.

$$M_{LLC} = \frac{1}{\sqrt{\left(L_n + 1 - \frac{L_n}{f_n^2}\right)^2 + Q^2\left(f_n - \frac{1}{f_n}\right)^2}} \tag{2.12}$$

The LLC resonant converter should operate in the inductive region, which means $I_r$ is lagging $V_a$ to achieve ZVS in primary switches. When the converter operates the capacitive region or the boundary of Regions 2 and 3, primary power switches operate

in hard-switching conditions. In this situation, the switching losses will increase and must be considered.

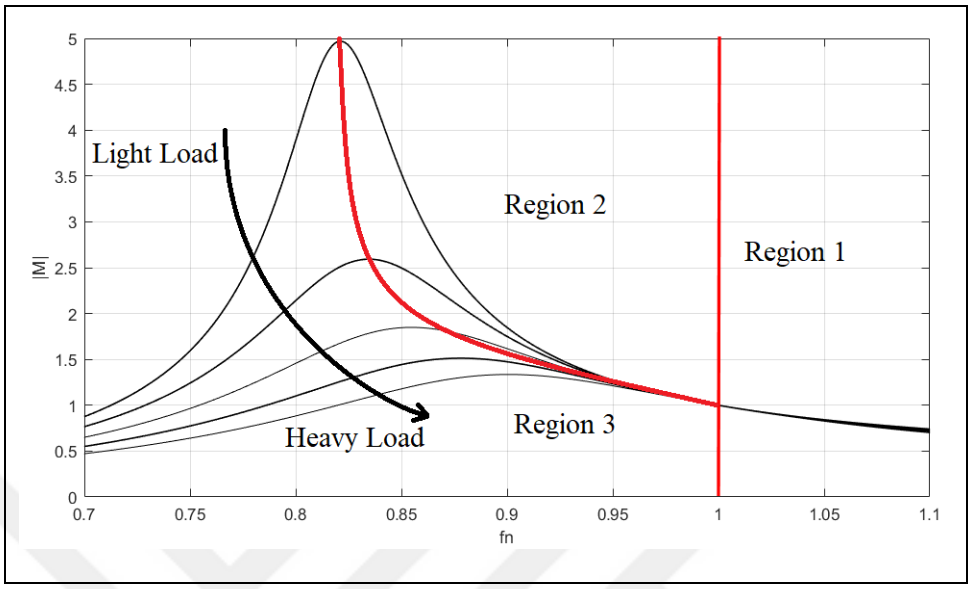


Figure 2.4: Operation regions of the LLC resonant converter.

The phasor diagram of main voltages and currents is presented in Figure 2.5. The phase angle of $I_r$ lagging $V_a$ is Θ. The voltage of the resonant tank is $V_r$. $V_s'$ and $I_s'$ are AC output voltage and current referred to the primary side, respectively. The equations for $V_r$, $V_s'$ and $I_s'$ are given below.

$$V_s' = \frac{V_s}{N} = \frac{1}{N}\frac{2\sqrt{2}}{\pi} V_o \tag{2.13}$$

$$I_s' = NI_s = N\frac{\pi}{2\sqrt{2}} I_o \tag{2.14}$$

$$V_r = V_{cr} - V_{lr} \tag{2.15}$$

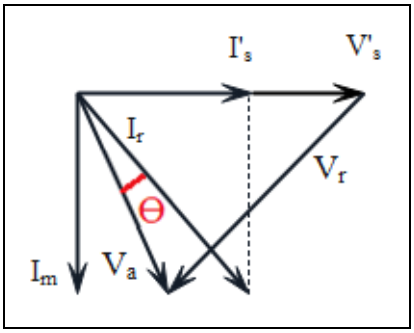


Figure 2.5: Current and voltage phasor diagram for the LLC resonant converter.

LLC resonant converter has three operation stages in the inductive region. In stage P, the main part of the energy is transferred to $R_o$, and a part of the energy is stored in the resonant tank. In stage N, $D_{Q1}$, $D_{Q2}$ and rectifier network diodes are conducting by using stored energy in the resonant tank. Thus, a part of the energy is transferred to $R_o$, and the main part of the energy is stored in the resonant tank. In stage O, secondary rectifier network diodes are turned off, and one of the main switches in the switching network is on state. Thus, energy is not transferred to $R_o$ and stored in the resonant network [68].

When $f_n \approx 1$, the converter operates in P mode, and basic current and voltage waveforms are presented in Figure 2.6.

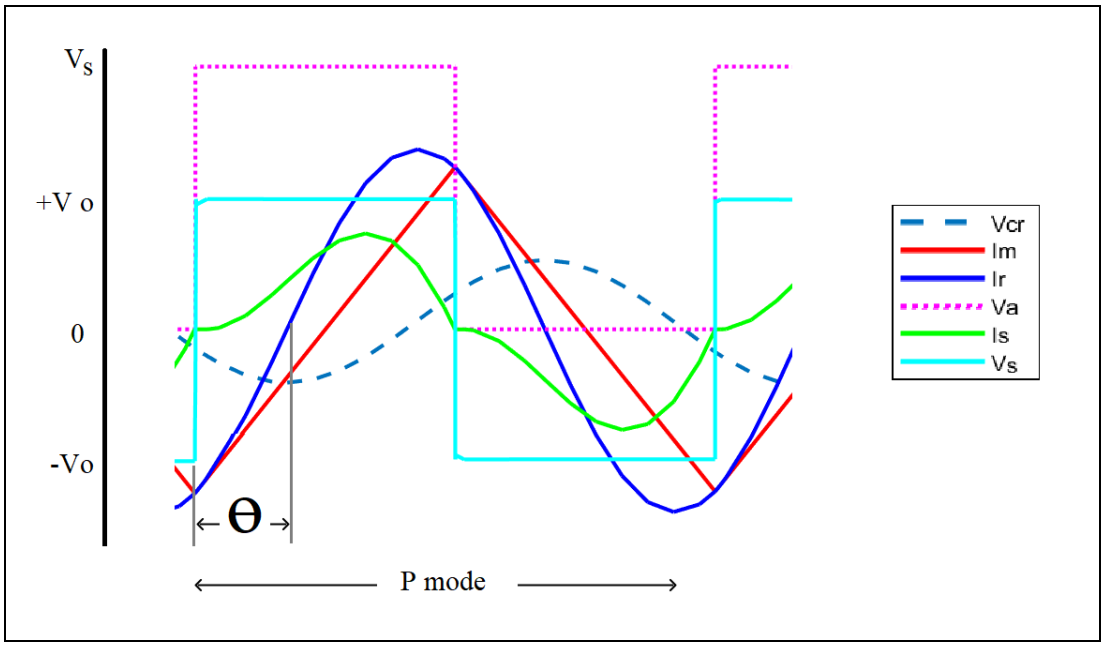


Figure 2.6: Operation modes of the LLC resonant converter: P mode $f_n \approx 1$.

The following equations can be obtained from Kirchhoff's Current Law (KCL) equations for half of the switching period, $0 < t \leq 0.5T_{SW}$ where $T_{SW} = 1/f_{SW}$.

$$V_s' = \frac{V_s}{N} = L_m \frac{dI_m}{dt}$$

$$I_r = \mathrm{I}_{r(peak)} \sin(2\pi f_r t - \Theta)$$

$$I_m = I_m(0) + \frac{V_s}{N} \frac{t}{L_m}$$

$$I_s = \frac{I_r - I_m}{N} \tag{2.16}$$

$$\mathrm{I}_{off} = I_r(0.5T_{sw})$$

$$I_r(0) = I_m(0)$$

$$I_r(0.5T) = I_m(0.5T)$$

$$I_r(0) = -I_r(0.5T)$$

$\mathrm{I}_{off}$ presents the main switch turn-off current, which causes turn-off losses and depends on the value of $C_r$ [60]. From equation (2.16), the magnetising inductance is clamped at the secondary voltage. The corresponding state equation is given below.

$$V_a - V_{cr}(t) - L_r \frac{dI_r}{dt}(t) = \frac{V_s}{N} \tag{2.17}$$

$$C_r \frac{dI_r}{dt} V_{cr}(t) = I_r(t) \tag{2.18}$$

When $t = 0$, $I_r$=$I_m$, then the peak value of the magnetising current can be expressed as below.

$$\mathrm{I}_{r(peak)} \sin(\Theta) = I_{m(peak)} = \frac{V_s}{4\ N\ L_m\ f_{R1}} \tag{2.19}$$

The phase angle Θ of $I_r$ lagging $V_a$ can be expressed as below.

$$\Theta = \sin^{-1}\left(\frac{\mathrm{V_s}}{4\ \mathrm{N}\ \mathrm{L_m}\ \mathrm{f_{R1}}\ \mathrm{I_{r(peak)}}}\right) \tag{2.20}$$

Based on the Law of Conversation of Energy, the energy transferred from $V_{in}$ must be equal to the energy transferred to $R_o$ in each half of $T_{SW}$ where $\mathrm{E}_{in}$, $\mathrm{E}_o$ and $\mathrm{P}_o$ are energy transferred from $V_{in}$, energy observed by $R_o$ and output power, respectively [67]. The equations for $\mathrm{E}_{in}$ and $\mathrm{E}_o$ are given below.

$$\begin{aligned} E_{in} &= \frac{\mathrm{V}_{in}\mathrm{I}_{r(peak)}\cos(\Theta)}{2\pi f_{R1}} \\ E_o &= P_o T_{SW} \\ E_{in} &= E_o \end{aligned} \tag{2.21}$$

The peak value of resonant current ($\mathrm{I}_{r(peak)}$) and the RMS value of resonant current ($\mathrm{I}_{r(RMS)}$) can be expressed when $f_n \approx 1$ [67, 68].

$$\begin{aligned} \mathrm{I}_{r(peak)} &= \sqrt{\left(\frac{V_s}{4.N.L_m}\right)^2 + \left(\frac{N\pi I_s}{2}\right)^2} \\ \mathrm{I}_{r(RMS)} &= \frac{\mathrm{I}_{r(peak)}}{\sqrt{2}} \end{aligned} \tag{2.22}$$

$$\begin{aligned} \mathrm{I}_{s(RMS)} &= \sqrt{\frac{2}{T_{SW}}\int_0^{T_{SW}/2}\left(\frac{I_r - I_m}{N}\right)^2 dt} \\ &= \frac{\sqrt{3}}{24\pi}\sqrt{(5\pi^2 - 48)\left(\frac{V_s}{4.N.L_m}\right)^2 + 12\pi^2 {I_s}^2} \end{aligned} \tag{2.23}$$

Then converter total loss can be calculated as 2.24 for the half-bridge LLC resonant converter. Total loss $P_{loss}$ can be obtained as the sum of primary side switching and conduction losses $P_p$, secondary side rectifier and conduction losses $P_s$, resonant inductor losses $P_{Lr}$ and transformer losses $P_T$ [67]. The equations for $P_{loss}$ is given below.

$$P_{loss} = P_p + P_s + P_{Lr} + P_T$$

$$\begin{aligned} P_{loss} = \mathrm{I}_{r(RMS)}{}^2\left(R_{\,ds(on)} + R_p + R_{Lr}\right) + \mathrm{I}_{s(RMS)}{}^2(R_s) \\ +2\mathrm{I}_{s(RMS)}V_f + \mathrm{I}_{off}2\pi f_{R1}T_{fall} \\ +V_T f_T{}^{\alpha_T} B_T^{\beta_T} \end{aligned} \tag{2.24}$$

$R_p$, $R_s$, $R_{Lr}$ and $R_{\,ds(on)}$ are the primary winding resistance, secondary winding resistance, resonant inductor winding resistance and primary switch (MOSFETs) on resistances, respectively. $\mathrm{I}_{off}$ and $T_{fall}$ are MOSFET turn-off current and MOSFET current fall time. $P_T$ is the core loss of the transformer. $V_T$, $B$, α and β are core volume, maximum flux density, frequency loss and magnetic loss of transformer core. The converter efficiency η be expressed as below.

$$\eta = \frac{P_O}{P_O + P_{LOSS}} \tag{2.25}$$

When $f_n < 1$, the converter operates in Region 2 (high voltage gain region) or Region 3 (hard-switching region), depending on Q [67]. In light load conditions, which means Q is not high, the converter operates in the inductive region, Region 2 and PO mode; the basic current and voltage waveforms are presented in Figure 2.7. The converter operates in P mode for the period $0 < t \leq 0.5T_{R1}$ where $T_{R1=}\, 1/f_{R1}$. The converter operates in O mode for the period $0.5T_{RES1} < t \leq 0.5T_{SW}$.

The resonant current and magnetising current can be obtained as below.

$$I_r = \begin{cases} \mathrm{I}_{r(peak)} \sin(2\pi f_{R1} t - \Theta) & , \quad 0 < t \leq 0.5T_{R1} \\ \dfrac{V_s}{4\,N\,L_m\,f_{R1}} & , \quad 0.5T_{R1} < t \leq 0.5T_{SW} \end{cases} \tag{2.26}$$

$$I_m = \begin{cases} \dfrac{V_s}{N}\,\dfrac{t}{L_m} - \dfrac{V_s}{4\,N\,L_m\,f_{R1}} & , \quad 0 < t \leq 0.5T_{R1} \\ \dfrac{V_s}{4\,N\,L_m\,f_{R1}} & , \quad 0.5T_{R1} < t \leq 0.5T_{SW} \end{cases} \tag{2.27}$$

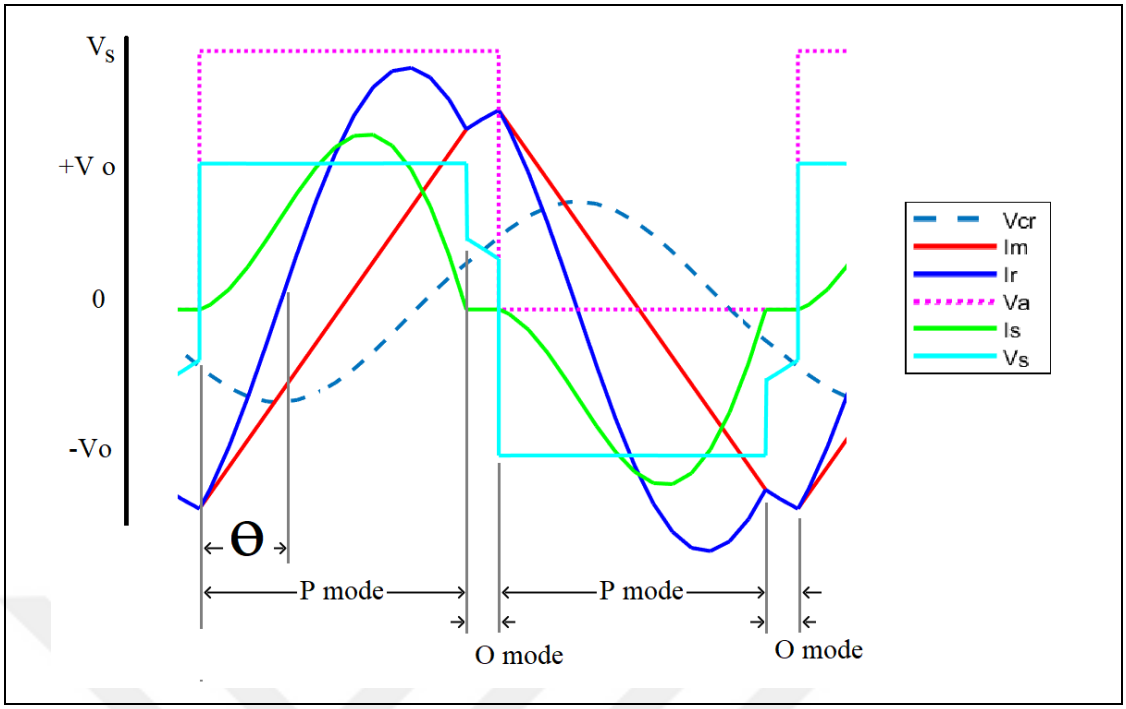


Figure 2.7: Operation modes of the LLC resonant converter PO mode $f_n < 1$.

In O mode, the resonant current charges and discharges $C_Q$ and changes the polarity of $V_s$. When $t = 0$, the resonant current can be expressed as below.

$$I_r(0) = I_{r(peak)} \sin(-\Theta) = -\frac{V_s}{4\,N\,L_m\,f_{R1}} \tag{2.28}$$

During half of $T_{SW}$, the secondary current $I_s$ can be calculated as below.

$$I_s = \frac{2}{T_{SW}} \int_0^{T_{SW}/2} \left| \frac{I_r - I_m}{N} \right| dt \tag{2.29}$$

The phase angle Θ of $I_r$ lagging $V_a$ can be expressed as below.

$$I_{r(peak)} \cos(\Theta) = \frac{N\,\pi\,I_s}{2} \frac{f_{R1}}{f_s} \tag{2.30}$$

$$\Theta = \tan^{-1}\left(\frac{V_s}{2\,\pi\,L_m\,I_s\,f_{R1}\,N^2}\right) \tag{2.31}$$

The peak resonant current $I_{r(peak)}$ can be calculated as below.

$$I_{r(peak)} = \sqrt{\left(\frac{V_s}{4\,N\,L_m\,f_{R1}}\right)^2 + \left(\frac{N\pi I_s}{2}\frac{f_{R1}}{f_s}\right)^2} \tag{2.32}$$

In O mode, since secondary rectifier diodes are turned off, $I_r = I_m$ and then the equations (2.25) and (2.26) can be redefined as below.

$$C_r \frac{dI_r}{dt} V_{cr}(t) = I_r(t) = I_m(t) \tag{2.33}$$

According to the continuity of the signal at the P and O modes and the symmetry of the voltage of the resonant capacitor, $V_s$ can be derived as below.

$$V_s = \frac{V_{in}}{2} + \frac{V_s}{4\,N\,C_r}\,(T_{sw} - T_{R1}) \tag{2.34}$$

Then the normalised voltage gain can be expressed as below [69].

$$|M_{LLC}| = \left|\frac{V_s}{N\,\left({}^{V_{in}}/_{2}\right)}\right| = \frac{1}{\sqrt{\left(\frac{1}{L_n} + 1 - \frac{1}{L_n f_n^2}\right)^2 + \frac{\pi^4}{64} Q^2 (\frac{1}{f_n} - f_n)^2}} \tag{2.35}$$

Depending on the increased value of Q, the converter starts to operate first in PON and then PN mode. In heavier load conditions, Θ gets closer to 0. When Θ=0, the converter operates in PON mode, as presented in Figure 2.8. At this point, the converter operates in the boundary of the inductive region and the capacitive region, so the ZVS condition of the main switches is lost.

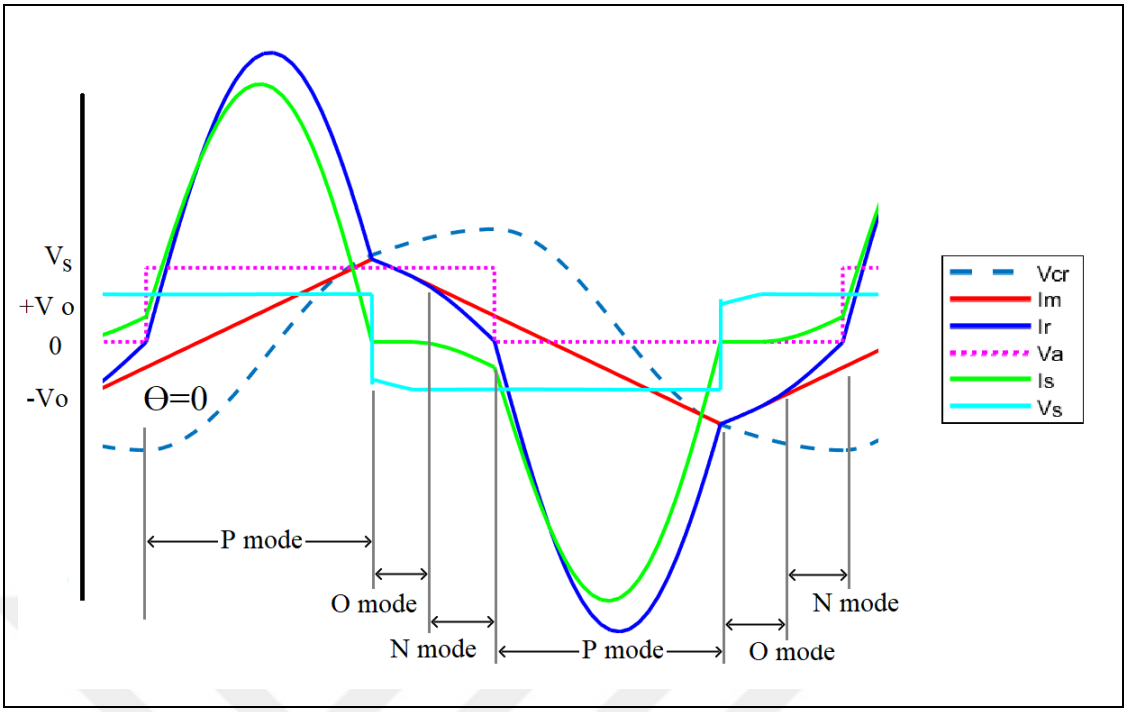


Figure 2.8: Operation modes of the LLC resonant converter: PON mode $f_n < 1$.

In heavy load conditions, which means Q is very high, the converter operates in Region 3, and $V_a$ is lagging $I_r$ (Θ<0), as presented in Figure 2.9. In this condition, the main switches can not operate in ZVS condition. Region 3 is the hard-switching region, and it is not analyzed.

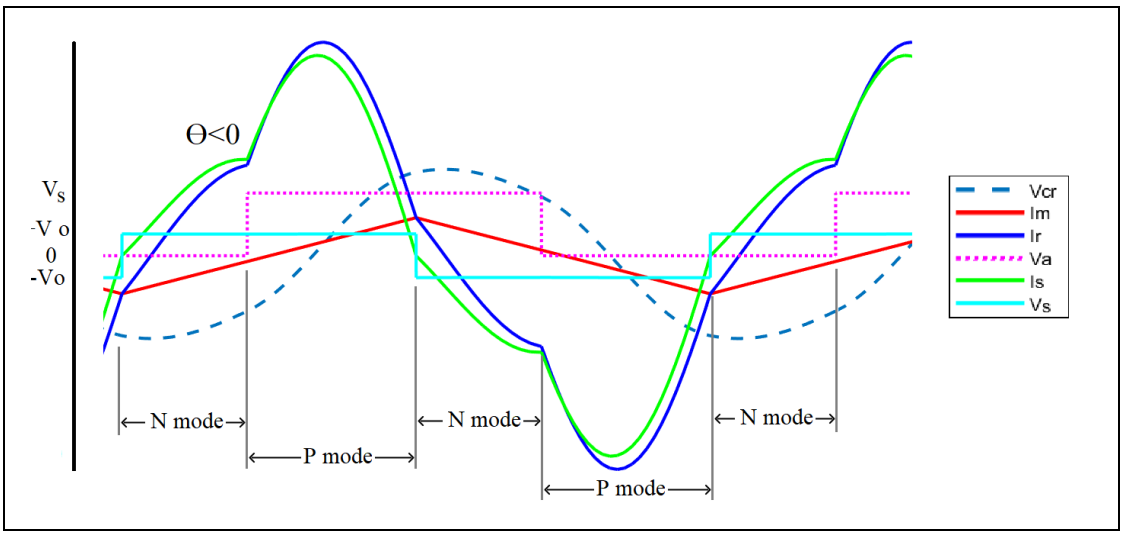


Figure 2.9: Operation modes of the LLC resonant converter: PN mode $f_n < 1$.

When $f_n > 1$, the converter operates in Region 1 (low voltage gain region) and in NP mode. The basic current and voltage waveforms in this form are presented in Figure 2.10. The ain switches always operate in ZVS condition.

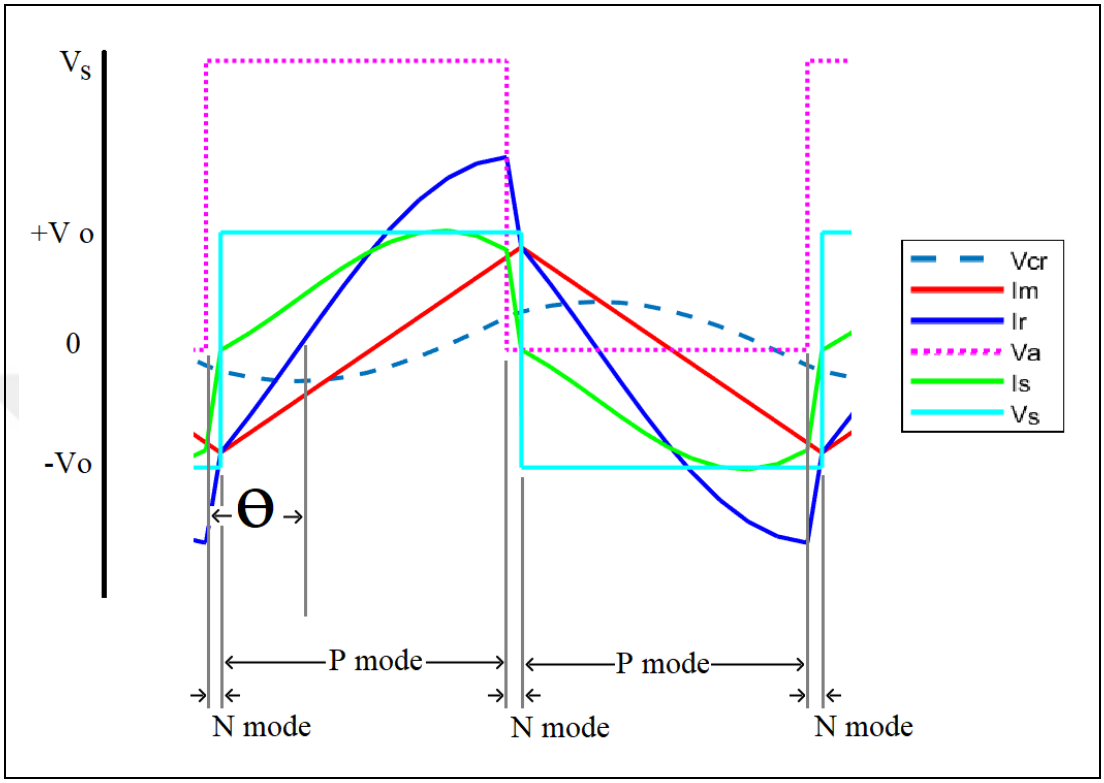


Figure 2.10: Operation modes of the LLC resonant converter: NP mode $f_n > 1$.

### 2.2.3. Converter Conduction States

For simplifying the analysis of current and voltage waveforms in the operation region, all elements are considered ideal, and the parasitic elements of the transformer and rectifier network are neglected. Effects of the parasitic elements of the transformer and rectifier network will be presented in section 2.2.4. To ensure the main switches operate in ZVS condition, the analysis should be in PO mode, Region 2. The current and voltage waveforms for region 2 are presented in Figure 2.11.

First state ($t_0 \sim t_3$): P state of positive polarity

($t_0 \sim t_1$): Before $t_0$ , $I_m$ is in negative polarity and flows through $D_{q1}$ and $V_{ds1}$ is almost zero. State starts with $Q_1$ is turned on at $t_0$ in ZVS condition. $I_m$ keeps flowing from $D_{Q1}$ and increases linearly. $L_r$ resonates with $C_r$, and $C_r$ starts to be charged.

The rectifier network diodes start to conduct. The energy is transferred to the secondary side.

($t_1 \sim t_2$): The status of $Q_1$ and $Q_2$ is not changed. $I_r$ reaches its positive peak value and the polarity of $I_m$ changes from negative to positive polarity at $t_2$.

($t_2 \sim t_3$): Since $f_{sw} < f_r, I_r = I_m$ at $t_3$. Secondary rectifier network diodes are turned off. Thus the energy transfer to the secondary side stops. $C_r$ is fully charged to the positive peak value.

Second state ($t_3 \sim t_6$): O state of positive polarity

($t_3 \sim t_4$): Converter starts to operate in the O stage. $I_m$ keeps flowing and is equal to $I_r$. $I_m$ reaches its positive peak value at $t_4$. This state ends at $t_4$ when $Q_1$ is turned off.

($t_4 \sim t_5$): $I_m$ continues to flow and simultaneously charges $C_{\mathrm{Q1}}$ to $V_{\mathrm{s}}$ and discharges $C_{\mathrm{Q2}}$ to 0.

($t_5 \sim t_6$): $C_{\mathrm{Q1}}$ charges and $C_{\mathrm{Q2}}$ discharges are ended at $t_6$. Thus $V_{\mathrm{ds1}} \approx V_{\mathrm{s}}$ and $V_{\mathrm{ds2}} \approx 0$. $I_m$ keeps flowing through $D_{Q2}$.

Third state ($t_6 \sim t_9$): P state of negative polarity

($t_6 \sim t_7$): At $t_6$, $V_{\mathrm{ds2}} \approx 0$ and $Q_2$ is turned on in ZVS condition. $I_m$ continues to flow through $D_{Q2}$ and decreases linearly. The rectifier network diodes start to conduct. The energy is transferred to the secondary side.

($t_7 \sim t_8$): The status of $Q_1$ and $Q_2$ is not changed. $I_r$ reaches its negative peak value, and the polarity of $I_m$ changes from positive to negative polarity at $t_8$.

($t_8 \sim t_9$): Since $f_{sw} < f_r$, $I_r = I_m$ at $t_9$. Secondary rectifier network diodes are turned off. Thus the energy transfer to the secondary side stops. $C_r$ is fully charged to the negative peak value.

Fourth state ($t_9 \sim t_0$): O state of negative polarity

($t_9 \sim t_{10}$): The converter starts to operate in the O stage. $I_m$ continues to flow and is equal to $I_r$. $I_m$ reaches its negative peak value at $t_{10}$. This state ends at $t_{10}$ when $Q_2$ is turned off.

($t_{10} \sim t_{11}$): $I_m$ continues to flow and simultaneously charges $C_{\mathrm{Q2}}$ to $V_{\mathrm{in}}$ and discharges $C_{\mathrm{Q1}}$ to 0.

($t_{11} \sim t_0$): $C_{\mathrm{Q2}}$ charges and $C_{\mathrm{Q1}}$ discharges are complited at $t_0$. Thus $V_{\mathrm{dsQ2}} \approx V_{\mathrm{s}}$ and $V_{\mathrm{dsQ1}} \approx 0$. $I_m$ continues to flow through $D_{Q1}$.

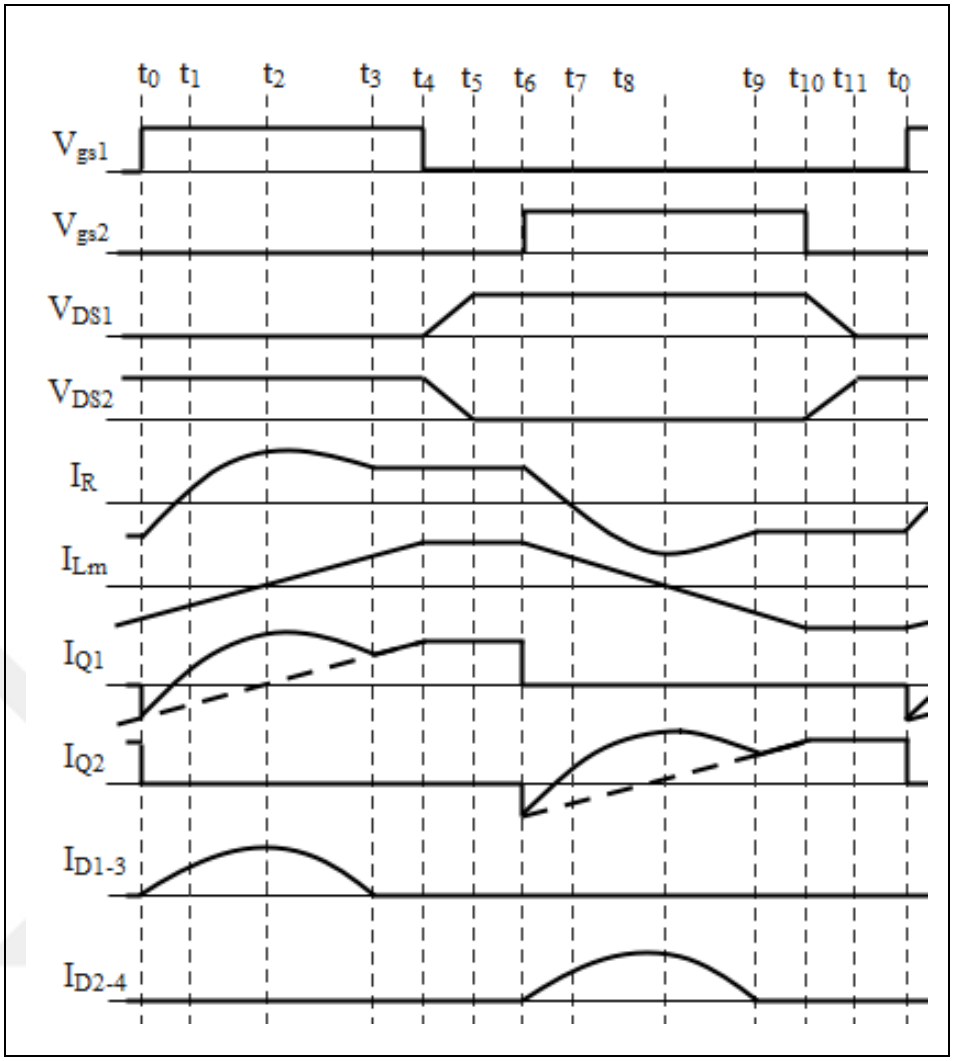


Figure 2.11: Current and voltage waveforms when the LLC resonant converter operates in region 2.

When all of the main switches in the switching network are off state at ($t_4 \sim t_6$) and ($t_{10} \sim t_0$), this period is called dead time. In this period, stored energy in resonant network charges and discharges $C_{Q2}$ and $C_{Q1}$. The conduction states of the LLC resonant converter are shown in Figure 2.12 and Figure 2.13.

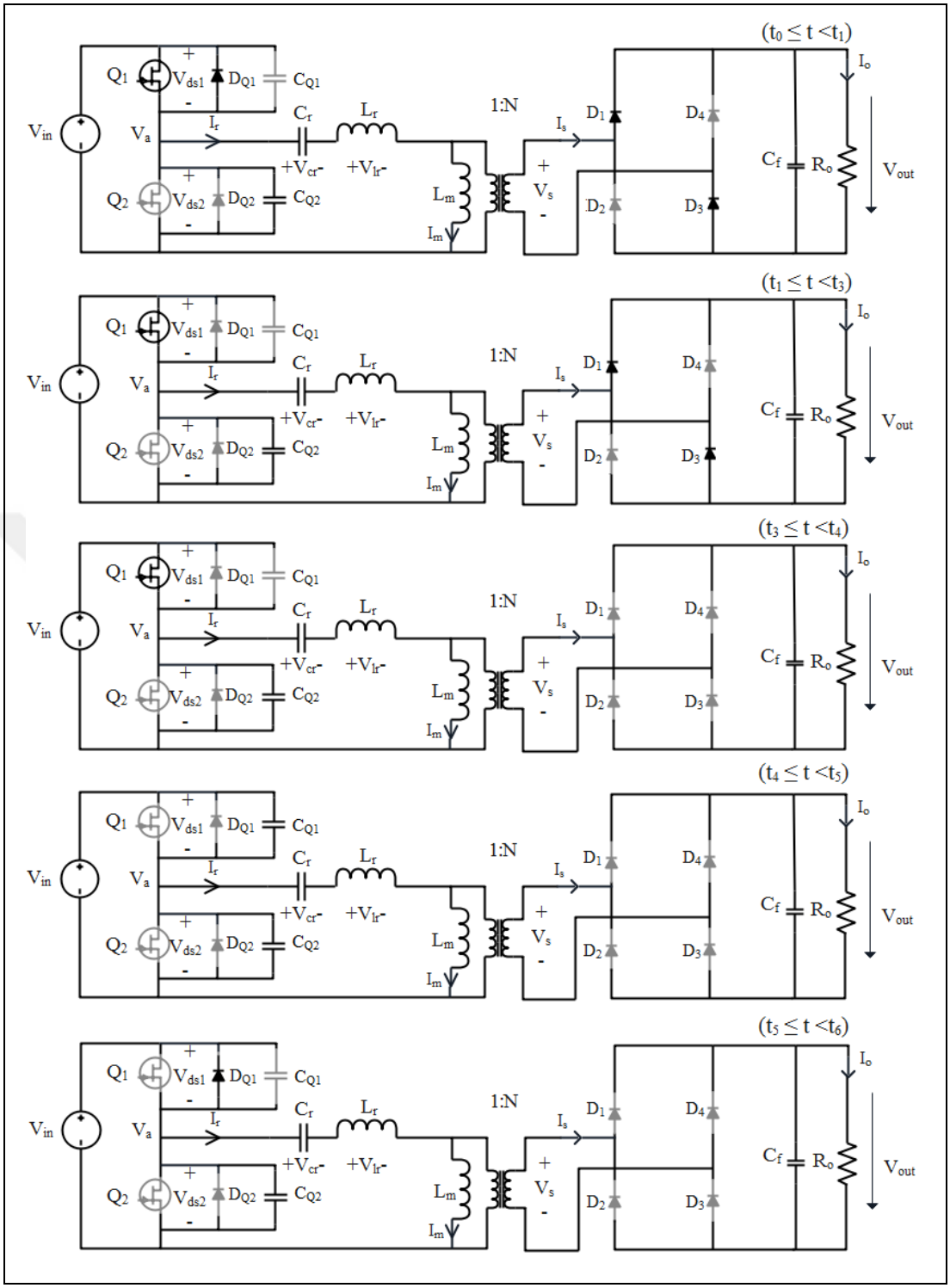


Figure 2.12: The conduction states of the LLC resonant converter for positive polarity.

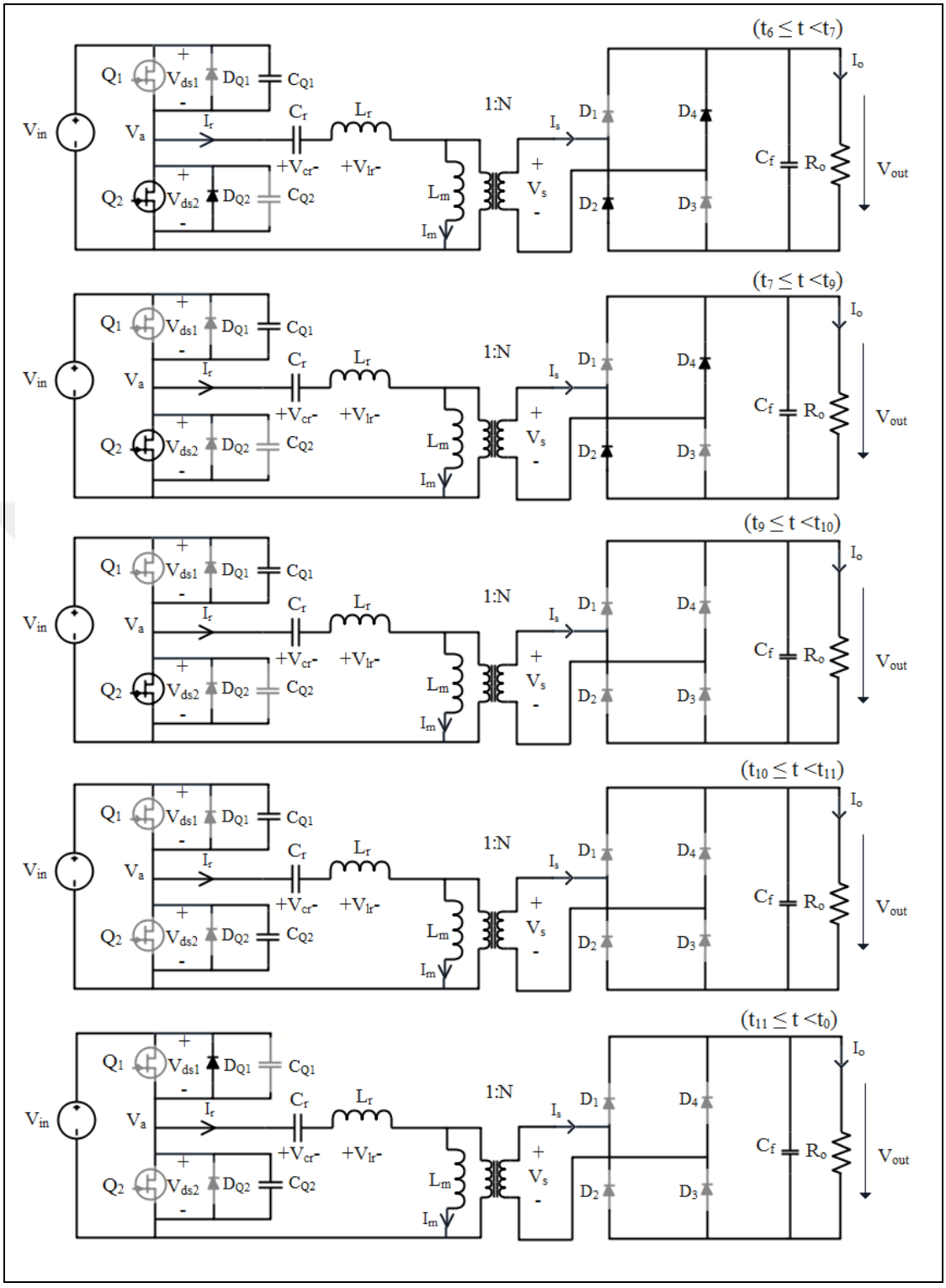


Figure 2.13: The conduction states of the LLC resonant converter for negative polarity.

### 2.2.4. Main Switches Soft- Switching Condition

ZVS condition of the main switches depends on the complete discharge of the parasitic capacitances during dead time. ZVS is achieved if the switches are turned on while the resonant current continues to flow through $D_Q$. The effects of the equivalent transformer capacitance ($C_{TR}$) and secondary rectifier network junction capacitance must be considered. $C_{j1}$-$C_{j4}$ are the junction capacitances of secondary rectifier diodes presented in Figure 2.1. $C_J'$ is the impact of $C_{j1-4}$ referred to as the primary side. The equivalent circuit of the LLC resonant converter, including the parasitic effects, is presented in Figure 2.14. Stray capacitance ($C_{Stray}$) is the sum of $C_J'$ and $C_{Stray}$. The equations for $C_J'$ and $C_{Stray}$ are given below.

$$C_J' = N^2(C_{j1} + C_{j2} + C_{j3} + C_{j4}) \tag{2.36}$$

$$C_{Stray} = C_J' + C_{TR} \tag{2.37}$$

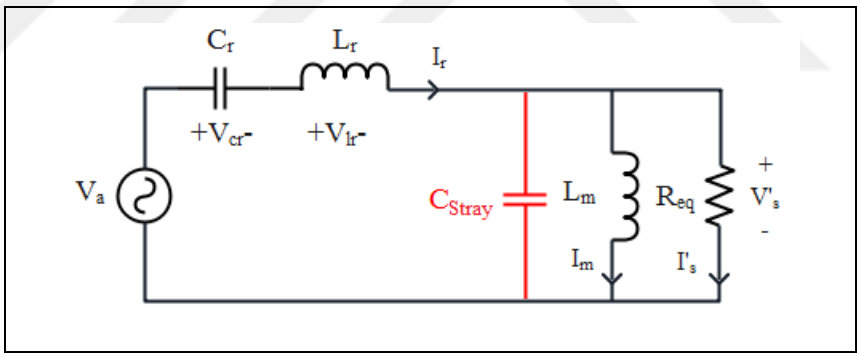


Figure 2.14: The simplified circuit of the LLC resonant converter, including the parasitic components.

The LLC resonant converter must operate in the inductive region as described in Section 2.2.1. $Z_n$ and $Z_{in}$ equations have been expressed in equations (2.9) and (2.10.). $C_{Stray}$ changes the characteristic of $Z_{in}$. The impact of $C_{Stray}$ to $Z_{in}$ is presented in Figure 2.15 using equations (2.38) and (2.39).

$$Z_{in} = sL_r + \frac{1}{sC_r} + sL_m // R_{eq} // \frac{1}{sC_{eq}} \tag{2.38}$$

$$\mathrm{Z}_n = \frac{Z_{in}}{Z_0} = \left( \frac{{f_n}^2 {L_n}^2 \mathrm{Q}}{\left(L_n C_n {f_n}^2 - 1\right)^2 + {f_n}^2 {L_n}^2 \mathrm{Q}^2} \right) + j\left( f_n - \frac{1}{f_n} + \frac{f_n L_n - {L_n}^2 C_n {f_n}^3}{\left(L_n C_n {f_n}^2 - 1\right)^2 + {f_n}^2 {L_n}^2 \mathrm{Q}^2} \right) \tag{2.39}$$

$$C_n = {C_{stray}}/{C_r} \tag{2.40}$$

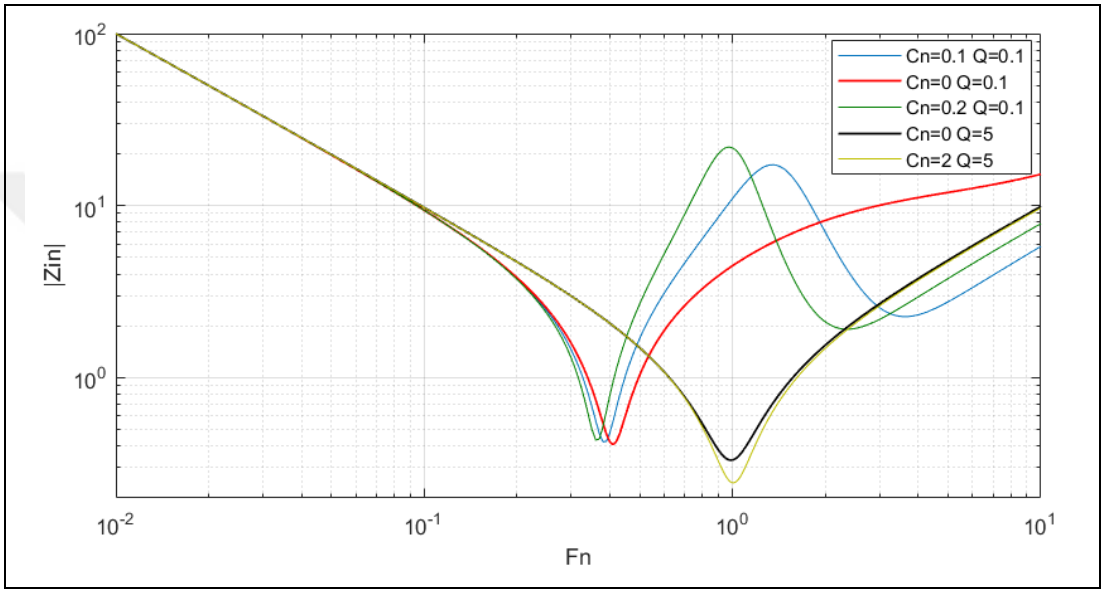


Figure 2.15: The frequency characteristic of normalised input impedance for the LLC resonant converter, including parasitic components.

The effect of $C_{Stray}$ depends on the value of Q. In heavy load conditions, $C_{Stray}$ effects are limited to the characteristics impedance of the converter. Conversely, in light load conditions, $C_{Stray}$ affects the operation region of the converter. When the imaginary part of $\mathrm{Z}_n$ is 0, the boundary of the capacitive and the inductive region can be obtained [68]. The imaginary part of $\mathrm{Z}_n$ is given below.

$$f_n - \frac{1}{f_n} + \frac{f_n L_n - {L_n}^2 C_n {f_n}^3}{\left(L_n C_n {f_n}^2 - 1\right)^2 + {f_n}^2 {L_n}^2 \mathrm{Q}^2} = 0 \tag{2.41}$$

Then, the following equations can be derived.

$$Q_{min} = \sqrt{\frac{L_n C_n {f_n}^2 - 1}{L_n({f_n}^2 - 1)} \frac{\left(L_n C_n {f_n}^2 - 1\right)^2}{{f_n}^2 {L_n}^2}} \tag{2.42}$$

$$\mathrm{Q} = \sqrt{\frac{L_r}{C_r}} \frac{1}{\mathrm{R}_{eq}} = 2\pi f_{R1} L_r \frac{1}{\mathrm{R}_{eq}} = \frac{2.\pi f_{R1} L_m}{L_n \mathrm{R}_{eq}} \tag{2.43}$$

$$L_m < \frac{L_n \mathrm{R}_{eq}}{2\pi f_{R1}} \sqrt{\frac{L_n C_n {f_n}^2 - 1}{L_n({f_n}^2 - 1)} \frac{\left(L_n C_n {f_n}^2 - 1\right)^2}{{f_n}^2 {L_n}^2}} \tag{2.44}$$

When $L_m$ is selected as defined in equation (2.44), the converter operates in the inductive region boundary. According to uncertainties, $L_m$ must be chosen with a margin [68].

In the dead time period ($T_d$), the resonant current equals magnetising current. Resonant current charges and discharges $C_{\mathrm{Q}}$ and changes the polarity of $V_s$. From equations (2.25) and (2.26), the value of $L_m$ can be calculated with the following equation.

$$I_r = I_m = \frac{V_s}{4NL_m f_{R1}} > 2C_{\mathrm{Q}} \frac{V_{in}}{T_d} + 2C_{Stray} \frac{V_s}{NT_d} \tag{2.45}$$

$$L_m < \frac{V_s}{8Nf_{R1}\left(C_{\mathrm{Q}} \frac{V_{in}}{T_d} + C_{Stray} \frac{V_s}{NT_d}\right)} \tag{2.46}$$

When the converter is operating at full load, minimum frequency and minimum impedance angle Θ, the value of $L_m$ can be derived with the following equation from equations (2.31) and (2.32).

$$L_m \leq \frac{V_s f_n}{2\pi N^2 I_s f_{R1} \tan(2\pi f_{R1} T_d)} \tag{2.47}$$

The principle of the resonant converter is based on resonant circuits filtering the higher harmonics of square wave voltage $V_a$. The impact of $C_{stray}$ of circuit elements for high-voltage applications is higher than that of low-voltage applications. Thus,

$C_{stray}$ and $L_m$ create a parasitic resonant circuit, which causes oscillations and voltage spikes. The frequency of the parasitic resonant circuit is $f_{pp}$ and is calculated below.

$$f_{pp} = \frac{1}{2\pi\sqrt{L_m C_{stray}}} \tag{2.48}$$

When the converter operates in P mode, the impact of the parasitic resonant circuit is low. When $f_{sw}$ is close to $f_{pp}$ or $f_{pp} < f_{sw}$, the parasitic resonant circuit causes oscillations and voltage spikes, so to loss of ZVS on primary MOSFETs and to lead voltage regulation problems. When $f_{pp} \gg f_{sw}$, the parasitic resonant circuit causes small oscillations, and the effect of the circuit is limited.

Conversely, when the converter operates in O mode or N mode, the impact of the parasitic resonant circuit is very high. The period of parasitic resonant frequency is $T_{pp}$. When $T_{pp} < T_d$, the parasitic resonant circuit causes small oscillations, and the effect of the circuit is limited.

Decreasing the effect of $C_n$ on the converter is possible with two conditions. The maximum value of $L_m$ is limited by (2.41), (2.46) and (2.47) and the minimum value of $L_m$ is limited by the flux density of the core and airgap. Increasing flux density is limited by core saturation. Increasing air gap causes higher winding losses, as described in Section 3.1. Increasing $L_r$ and $C_r$ significantly decreases $f_{sw}$. Therefore, the value of $C_{stray}$ should be determined, evaluated, and minimized.

## 2.3. Simulations

The LLC resonant converter parameters are calculated using the parameter selection criterion in Section 2.2. The converter parameters are listed in Table 2.1.

Table 2.1: The LLC resonant converter simulation parameters.

| Parameter | Value |
|---|---|
| $V_{in}$ | 360 V |
| $V_{out}$ | 12000 V |
| $P_{out}$ | 1200 W |
| $L_r$ | 78.4 µH |
| $C_r$ | 66 nF |
| $C_{stray}$ | 0-13nF |
| $C_Q$ | 1 nF |
| $C_j$ | 10 pF |
| $L_m$ | 286 µH |
| $f_{res}$ | 70 kHz |
| $f_{SW}$ | 45–150 kHz |

Figures 2.16 and 2.17 show the current and voltage waveforms when the converter operates at the resonant frequency. $C_{stray}$ effect on ZVS condition is limited at the resonant frequency. The simulations show that a high $C_{stray}$ causes large distortions in the current and voltage waveforms for the entire operating frequency range. The simulations show that distortions are very high under light-load conditions because of oscillations between $C_{stray}$ and $L_r$.

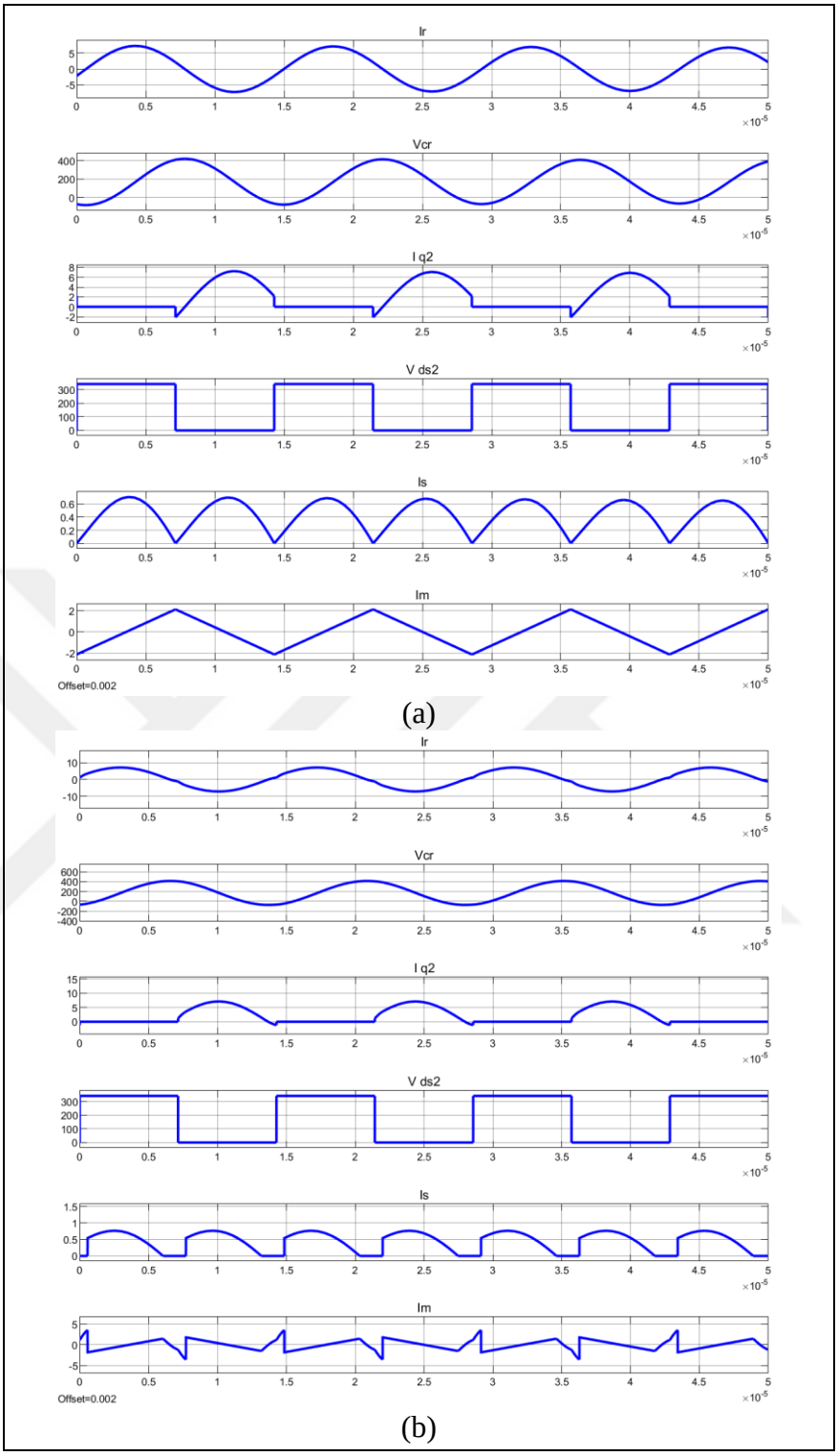


Figure 2.16: The LLC resonant converter operates at resonant frequency Q = 1: (a) $C_n = 0$, (b) $C_n = 0.2$.

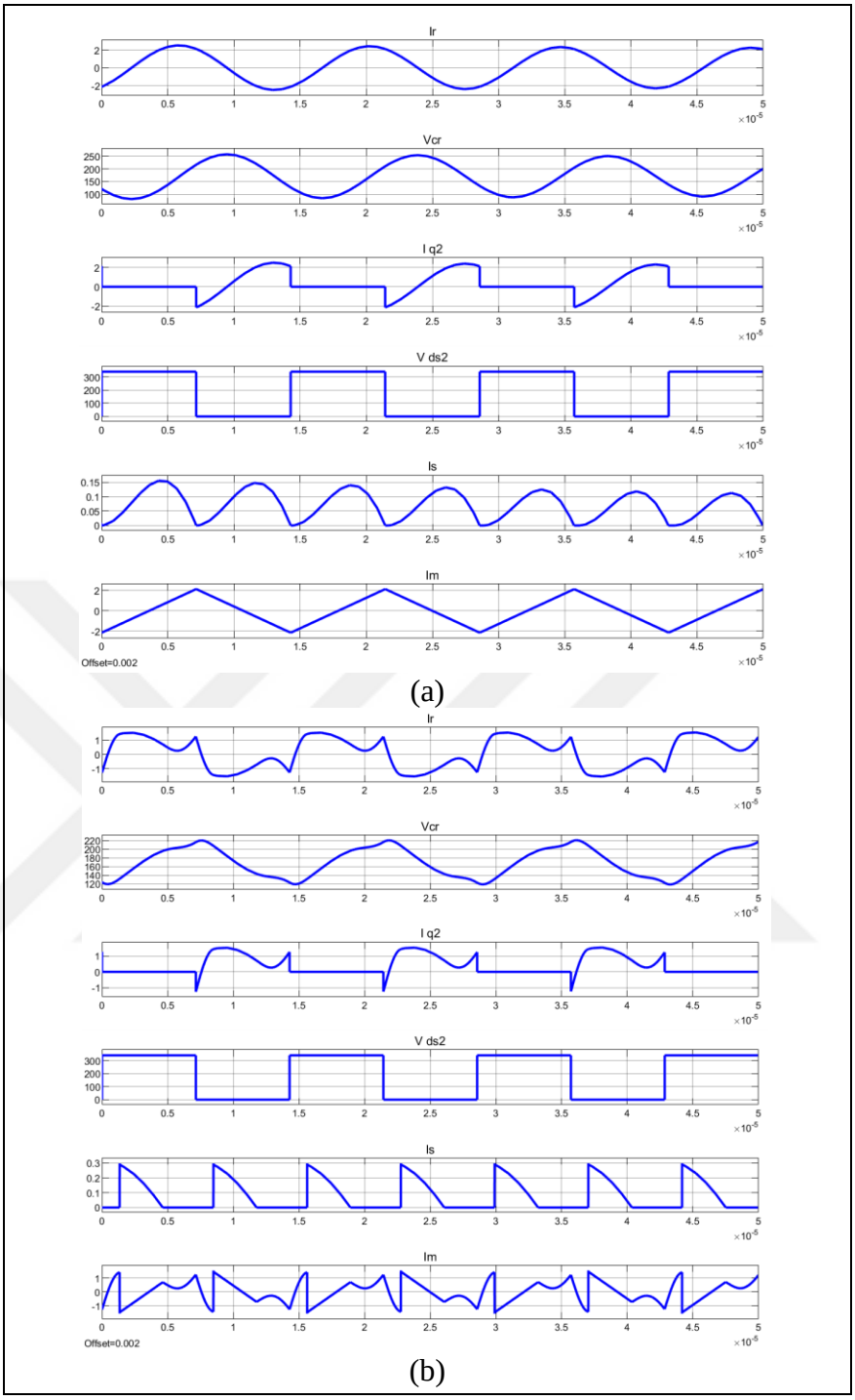


Figure 2.17: The LLC resonant converter operates at resonant frequency Q = 0.1: (a) $C_n = 0$, (b) $C_n = 0.2$.

Figure 2.18 presents the current and voltage waveforms when the converter operates below the resonant frequency. The simulations show that a high $C_{stray}$ causes large distortions in the current and voltage waveforms for the entire operating frequency range.

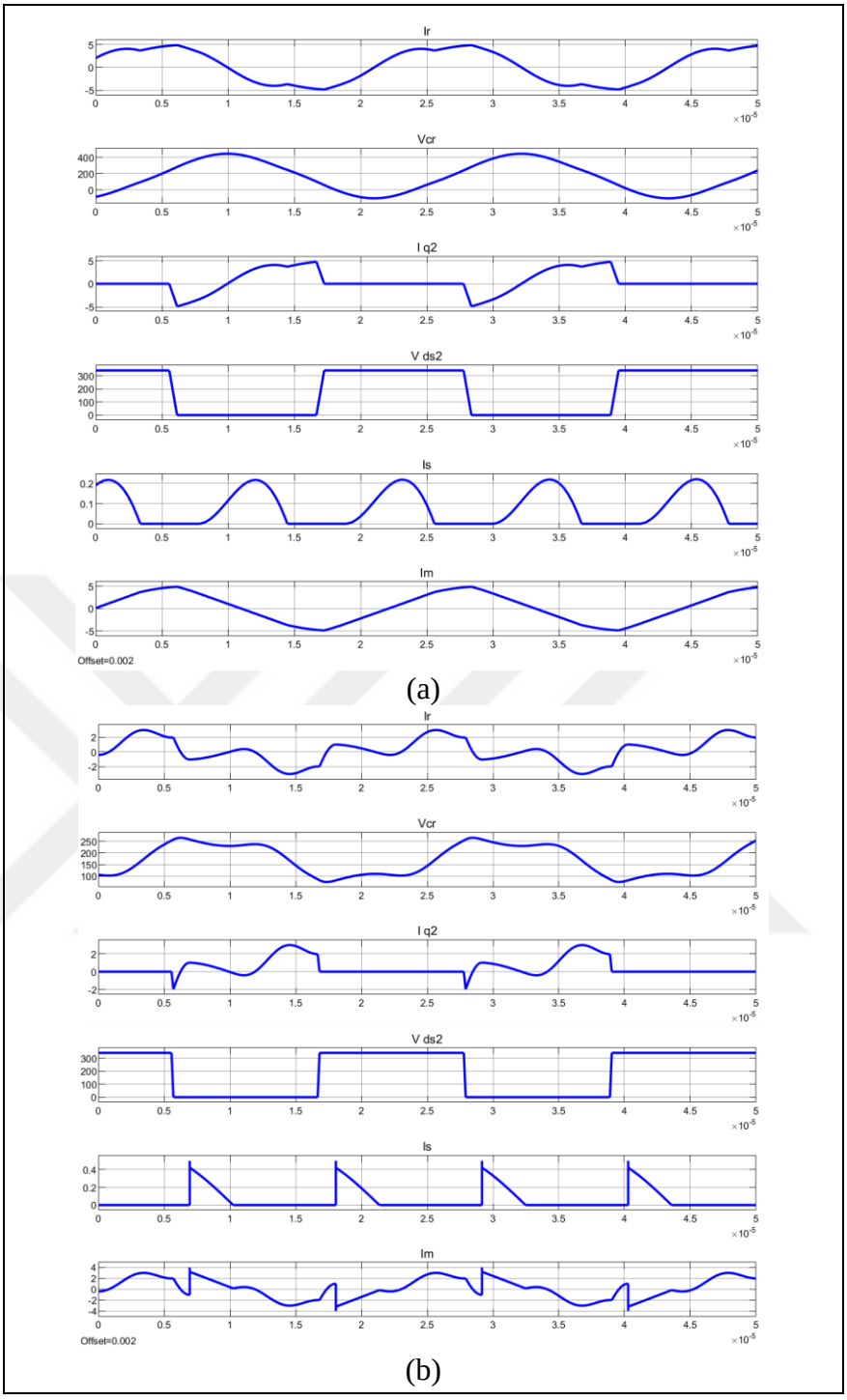


Figure 2.18: The LLC resonant converter operates below resonant frequency at 45 kHz Q = 0.1: (a) $C_n = 0$, (b) $C_n = 0.2$.

Figure 2.19 presents the current and voltage waveforms when the converter operates above the resonant frequency. The simulations show that after the switching frequency reaches 1.5 times the resonant frequency, the resonant tank leaves the inductive region, which is not suitable for the LLC resonant circuit and primary MOSFETs. Therefore, waveform distortions are extremely high.

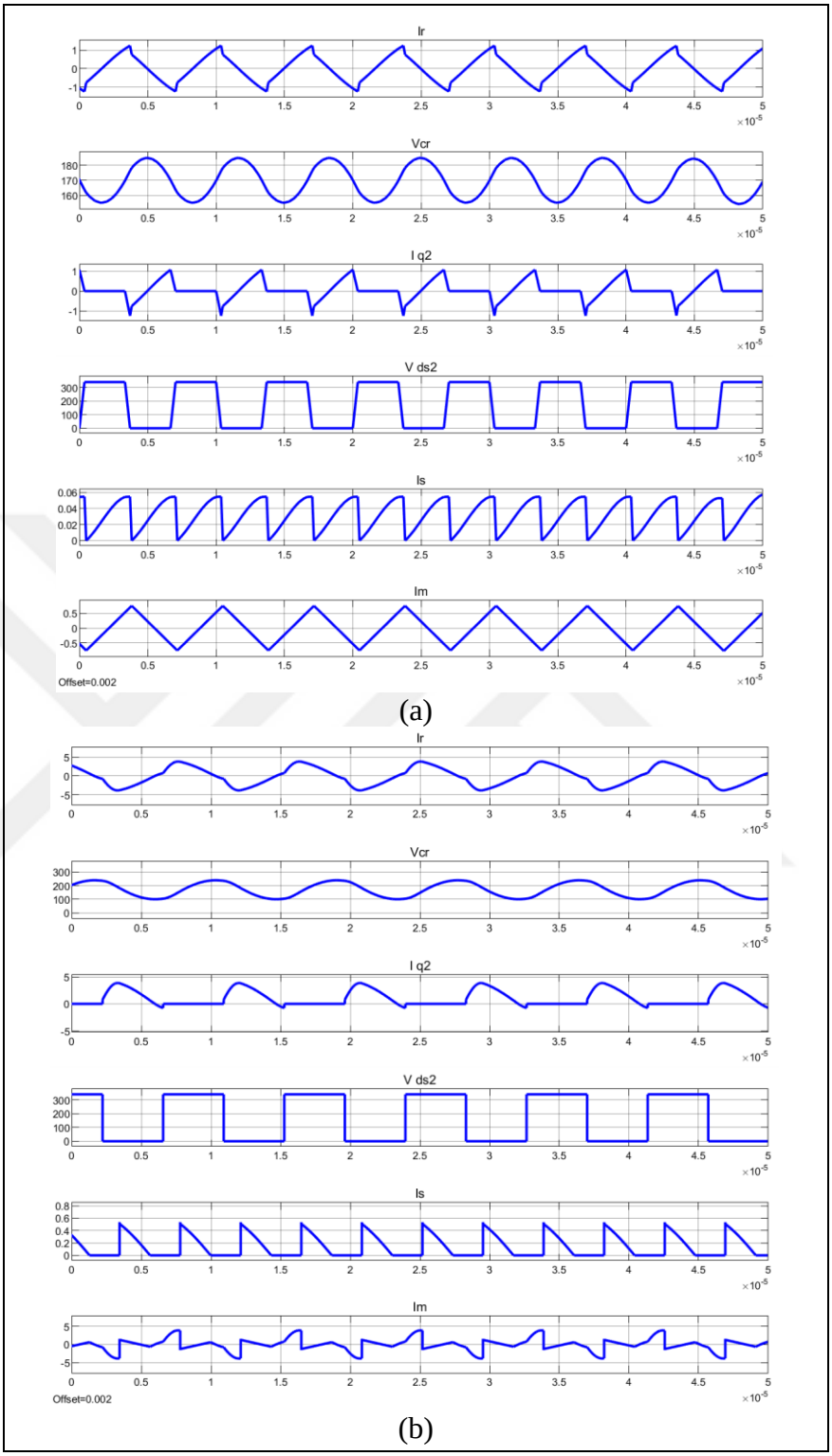


Figure 2.19: The LLC resonant converter operates above resonant frequency Q = 0.1: (a) $C_n = 0$, $f_n = 2$ (b) $C_n = 0.2$ $f_n = 1.5$.

FHA analysis is only applicable when the parasitic capacitance effects and values are lower than those of the main resonant elements. In Figure 2.20, the normalised voltage gain curve of the LLC resonant circuit is shown in the design load and frequency range according to the FHA, while the quality factor varies. Since the parasitic effects were neglected, the voltage gain decreased proportionally to the frequency increment even under light-load conditions above the resonant frequency. ZVS on the primary-side switches were achieved specifically under light-load conditions, whereas $f_n > 1$.

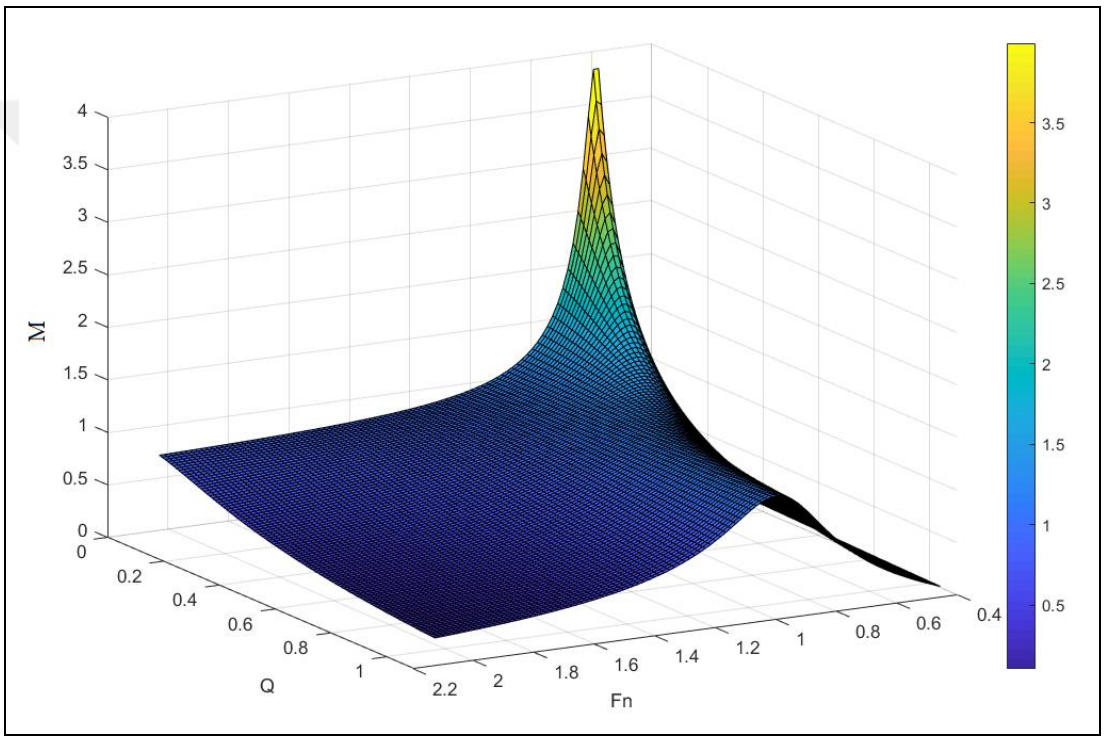


Figure 2.20: The LLC resonant converter normalized voltage gain.

Figure 2.21 shows the normalized voltage gain curve for the designed load and frequency range including the different values of $C_{stray}$ while the quality factor varies. The normalized voltage gain decreased even at the resonance frequency. The normalized voltage gain above the resonant frequency increases slightly in proportion to the switching frequency under light-load conditions where $C_n$ is equal to 0,1. The normalized voltage gain above the resonant frequency increases excessively in proportion to the switching frequency under light-load conditions where $C_n$ is equal to 0,5. The operating frequency limits of the LLC resonant circuit are decreased if $C_n$ is increased.

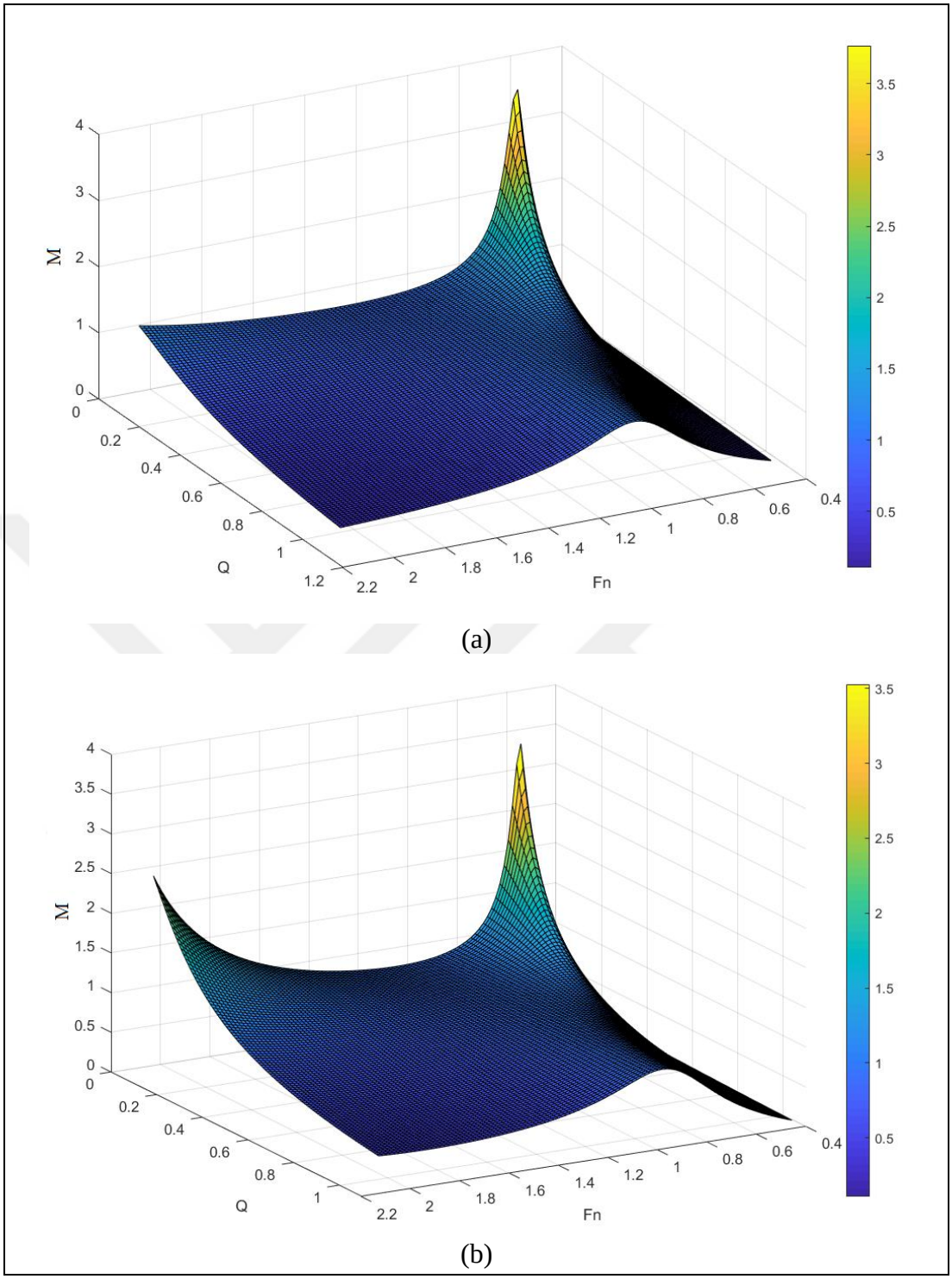


Figure 2.21: The LLC resonant converter normalized voltage gain with the effect of $C_n$ :(a) $C_n$=0.1, (b) $C_n$=0.5.

Figure 2.22 shows the effect of $C_n$ change under light-load conditions on the mode of operation of the LLC resonant converter and over the frequency limit $f_{max}$ where soft switching is lost under any circumstance. $C_{stray}$ causes a high primary charge, distortion of the current and voltage waveforms on the primary side, and loss

of ZVS in the primary-side switches, particularly when $f_n$ >1 under light load conditions. As $C_{stray}$ increases, the frequency ($f_{max}$) where ZVS is lost gets close to resonant frequency.

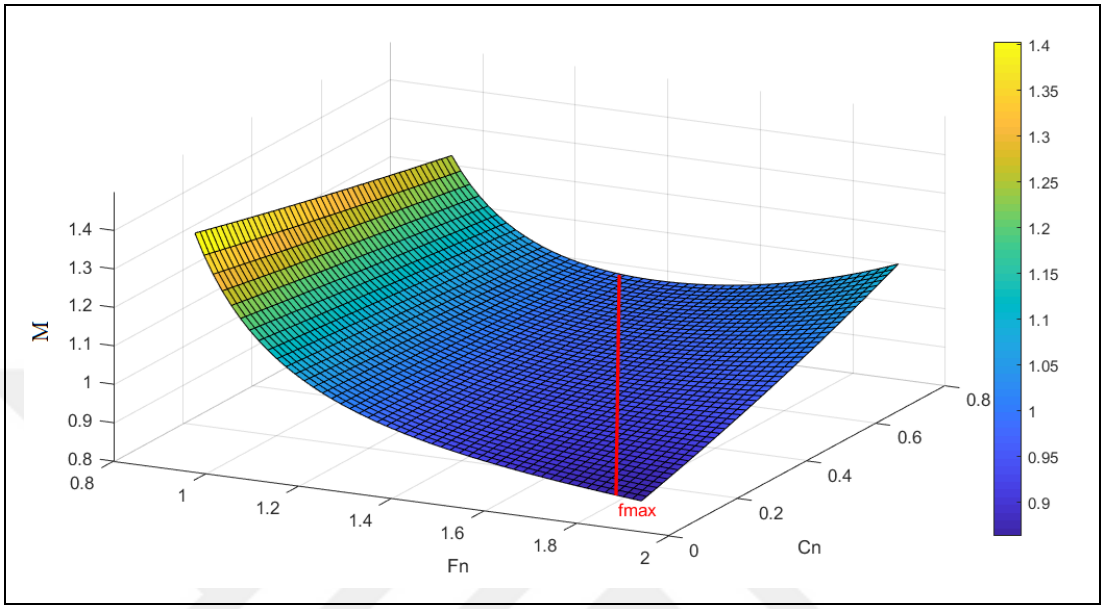


Figure 2.22: The LLC resonant converter voltage gain with effect $0.1 \leq C_n \leq 0.6$ while Q=0.1.

## 2.4. Summary

This section has presented a detailed analysis of the LLC resonant converter based on FHA. The circuit description, impedance characterization, operation regions and converter conduction states have been analyzed. Furthermore, the effects of the parasitic capacitance of the transformer on the LLC resonant converter have been shown. The theoretical considerations have also been verified by the simulations.

# 3. MODELING HIGH-FREQUENCY TRANSFORMER AND RECTIFIER NETWORK

This section describes the high-frequency transformer and the rectifier network parasitic elements, which should be considered for the operation of the LLC resonant converters. The transformer model and rectifier network effects are described. Also, multi-winding transformer parameters are explained.

## 3.1. High-Frequency Transformer

The modeling of the two-port high-frequency transformers has been evaluated in many studies [11]-[13]. A model of the transformer, including the parasitic elements, is presented in Figure 3.1 [12].

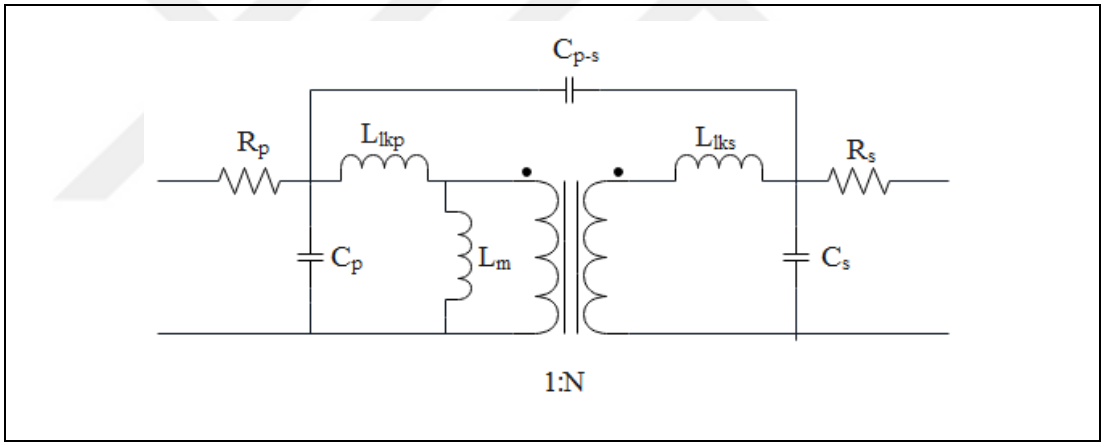


Figure 3.1: A high-frequency transformer model including the parasitic elements.

N is defined as the turn ratio. The inductive elements $L_m$, $L_{lkp}$, and $L_{lks}$ represent mutual, primary winding leakage, and secondary winding leakage inductances, respectively. Inductive elements are defined as magnetic field effects that can be directly measured at low frequencies using short-circuit and open-circuit tests to minimize the effects of capacitive elements. After the measurements, the primary and secondary leakage inductances can be summed into a single equivalent leakage inductance component, $L_{lk}$, referred to the primary side. The equation for $L_{lk}$ is given below.

$$L_{lk} = L_{lkp} + {}^{L_{lks}}/_{N^2} \tag{3.1}$$

In the LLC resonant converter, a gapped core must be used to integrate both $L_{lk}$ and $L_m$ to the resonant circuit and to adjust the resonant parameters as defined in Section 2. $L_m$ value is limited by core flux density and air gap. $L_{lk}$ value can be optimized by winding arrangement and conductor spacing.

The windings of the transformer have a DC resistance ($R_{dc}$) which depends on winding length, cross section ($A_w$) area and material of the conductor. ρ is the resistivity of the conductor. $I$ represents the current that flows the through the conductor. $t$ and $w$ depict the thickness and width of the conductor, respectively. MLT stands for the mean length of turns. Current density ($J$) is uniform through the conductor ($J = I/A_w$ , $A_w = t.w$) for DC current. The equation for $R_{dc}$ is given below.

$$R_{dc} = \frac{\rho\ (\mathrm{MLT})}{t.w} = \frac{\rho\ (\mathrm{MLT})}{A_w} \tag{3.2}$$

AC resistance ($R_{ac}$) of the windings in transformers increases with high frequency due to proximity effects, including the skin effect and the proximity effect losses. Current density ($J$) is not uniform through the conductor for AC current because of the skin effect and the proximity effect. $R_{ac}$ was described only for sinusoidal current for a transformer by Dowell and Ferreira [25], [26]. The ratio of $R_{ac}$ to $R_{dc}$ including the skin effect of an infinite foil conductor with fixed frequency sinusoidal current is presented in equation (3.3) [36]. $t$, δ and Δ are foil thickness and the skin depth and the ratio of $t$ to δ, respectively.

$$\frac{R_{ac}}{R_{dc}} = \frac{\Delta}{2}\,\frac{\sinh(\Delta)+\sin(\Delta)}{\cosh(\Delta)-\cos(\Delta)}\ ,\ \Delta = t/\delta \tag{3.3}$$

Based on Dowell's assumptions, the ratio of $R_{ac}$ to $R_{dc}$ is represented by $F_R$ for the high-frequency transformers. $p$ is the number of layers and can be defined as a ratio magneto motive force (MMF) in the lowest to the highest layer of MMF

distribution. $F_R$ stands for the proximity effect of $p^{th}$ layers for foil conductors and fixed frequency sinusoidal current defined as in [25], [26], [28]. The equation for $F_R$ is given below.

$$F_R = \frac{R_{ac,p}}{R_{dc,p}} = \frac{\Delta}{2}\left[\frac{\sinh(\Delta)+\sin(\Delta)}{\cosh(\Delta)-\cos(\Delta)} + \frac{2}{3}(p^2-1)\frac{\sinh(\Delta)-\sin(\Delta)}{\cosh(\Delta)+\cos(\Delta)}\right] \tag{3.4}$$

The proximity effect losses dominate the AC losses with the increasing number of layers. The proximity effect depends on the winding arrangement, the layer porosity factor and layer distances [27], [32]. MMF distribution of the y-axis different winding arrangement is presented in Figure 3.2, where winding symmetry along the y-axis and each primary and secondary turn ratio are the same. $t_p$ and $t_s$ are the foil thicknesses on primary and secondary windings, respectively. $h$ and $h_{p-s}$ are the insulator thickness between layers and between primary and secondary windings [27].

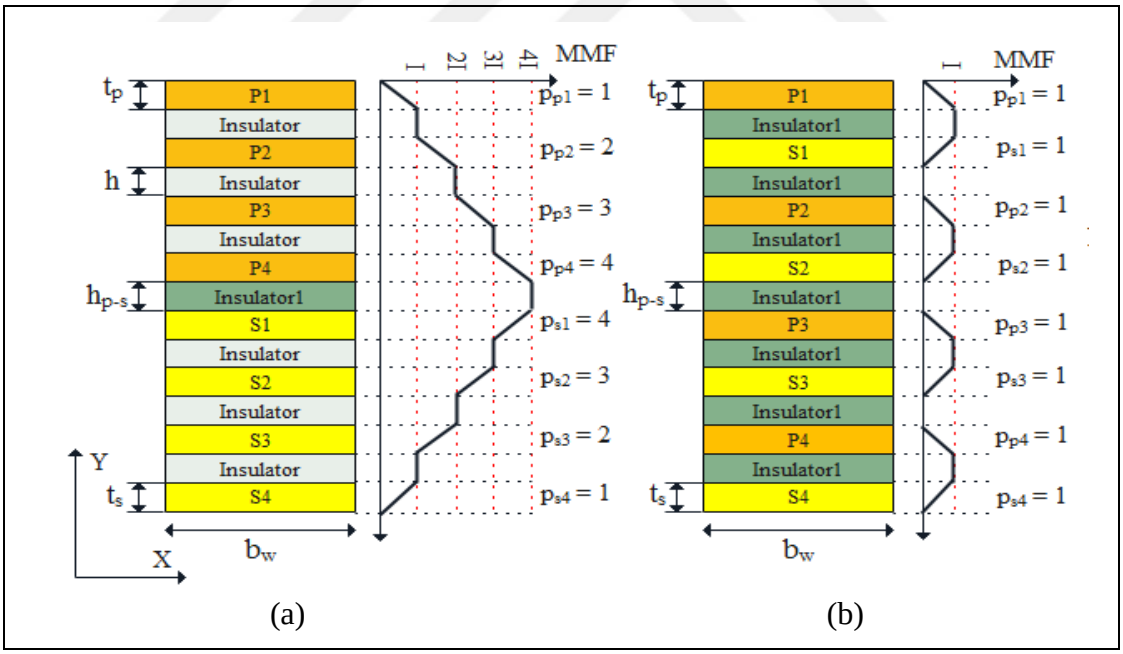


Figure 3.2: MFF distributions (a) Non-interleaving arrangements, (b) Interleaving arrangements.

$F_R$ increases $h$ and $h_{p-s}$ becasue of the leakage flux. Additionally, $F_R$ slightly increases with the width of the layer ($b_w$). All layers can include several turns. The AC resistance of each turn varies based on the distance between the turn and the core,

particularly in non-interleaved arrangements[36]. The most significant factors affecting $F_R$ are $\Delta$ and $p$. As $\Delta$ decreases to a value less than $\delta$, $F_R$ approaches 1, resulting in minimal proximity losses for all $p^{th}$ layers [29]. Figure 3.3 shows that $F_R$ which increases by increasing thickness at a fixed frequency.

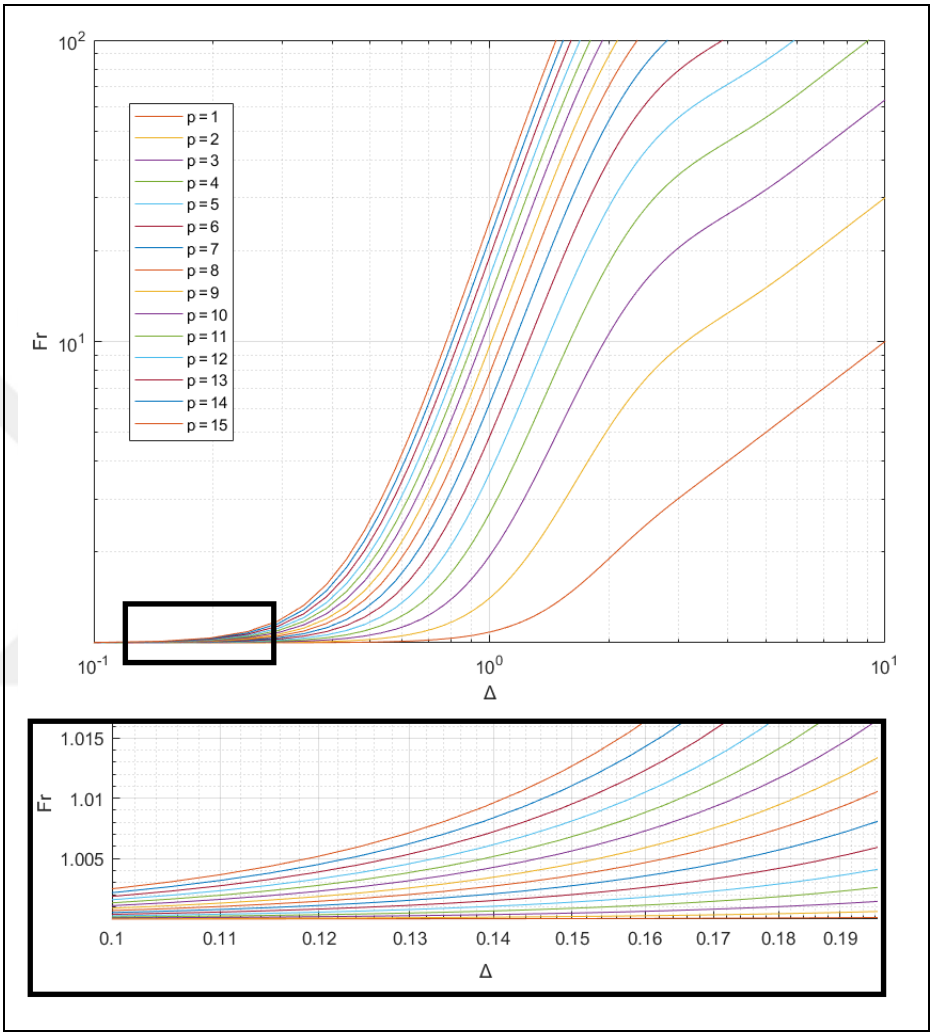


Figure 3.3: The ratio of AC resistance to DC resistance as a function of $\Delta$ and MMF ratio of $p$.

In DC-DC converter applications, transformers are switched to non-sinusoidal current waveforms except for the resonance frequency. $F_R \approx 1{,}3$ is the optimum for $R_{ac}$ [32]. The optimal value for the thickness of the foil conductor ($\Delta_{opt}$) can be calculated by Fourier analysis by considering the RMS value of the converter current ($I_{rms}$), the RMS value of the first derivative of converter current ($I'_{rms}$) and fundamental frequency($f_f$). $I_{rms}$ and $I'_{rms}$ can be calculated by using Fourier analysis where the period is T, and the duty cycle is D. $I_{rms}$ and $I'_{rms}$ calculations are

presented in Table 3.1 [34]. The equation for $\Delta_{opt}$ is given below [34]. $I_0$ is the output current of the converter. $D$ and $T$ are the duty cycle and the converter operation period, respectively. $t_r$ is the current rise time of the converter.

$$\Delta_{opt} = \frac{1}{\sqrt[4]{\frac{5p^2-1}{15}}} \sqrt{\frac{2.\pi.f_f\, I_{rms}}{I'_{rms}}} \tag{3.5}$$

Table 3.1: $I_{rms}$ and $I'_{rms}$ calculations due to waveforms.

| | | |
|---|---|---|
| 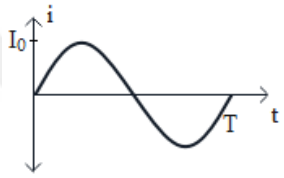 | $I_{rms} = \frac{I_0}{\sqrt{2}}$ | $I'_{rms} = I_0 \frac{2\pi}{T\sqrt{2}}$ |
| 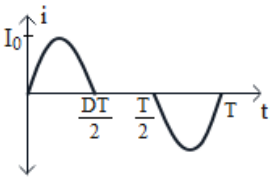 | $I_{rms} = I_0 \sqrt{\frac{D}{2}}$ | $I'_{rms} = I_0 \frac{2\pi}{DT} \sqrt{\frac{D}{2}}$ |
| 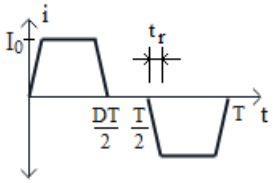 | $I_{rms} = I_0 \sqrt{D - \frac{4t_r}{3T}}$ | $I'_{rms} = I_0 \sqrt{\frac{2}{t_r T}}$ |
| 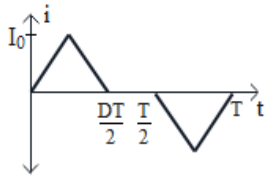 | $I_{rms} = I_0 \sqrt{\frac{D}{3}}$ | $I'_{rms} = \frac{4I_0}{\sqrt{DT}}$ |

In the LLC resonant converter, the gapped core must be used to optimize the value of $L_m$ for the ZVS condition of the main switches as defined in Section 2. The influence of the fringing in the air-gap field will cause $R_{gap}$ to be close to the air gap [31], [33]. $R_{gap}$ can be decreased by winding arrangement [32], [33]. $R_{gap}$ decreases when the distance between the windings and air gap beyond the notch radius is increased. Total winding resistance, $R_{tot}$, can be expressed as the sum of primary

winding resistance ($R_p$) and secondary winding resistance ($R_s$). The equations for $R_{tot}$ are given below.

$$R_s = R_{dc(s)} + R_{ac(s)} + R_{gap(s)} \tag{3.6}$$

$$R_p = R_{dc(p)} + R_{ac(p)} + R_{gap(p)} \tag{3.7}$$

$$R_{tot} = R_p + R_s \tag{3.8}$$

The capacitances are defined as the electric field effects of the transformer. Electric field energy ( $W_E$) can be modeled by the parallel plate method shown in Figure 3.4 where $A_t$, $d$, $V_1$, $V_2$ and $C_{ab}$ are parallel surface area, the distance of conductive plates, voltage level of the conductive plate a, voltage level of the conductive plate b and capacitance between plates, respectively. $\varepsilon_o$ is the permeability of air, and $\varepsilon_r$ is the permeability of the isolation material. The equations for $W_E$ and $C_{ab}$ are given below.

$$W_E = \frac{1}{2}\,(V_1 - V_2)^2 C_{ab} \tag{3.9}$$

$$C_{ab} = \varepsilon_r \varepsilon_o \frac{A_t}{d} \tag{3.10}$$

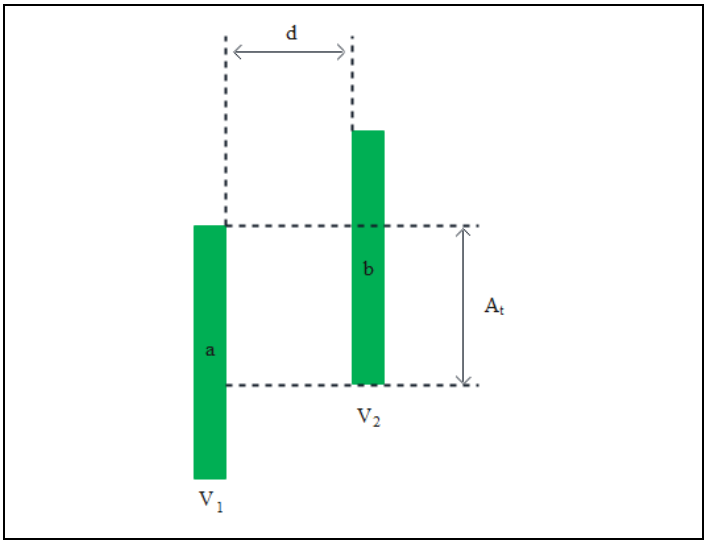


Figure 3.4: The parallel plate capacitance model.

The capacitances of the transformers, $C_p$, $C_s$, and $C_{p-s}$ , have been defined as the primary winding capacitance, secondary winding capacitance, and primary-secondary coupling capacitance, respectively [12]. Unlike the inductive components, capacitive elements cannot be measured directly [13]. The capacitive elements should be measured as much as possible from the magnetic core [11]. The parasitic capacitances of the transformer can be shown as a single equivalent winding capacitance, $C_{tr}$, using the network and step response approach techniques. $C_{tr}$ can be shown on the primary side that can be expressed with scattered or parasitic electrical coupling between windings, where all parameters referred to the primary side are indicated by an apostrophe (‘) [12], [13]. A simplified equivalent model of the primary side is shown in Figure 3.5. The equations for $C_{tr}$ are given below.

$$C_p' = C_p + (1 - N).C_{p-s} \tag{3.11}$$

$$C_s' = N^2 C_s + N.(N - 1).C_{p-s} \tag{3.12}$$

$$C_{tr} \cong C_p' + C_s' \tag{3.13}$$

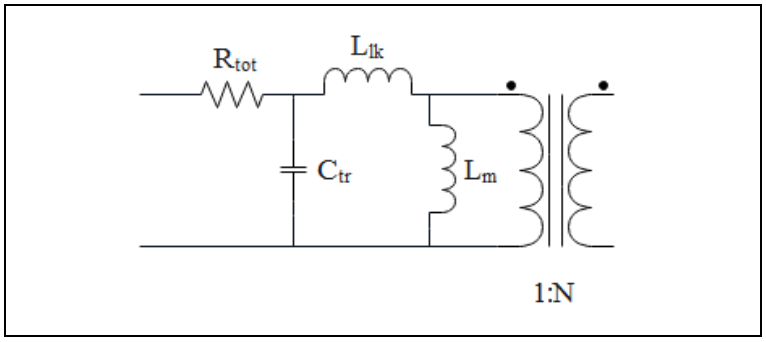


Figure 3.5: The simplified high-frequency transformer model, referred to primary side.

Two resonance frequencies, $f_{series}$ and $f_{paralel}$, are defined as series and parallel resonance frequencies of the transformer, respectively, and given in the following equations. $f_{series}$ is determined by $L_{lk}$ and $C_{tr}$, and $f_{paralel}$ are determined by $(L_m + L_{lk})$ and $C_{tr}$ [11], [20].

$$f_{series} = \frac{1}{2.\pi.\sqrt{L_{lk}.C_{tr}}} \tag{3.14}$$

$$f_{paralel} = \frac{1}{2.\pi.\sqrt{(L_m + L_{lk}).C_{tr}}} \tag{3.15}$$

$C_{P-S}$, which creates a low-impedance path between the primary and secondary windings and gives rise to Electromagnetic interference (EMI) noise, can be reduced by shielding [16] or by increasing $h_{p-s}$ thickness. $C_p$ and $C_s$ can be reduced by increasing the spacing between the windings, reducing the parallel surfaces, increasing the spacing between the layers, and reducing the potential differences between the parallel faces [22], [23]. Making the windings layered is necessary for high-voltage applications for electrical insulation; however, decreasing the turn–turn layer capacitances of windings in the layers reduces the $C_s$ [15], [20]. However, these methods increase the leakage inductance because they also affect magnetic coupling even if the $C_s$ effect is reduced [24]. As the insulator thickness is increased, the equivalent capacitance of the transformer decreases while the leakage inductance increases. Reducing both leakage inductance and transformer equivalent capacitance is not possible because of the physical parameters. However, it is possible to obtain

optimal behaviours for both leakage inductance and stray transformer equivalent capacitance with winding arrangements [26].

In high-voltage applications, the main component of $C_{tr}$ is $C_s$ because $C_s$ must be multiplied by the square of the high turn ratio N. Simply adjusting the winding geometry alone cannot effectively reduce the electric field effects resulting from the high voltage conversion ratio of the transformer.

## 3.2. Integration of Rectifier Network

The modeling should consider the impact of the secondary rectifier network junction capacitance $C_j$. $C_j$ and secondary leakage inductance can create a parasitic resonant network. The parasitic resonant network frequency and converter switching frequency can converge. Thus, the parasitic resonant network frequency and distort voltage and current waveform of the converter [50], [51]. Various types of rectifier networks can be implemented, such as voltage doubler and voltage multipliers. The main configurations of rectifier networks are presented in Figure 3.6.

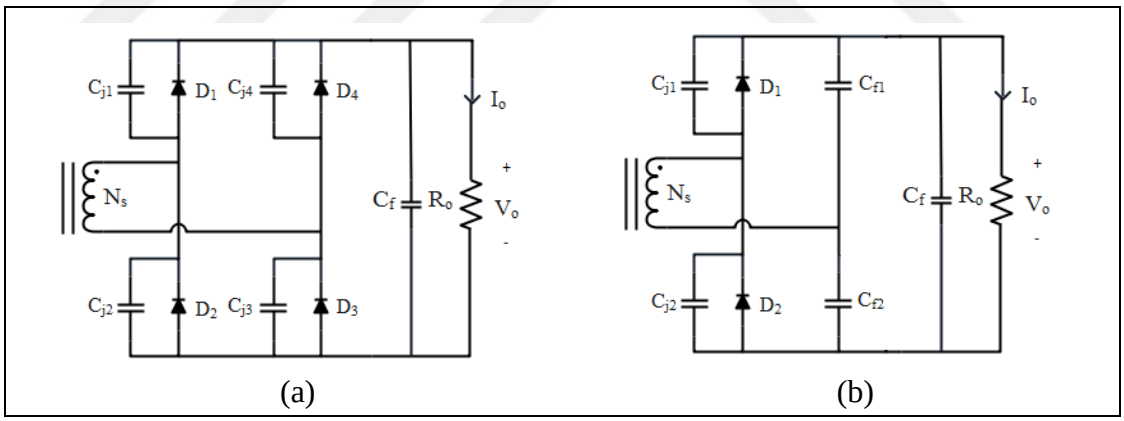


Figure 3.6: The rectifier network types: (a)Full-Bridge, (b) Voltage-Doubler.

$C_j'$ is the impact of the secondary rectifier network junction capacitance referred to as the primary side. $C_j'$ will be half by selecting a voltage-doubler compared to a full-bridge for the same output voltage [51]. Thus, the turn ratio will be half, and the $C_s'$ will also be half. Therefore, a voltage doubler in the high-voltage application is more advantageous than a full bridge to reduce capacitive effects. If the turn ratio is low, $L_m$ is significantly higher than $L_{lks}$, so $C_j$ is parallel to secondary winding capacitance, and its impact will be proximate. The equation for $C_j'$ is given below.

$$C_j' = N^2 . C_j \tag{3.16}$$

$$C_{stray} \cong C_{tr} + C_j' \tag{3.17}$$

In order to define the equivalent stray capacitance referred to the primary side ($C_{stray}$) the effects of $C_j$ must be considered. $C_{stray}$ can be expressed as the sum of $C_{tr}$ and effect $C_j'$ as given below.

$$C_{stray} \cong C_{tr} + C_j' \tag{3.17}$$

## 3.3. Multi-Winding Transformer

A multi-winding transformer includes more than two windings. Each winding can have a different turn ratio and be connected in series or parallel. The power paths can be varied. This section evaluates one primary winding and multi-secondary windings transformer. Winding arrangements such as multi-layer and multi-disk are presented in Figure 3.7 [45], [49].

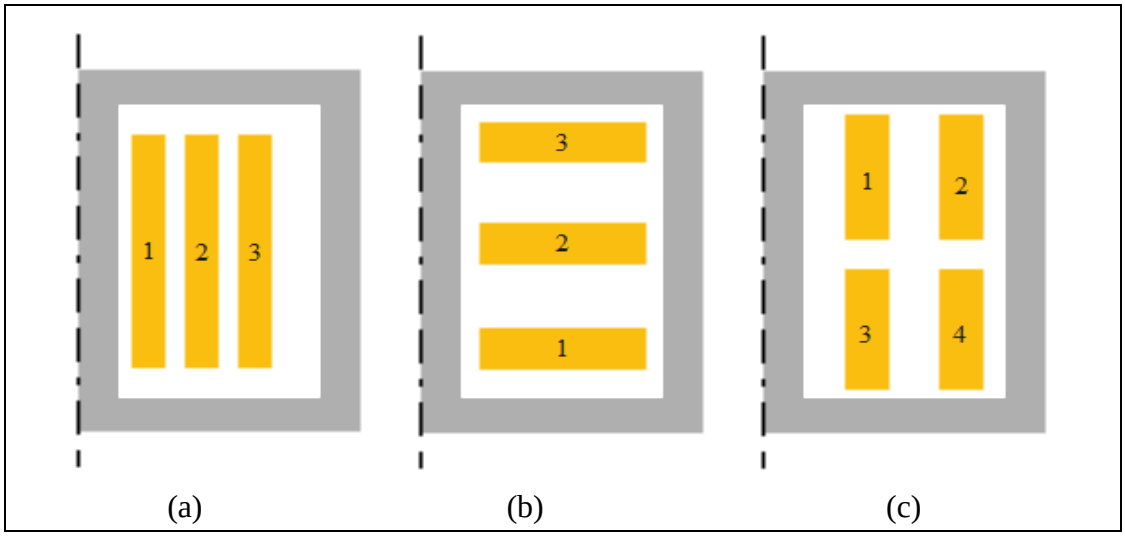


Figure 3.7: The winding arrangements for multi-winding transformer: (a) multi-layer (b) multi-disk (c) mixed.

The multi-winding transformer includes a coupled inductor (leakage transformer) which describes the interaction between leakage (self) inductance for each winding to other windings due to magnetic coupling [41], [49]. The coupled inductor causes power transfer and voltage regulation problems [37]. The multi-winding transformer circuit can be obtained by an inductance matrix. The inductance matrix, L, is a positive defined, symmetrical matrix and includes mutual inductances, coupled inductances and leakage inductance of each winding [38], [44]. The matrix inductances can be measured with short circuit and open circuit tests or load impedance tests [40], [44], [47].

$$L = \begin{vmatrix} L_{11} & M_{1-2} & \dots & M_{1-z} \\ M_{1-2} & L_{22} & \dots & M_{2-z} \\ \vdots & \vdots & \ddots & \vdots \\ M_{1-z} & M_{2-z} & \dots & L_{zz} \end{vmatrix} \tag{3.18}$$

Once the inductance matrix is obtained, the relationship between output current ($i$) and voltage ($v$) can be calculated for each winding as in the following equations [44]. The cross-coupling coefficient, $k$, represents the relationship between each winding to other windings. $R$ is the winding resistance.

$$i = |i_1 \quad i_2 \quad \cdots \quad i_z|^T \tag{3.19}$$

$$v = |v_1 \quad v_2 \quad \cdots \quad v_z|^T \tag{3.20}$$

$$v = Ri + L.\frac{d}{dt}i \tag{3.21}$$

$$k_{i-j} = \frac{M_{i-j}}{\sqrt{L_{ii}.L_{jj}}} \tag{3.22}$$

$$k = \begin{vmatrix} 1 & k_{1-2} & \dots & k_{1-z} \\ k_{1-2} & 1 & \dots & k_{2-z} \\ \vdots & \vdots & \ddots & \vdots \\ k_{1-z} & k_{2-z} & \dots & 1 \end{vmatrix} \quad (3.23)$$

The cross-coupling coefficient describes the relation between mutual and leakage inductance of each winding and must be $0 \leq k \leq 1$. In practice some winding can be dominant coupled (means that $k \approx 1$ ), whereas all others are weak [41]. The differences in the coupling between windings cause unbalance in power transfer and lead to negative inductances [43]. Therefore, the coupled inductor must be modeled separately from mutual inductances for one primary and multi-secondary windings transformer. Since the power path is from the primary to multi-secondary windings, coupling between the primary and each secondary must be convergent, and leakage coupling between secondary windings must be considered. The main obstacle in power transfer is secondary leakage inductance and coupled inductances caused by leakage inductances of each winding. The inductances can be separated by the mutual inductance of the core ($L_{mcore}$), the mutual inductances for each secondary windings ($L_{msi}$), leakage inductances ($L_{Li}$) and coupled inductor inductances ($L_{ci}$) [48]. A multi-winding transformer with an integrated rectifier for one primary winding and a number of z secondary windings is shown in Figure 3.8.

After the inductance matrix is obtained, $L_{mcore}$ can be selected with the minimum mutual inductance between primary and secondary winding as in the following equation.

$$L_{mcore} = \frac{N_p}{N_{si}} M_{1,i} \quad (3.24)$$

Mutual inductance for each secondary winding can be calculated by considering $L_{mcore}$, where $j$ is the number of the secondary winding. Thus, leakage inductance for primary winding can be calculated as given below. $L_{msj}$ is the mutual inductance of the secondary winding j. $L_{lk1}$ is the secondary leakage inductance of which the secondary winding mutual inductance with the primary winding is minimum.

$$\mathrm{L}_{msj} = \left(\frac{N_p}{N_{sj}}\ \mathrm{M}_{1-j}\right) - \mathrm{L}_{mcore} \tag{3.25}$$

$$\mathrm{L}_{lk1} = \mathrm{L}_{11} - \left(\sum_{j=2}^{z} \mathrm{L}_{msj}\right) - \mathrm{L}_{mcore} \tag{3.26}$$

The coupled inductances and leakage inductances for each secondary winding can be obtained by considering mutual inductances, $\mathrm{L}_{mcore}$ and turn ratios. The inductance of the coupled inductor ($L_{leak}$) can be obtained below. $\mathrm{L}_{c(i,j)}$ is the coupled inductance between the secondary winding i and j.

$$\mathrm{L}_{c(i,j)} = \left(\frac{N_{si}}{N_{sj}}\ \mathrm{M}_{i-j}\right) - \mathrm{L}_{mcore} \tag{3.27}$$

$$\mathrm{L}_{lkj} = \mathrm{L}_{jj} - \left(\frac{N_{sj}}{N_p}\right)^2 \mathrm{L}_{mcore} - \sum_{i=2}^{z} \left(\frac{N_{sj}}{N_i}\right)^2 \mathrm{L}_{c(j,i)} \tag{3.28}$$

$$L_{leak} = \begin{vmatrix} L_{lkp} & L_{ms1} & \cdots & L_{c1-z} \\ L_{ms1} & L_{lks1} & \cdots & L_{c2-z} \\ \vdots & \vdots & \ddots & \vdots \\ L_{mz} & L_{c2-z} & \cdots & L_{lksz} \end{vmatrix} \tag{3.29}$$

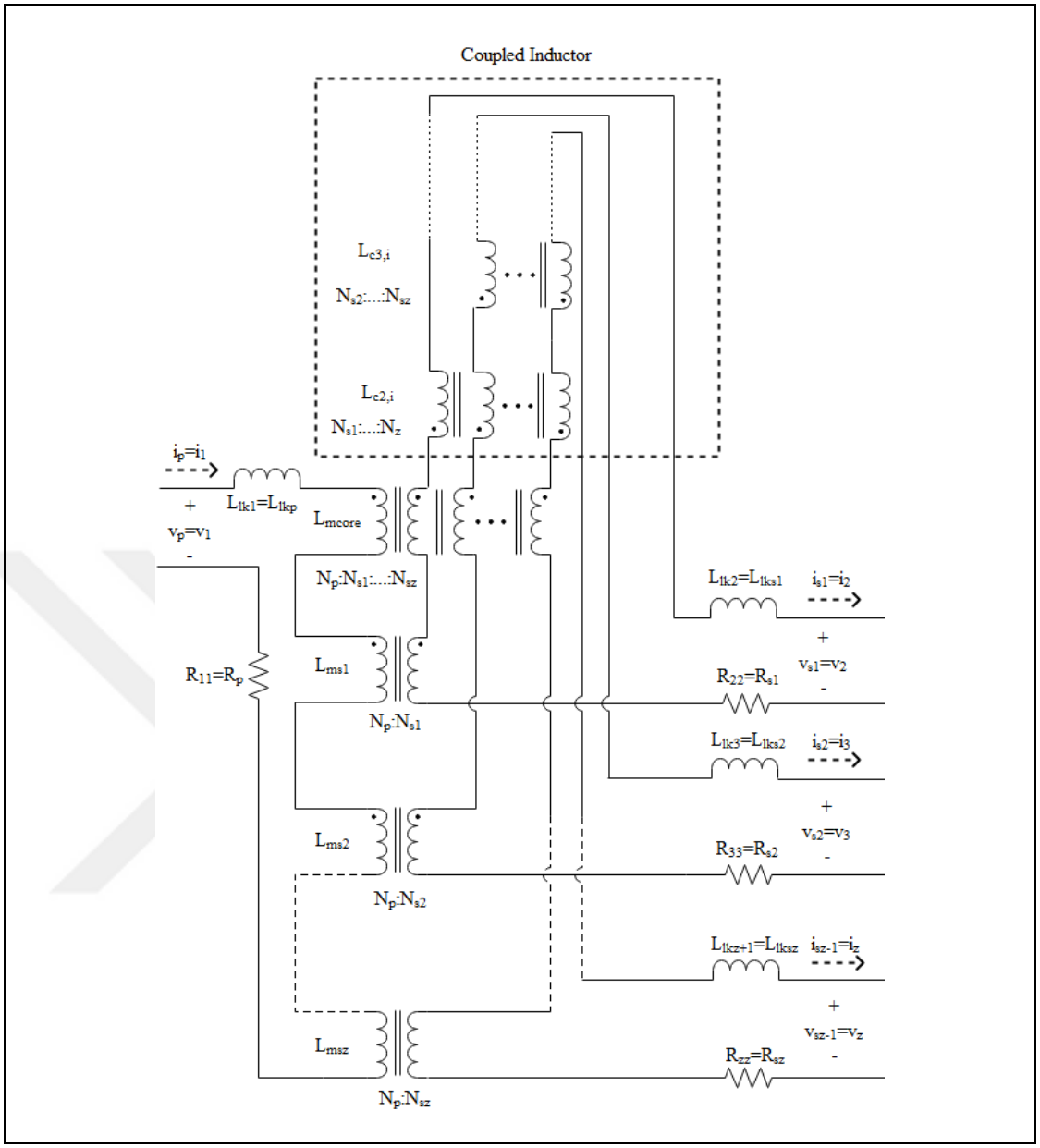


Figure 3.8: The multi-winding transformer model.

Then, equation (3.21) can be converted to equation (3.31) in order to obtain the voltage drop on the coupled inductor in the secondary winding (Δv). The circuit of first secondary winding is presented in Figure 3.9. The cross-coupling between secondary windings must be weak to minimize voltage drop and inaccuracy on secondary windings. Choosing a cross-coupling coefficient k≤0.2 for the coupled inductor results in minimal effects of cross-coupling, and ensures that some serial impedance remains constant regardless of the related winding. This may introduce a maximum inaccuracy of 4% on the serial impedance [41], [44]. Since leakage flux changes depending on the position of each secondary winding, $R_{ac}$ of the windings are

varied. The resistances of each secondary winding can be optimized as defined in section 3.1.

$$\Delta v = |\Delta v_1 \quad \Delta v_2 \quad \cdots \quad \Delta v_z|^T \tag{3.30}$$

$$\Delta v = Ri + L_{leak}\frac{d}{dt}i \tag{3.31}$$

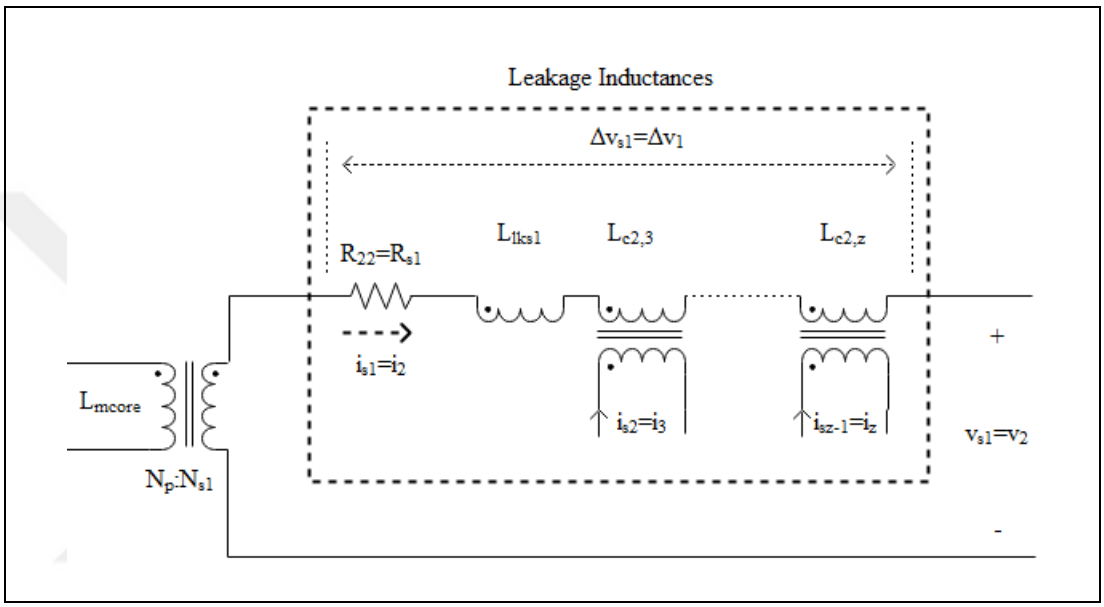


Figure 3.9: The equivalent circuit of the first secondary winding.

The winding capacitances of the multi-winding are $C_{p-s}$, $C_{s-s}$, $C_s$, $C_{Ji}$ are primary-secondary coupling capacitance, secondary-secondary coupling capacitance, secondary winding capacitance and secondary rectifier network junction capacitance, respectively [17]. All capacitances are indicated by the number of windings. The winding capacitances of the multi-winding transformer are presented in Figure 3.10.

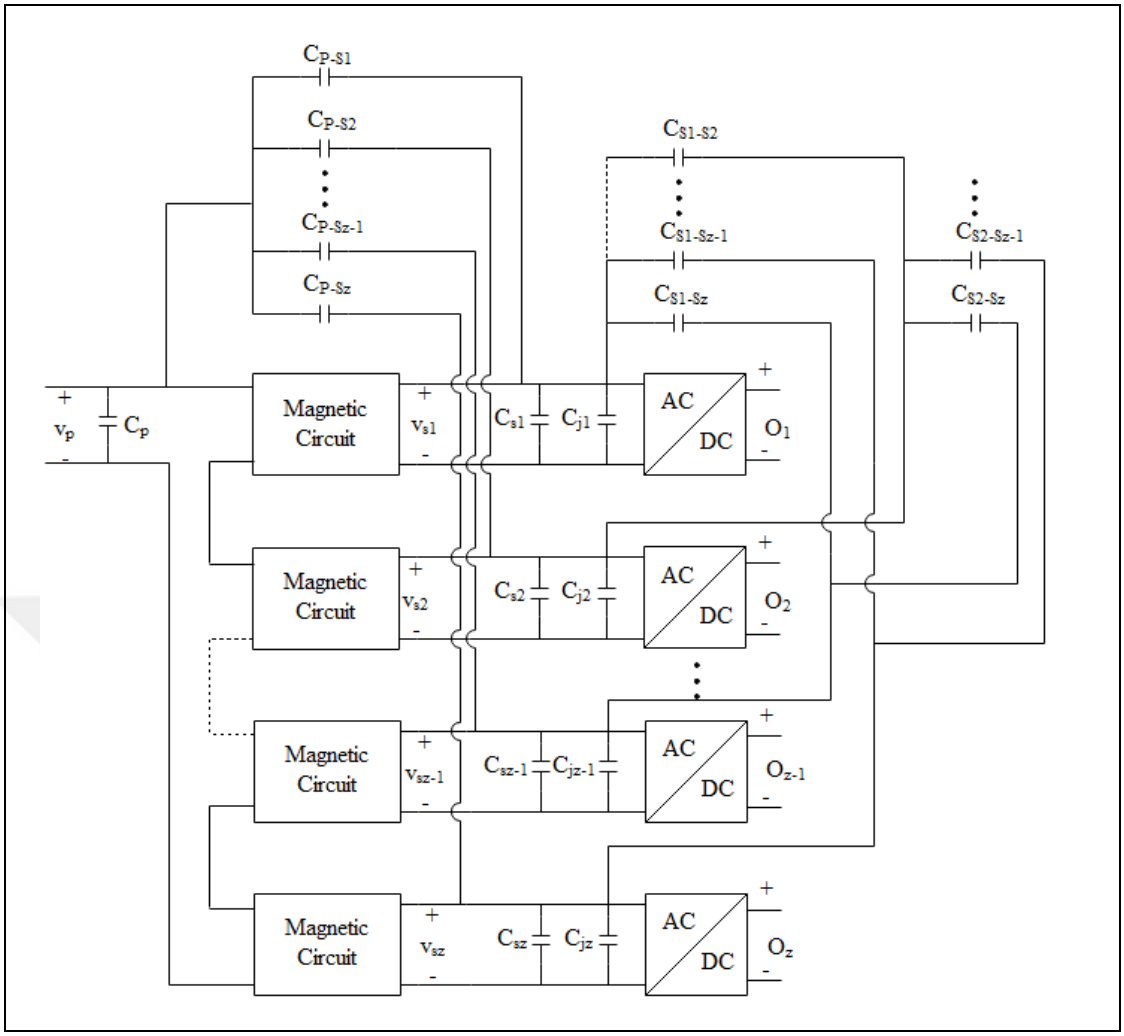


Figure 3.10: The Capacitances of the multi-winding transformer.

For z secondary windings, $C'_{sz}$ and $C'_{pz}$ are defined as the sum of the secondary winding capacitances and the sum of the primary–secondary coupling capacitances, respectively. $C_{tr}$ can be calculated by substituting equations (3.11), (3.12), (3.12) and (3.17), with $C'_{pz}$ and $C'_{sz}$, respectively, resulting in equations (3.33), (3.34) and (3.35) [20], [21]. Calculation of $C_{s-s}$ has another difficulty if the winding voltage distribution is not uniform [17], [18]. The equivalent stray capacitance referred to the primary side must be considered for the LLC resonant converter soft switching condition. $C_{s-s}$ is ineffective for equivalent stray capacitance referred to primary side [20], [21].

$$N_1 = N_{s1}/N_p, \ldots, N_z = N_{sz}/N_p \tag{3.32}$$

$$C'_{pz} = C_p + \sum_{i=1}^{z} (1 - N_i).\, C_{p-si} \tag{3.33}$$

$$C'_{sz} = \sum_{i=1}^{z} N_i^2 C_{si} + N_i^2 C_{ji} + N_i.\,(N_i - 1).\, C_{p-si} \tag{3.34}$$

$$C_{stray} \cong C'_{pz} + C'_{sz} \tag{3.35}$$

## 3.4. Summary

This section has presented a detailed analysis of the high-frequency transformer. The winding losses and capacitive behaviours of the transformer has been described. The parasitic effects of the rectifier network and integration of the rectifier network have also been analyzed. Multi-winding transformer model has been defined based on one primary winding and multi-secondary windings transformer.

# 4. WINDING ARRANGEMENT OF HIGH-VOLTAGE MULTI-WINDING TRANSFORMER WITH INTEGRATED RECTIFIER

In high-voltage applications, the transformer has high values for both the leakage inductance and the stray capacitance. In high-voltage transformers, the key point to examine in the resonant converter topology is optimizing the contradiction between the leakage inductance and the stray capacitance. Both the leakage inductance and the stray capacitance values can be reduced separately. As the leakage inductance decreases, the stray capacitance increases and vice versa. The leakage inductance cannot be reduced because of the isolation requirement of high-voltage transformers. The stray capacitance can not be reduced for high-voltage transformers since they have a high turn ratio by only winding arrangement.

The main objective of the proposed winding arrangement is decreasing stray capacitance and minimizing that arrangement's influence on the leakage inductance and winding losses by considering cross-coupling effects. Since stray capacitance decreases to negligible values, distortion of the current and voltage waveforms on the primary side decreases and the converter's gain increases as defined in Section 2. Thus, the LLC resonant converters can be suitable to use in high-voltage applications.

This section presents a winding arrangement that decreases the stray capacitance of the transformer by using a multi-winding transformer to make the LLC resonant converter usable in high-voltage applications. The concept of winding arrangement and FEA analysis are introduced.

## 4.1. Design Concept

The proposed winding arrangement is presented in Figure 4.1. The winding direction of the primary coil is along the y-axis, and the winding direction of the secondary coil is along the x-axis. All secondary windings are designed with the same geometry, turn ratio, and a single layer on a PCB.

If all the secondary windings are connected in series before the rectifier network, it is multi-layer (sectional) winding. In multi-layer arrangements, stray capacitance is extremely high, which is not suitable for the LLC resonant converter applications.

Leakage inductance and winding losses can be calculated as defined in Section 3. If all secondary windings are connected in series after the rectifier network, it is a multi-winding transformer. Since coupling relationships between the windings are complex, a more complex analysis is required.

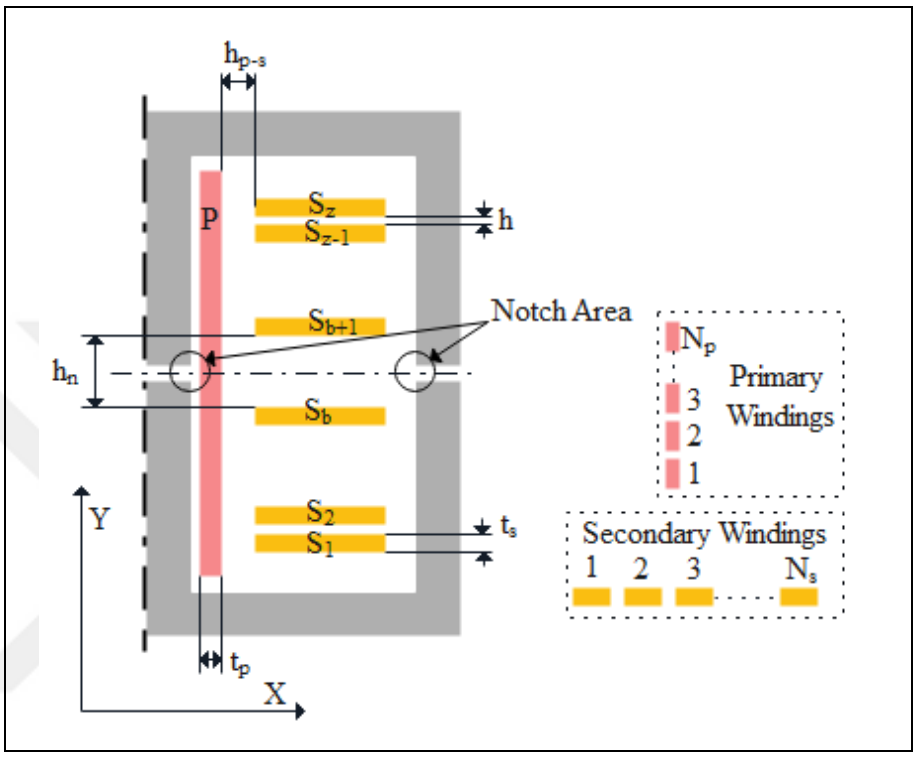


Figure 4.1: Proposed winding arrangement.

Since the secondary windings are connected in series after the rectifier network, the DC current to load is the same for all windings. However, the secondary winding voltage can vary due to the impedance of leakage inductance and coupled inductor. By assuming the coupling effect is similar for all the secondary windings, the capacitive effects of the multi-winding transformer integrated with a rectifier are presented in Figure 4.2.

The voltage level of $Layer\ (i)$ is $U_o$, and the voltage level of $Layer\ (i+1)$ is $U_o + U_p$, and both are the DC voltages. Each layer includes an AC voltage $U_p$. Thus, the storage energy of the electrical field has two components which are $C_{ac}$ and $C_{dc}$ and can be separated by using an integrated rectifier [24]. $C_{dc}$, unlike $C_{ac}$, is not charged and discharged during one period of the switching frequency. Therefore, the effects of $C_{dc}$ on the resonant converter are limited. $C_{ac}$ and $C_{dc}$ can be separated by multi-winding transformers where the output of the rectifier network are serially

connected; however, voltage distribution of the output, winding arrangement and effects of the multi-winding transformer to resonant converter must be evaluated.

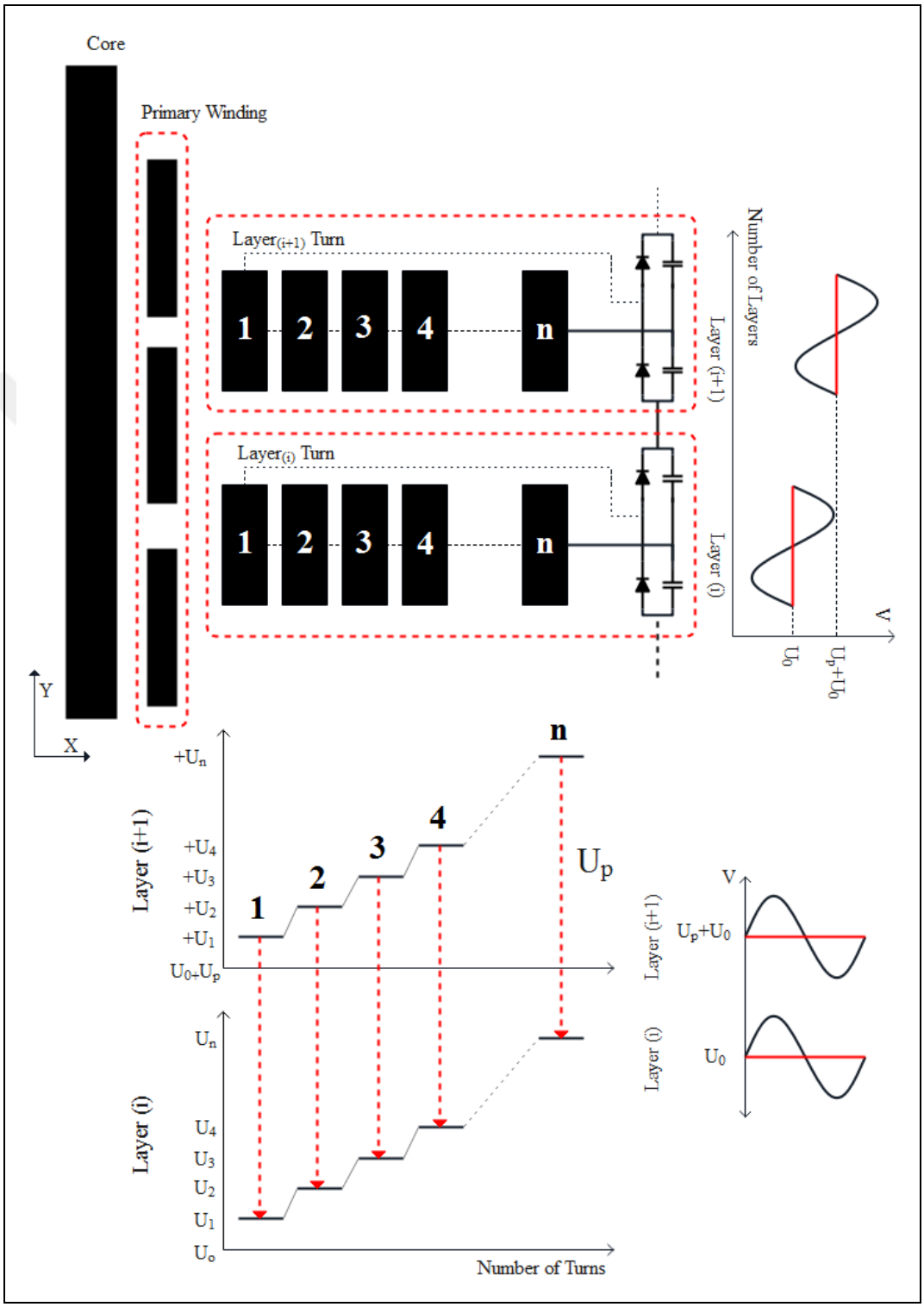


Figure 4.2: The capacitive effects of the proposed transformer.

In the secondary windings, each layer includes N turns and is designed with the same geometry with symmetry. Since the secondary layers are along the x-axis, each secondary layer is symmetric on the y-axis. This implies that the distance between the symmetric turn and the core is consistent within the layers. Also, the distance between the symmetric turn and the primary winding is consistent within the layers. Stated differently, the distance between the second turn of $Layer\ (i)$ and the core is equal to the distance between the second turn of $Layer\ (i+1)$ and the core. Similarly, the distance between the second turn of $Layer\ (i)$ and the primary winding and the distance between the second turn of $Layer\ (i+1)$ and the primary winding are equal. This symmetry is the same for all secondary layers. Within each layer, the symmetric turn resistance becomes convergent due to the combined effects of MLT and the proximity effects. The layer resistance is calculated as the total of the turn resistances within a layer. Thus, the proximity effect to resistance for layers is convergent. The resistance of each layer is related to its location on the y-axis. Thus, the number of layers has a limited effect on total winding resistance. The AC resistance for each secondary winding depends on leakage inductance. By selecting the thickness of foil as presented in Section 3, the proximity effects on each winding will be minimized. The resistance of the primary winding effect is limited. In high-voltage transformers, the secondary windings current are very low compared to the primary winding. Thus, $\Delta$ can be selected less than $\Delta_{opt}$, so secondary winding resistance proximity losses are limited.

If the coupling effect is convergent and less than 0.2 for all the secondary windings, it can be said that;

- All secondary windings are rectified, and all layers are designed in the same geometry, $C_{s-s}$ in all windings has only $C_{dc}$, and the influence of the converter is negligible. There can be low-impedance differences between the secondary windings because of differences. Since $C_{dc}$ is much higher than $C_{ac}$, $C_{s-s}$ effect will be limited. The distance between secondary windings $h$ and $h_n$ causes only an increase of leakage inductance and has a limited effect on $C_{s-s}$. Since the minimum distance between the secondary windings to the notch area is $h_n/2$, $R_{gap}$ is minimized.

- Each secondary layer has the DC voltage level, and the DC voltage level increases with the number of layers. Each layer includes an AC voltage $U_p$. For each layer, $C_{P-S}$ includes a high $C_{dc}$ component that is negligible compared to the small $C_{ac}$ component. As the AC voltage level $U_p$ is equal for each secondary winding, $C_{ac}$ remains the same for each of them. Thus each layer $C_{P-S}$ value is convegent.
- Since the secondary windings are designed in the same geometry, $C_s$ is the same for all the secondary windings.
- $C_{P-S}$ and $C_s$ are convergent in all secondary layers. In this case, from equation (3.33) and (3.34) $C_{stray}$ can be expressed as a linear function of the output number z.
- The optimization of leakage inductance and winding losses can be achieved by arranging tickness of $h$ and $h_n$ accordingly.

Optimization is needed to determine the appropriate values for the secondary winding number N and the number of secondary windings z to minimize $C_{stray}$. Increasing N in each layer increases $C_s$ because of the turn-to-turn capacitance. $C_s$ includes only $C_{ac}$. The $C_{stray}$ increase is multiplied by the square of N. Increasing z because of the separation of $C_{ac}$, $C_{dc}$, and $C_{stray}$ increases proportionally $C_{stray}$, which will be significantly reduced.

## 4.2. FEA Simulation

FEA software Maxwell is used for proposed winding simulations. Simulations have been carried out using the transient solver for core losses and flux density. Eddy current solver is used for leakage inductance, mutual inductance and coupling coefficient matrix. For the capacitance simulations, the electrostatic solver has been used. The design parameters of the multi-winding transformer are presented in Table 4.1. The three-dimensional model of the multi-winding transformer is shown in Figure 4.3.

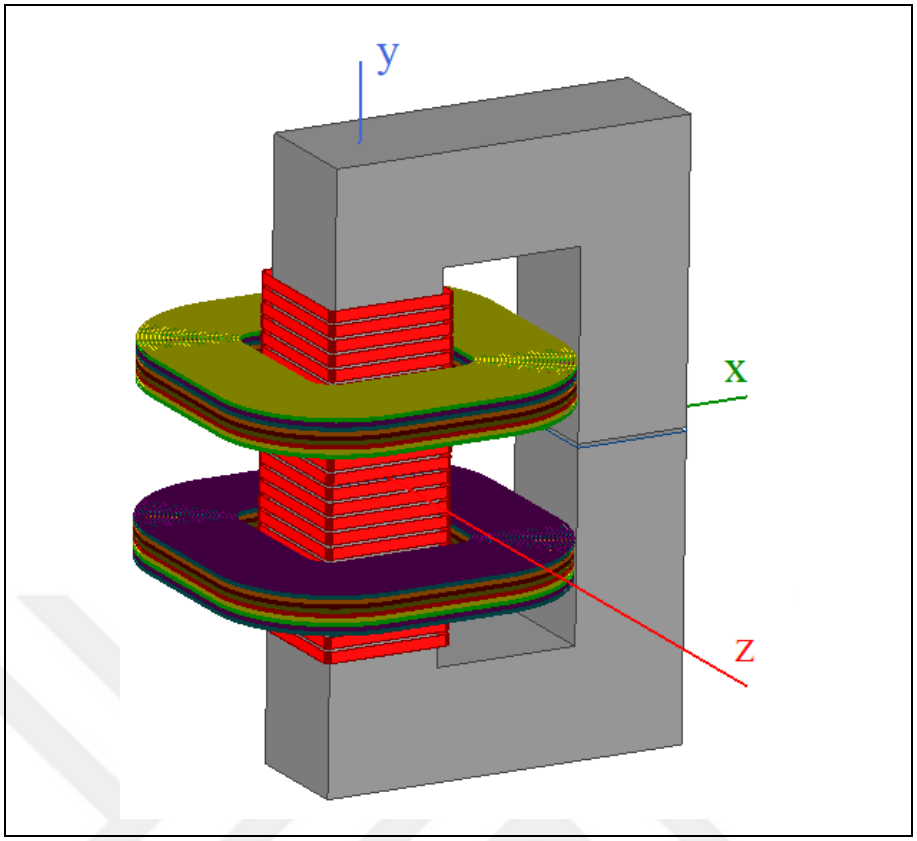


Figure 4.3:Three dimension model of multi-winding transformer.

Table 4.1:Simulation design parameters.

| | |
|---|---|
| **Core material** | Ferroxcube 3F3 |
| **Core Type** | UU93 |
| $\mathbf{N}_{p}$ | 24 Turns |
| $\mathbf{N}_{S-Layer}$ | 24 Turns |
| $\mathbf{Z}_{S-Layer}$ | 20 Layer |
| $h_n$ | 5 mm |
| $h_s$ | 1 mm |
| $h_{p-s}$ | 5 mm |
| **Air gap** | 1 mm |
| $t_p$ | 0.1 mm |
| $w_p$ | 3 mm |
| $t_s$ | 0.035 mm |
| $w_s$ | 0.3 mm |

Simulation waveforms are selected the same as in Section 2.2 where $Q = 1$ and operation frequency is selected just below resonant frequency, 68 kHz, to analyze the worst condition. The current waveforms are presented in Figure 4.4.

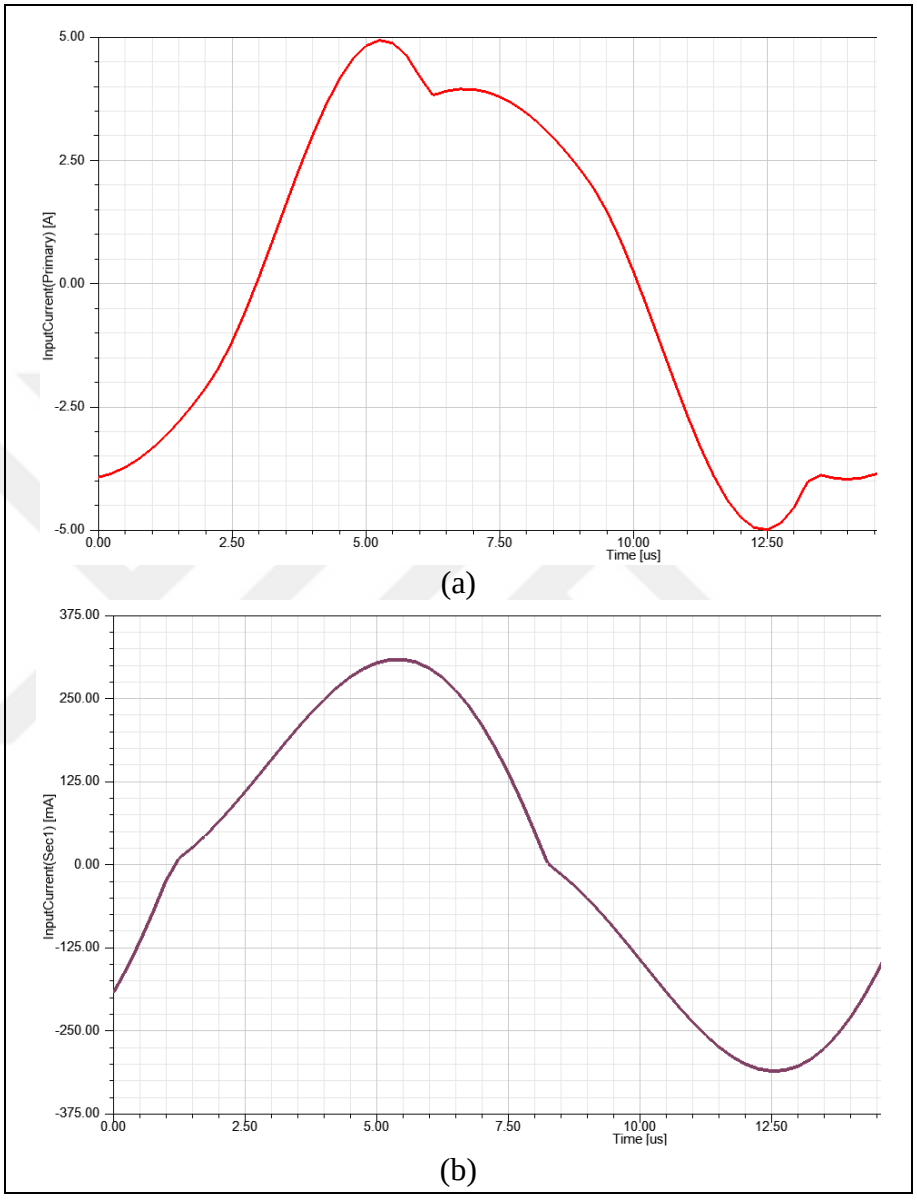


Figure 4.4: Simulation current waveforms: (a) Primary current (b) Each secondary current.

The mesh dimensions are 4 mm for the core and 0.002 mm for the conductors. The mesh plot is shown in Figure 4.5.

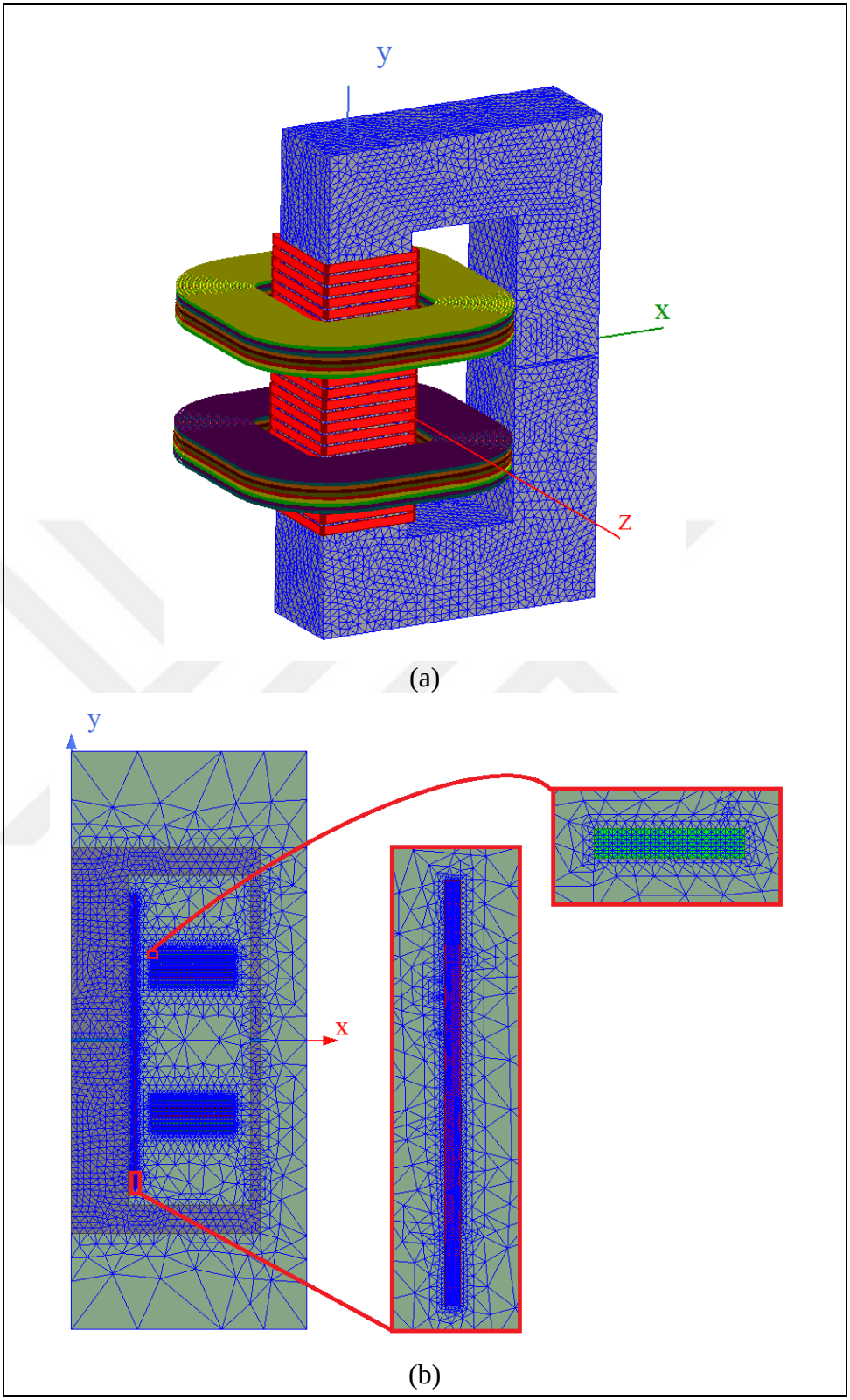


Figure 4.5: Mesh Plot: (a) 3D core, (b) 2D conductor.

Simulation results for current density are presented in Figure 4.6. In the primary winding, current density increases near the airgap because of the notch effect. The current density in the secondary windings is convergent.

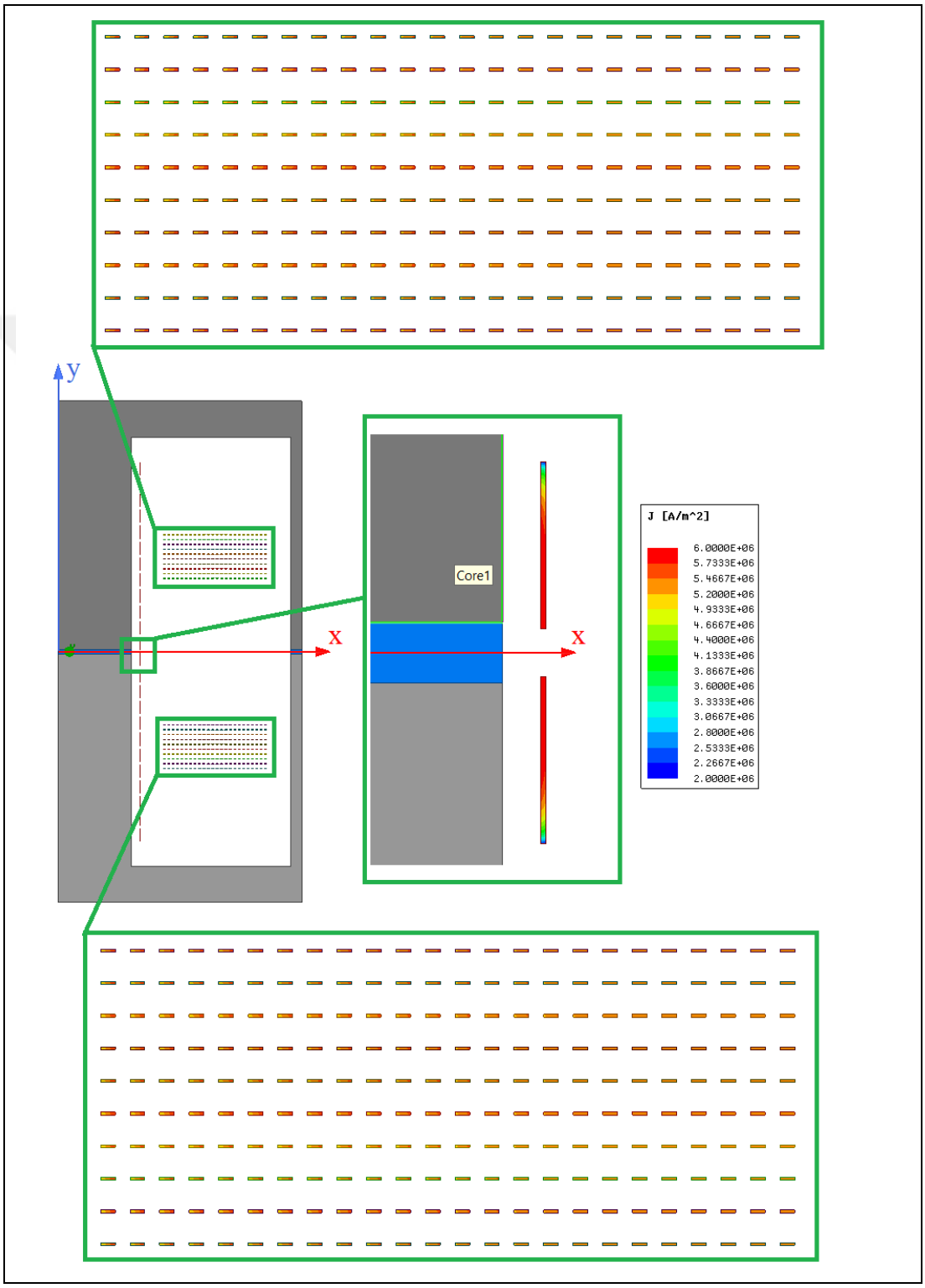


Figure 4.6: Simulation results for current density.

Simulation results for flux density and magnetic flux distribution are presented in Figure 4.7.

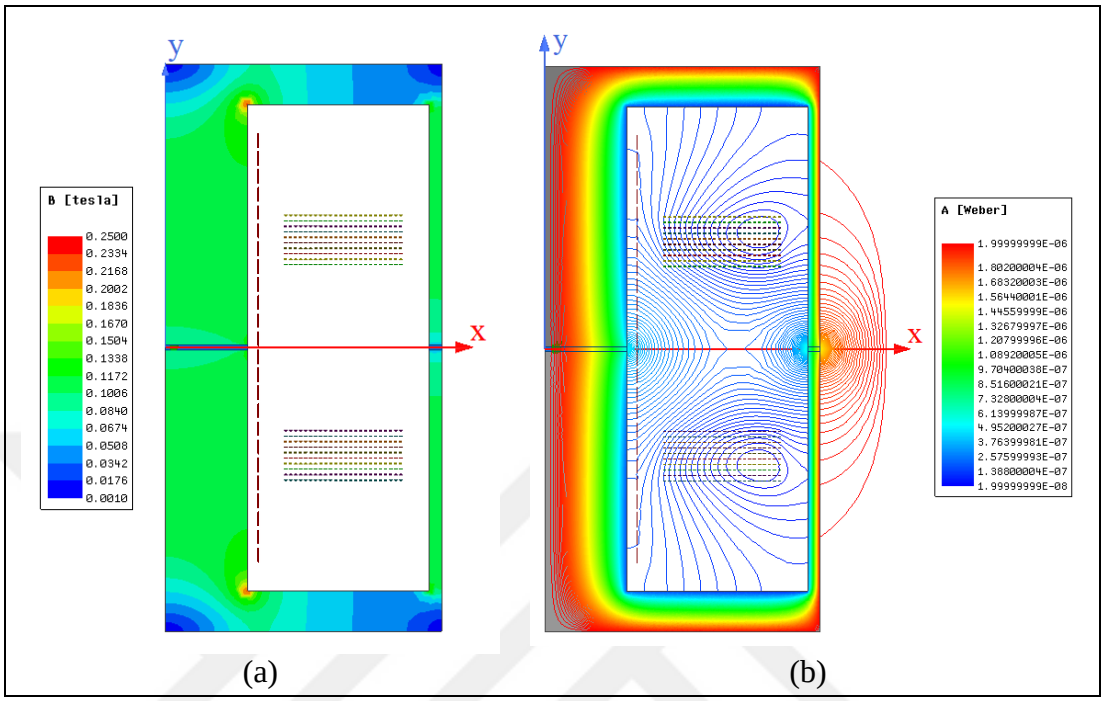


Figure 4.7: Simulation results: (a) Flux density, (b) Magnetic flux distribution.

The resistance simulation results at different frequencies are presented in Table 4.2. The comparison of winding resistance simulation results at different frequencies is shown in Figure 4.8. Since the winding geometry is the same, the DC resistance of all the secondary windings is convergent. The resistance of each winding is determined by its location on the y-axis, distance to the air gap, and distance to the edge of the core.

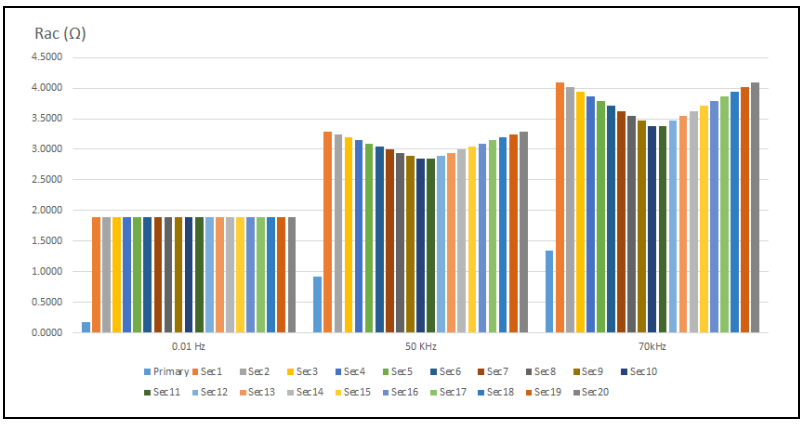


Figure 4.8: Simulation results for winding resistance.

Table 4.2: The simulation results for the winding resistance.

| | **0.01 Hz** | **50 KHz** | **70kHz** | **100 kHz** | **200 kHz** | **500 kHz** | **1000 kHz** |
|---|---|---|---|---|---|---|---|
| $\boldsymbol{R_p}$ | 0.1719 | 0.9182 | 1.3393 | 1.9199 | 3.7603 | 11.8950 | 37.7300 |
| $\boldsymbol{R_{s1}}$ | 1.8921 | 3.2894 | 4.0899 | 5.1690 | 8.1830 | 18.6830 | 48.1330 |
| $\boldsymbol{R_{s2}}$ | 1.8923 | 3.2424 | 4.0160 | 5.0614 | 8.0083 | 18.3980 | 47.5640 |
| $\boldsymbol{R_{s3}}$ | 1.8921 | 3.1941 | 3.9402 | 4.9503 | 7.8223 | 18.0720 | 46.9180 |
| $\boldsymbol{R_{s4}}$ | 1.8919 | 3.1452 | 3.8631 | 4.8368 | 7.6281 | 17.7150 | 46.2120 |
| $\boldsymbol{R_{s5}}$ | 1.8921 | 3.0962 | 3.7855 | 4.7218 | 7.4274 | 17.3330 | 45.4560 |
| $\boldsymbol{R_{s6}}$ | 1.8921 | 3.0466 | 3.7069 | 4.6050 | 7.2203 | 16.9260 | 44.6520 |
| $\boldsymbol{R_{s7}}$ | 1.8919 | 2.9964 | 3.6272 | 4.4864 | 7.0070 | 16.4960 | 43.7980 |
| $\boldsymbol{R_{s8}}$ | 1.8921 | 2.9461 | 3.5472 | 4.3666 | 6.7875 | 16.0390 | 42.8910 |
| $\boldsymbol{R_{s9}}$ | 1.8923 | 2.8954 | 3.4662 | 4.2448 | 6.5602 | 15.5500 | 41.9160 |
| $\boldsymbol{R_{s10}}$ | 1.8921 | 2.8436 | 3.3836 | 4.1199 | 6.3219 | 15.0160 | 40.8520 |
| $\boldsymbol{R_{s11}}$ | 1.8921 | 2.8436 | 3.3836 | 4.1200 | 6.3220 | 15.0170 | 40.8520 |
| $\boldsymbol{R_{s12}}$ | 1.8923 | 2.8954 | 3.4662 | 4.2448 | 6.5602 | 15.5500 | 41.9170 |
| $\boldsymbol{R_{s13}}$ | 1.8921 | 2.9461 | 3.5472 | 4.3666 | 6.7876 | 16.0390 | 42.8910 |
| $\boldsymbol{R_{s14}}$ | 1.8919 | 2.9964 | 3.6273 | 4.4865 | 7.0071 | 16.4960 | 43.7990 |
| $\boldsymbol{R_{s15}}$ | 1.8921 | 3.0466 | 3.7069 | 4.6051 | 7.2204 | 16.9260 | 44.6520 |
| $\boldsymbol{R_{s16}}$ | 1.8921 | 3.0963 | 3.7855 | 4.7219 | 7.4274 | 17.3330 | 45.4560 |
| $\boldsymbol{R_{s17}}$ | 1.8919 | 3.1453 | 3.8631 | 4.8368 | 7.6281 | 17.7150 | 46.2130 |
| $\boldsymbol{R_{s18}}$ | 1.8921 | 3.1941 | 3.9402 | 4.9503 | 7.8224 | 18.0720 | 46.9180 |
| $\boldsymbol{R_{s19}}$ | 1.8923 | 3.2424 | 4.0161 | 5.0615 | 8.0084 | 18.3980 | 47.5650 |
| $\boldsymbol{R_{s20}}$ | 1.8921 | 3.2894 | 4.0899 | 5.1691 | 8.1831 | 18.6830 | 48.1330 |

The leakage inductances are calculated as presented in Section 3.3. The inductance matrix and coupling coefficient matrix are shown in Figure 4.9 and Figure 4.10, respectively. The coupling coefficient of the leakage transformer is very weak without adjacent layers. The secondary winding voltage distribution is convergent.

$$
L_{lk} = \begin{bmatrix}
72.67 & 7.87 & 7.16 & 6.40 & 5.60 & 4.77 & 3.89 & 2.97 & 2.01 & 1.02 & 0.85 & 0.78 & 1.02 & 2.01 & 2.97 & 3.89 & 4.77 & 5.61 & 6.40 & 7.16 & 7.87 \\
7.87 & 63.42 & 8.07 & 7.56 & 7.07 & 6.60 & 6.14 & 5.69 & 5.25 & 4.82 & 4.39 & 1.99 & 2.01 & 2.03 & 2.05 & 2.06 & 2.08 & 2.09 & 2.10 & 2.12 & 2.13 \\
7.16 & 8.07 & 34.38 & 7.69 & 7.18 & 6.69 & 6.22 & 5.76 & 5.31 & 4.87 & 4.44 & 1.97 & 1.99 & 2.01 & 2.03 & 2.05 & 2.06 & 2.08 & 2.09 & 2.11 & 2.12 \\
6.40 & 7.56 & 7.69 & 38.02 & 7.31 & 6.80 & 6.31 & 5.84 & 5.38 & 4.94 & 4.50 & 1.96 & 1.98 & 2.00 & 2.02 & 2.04 & 2.05 & 2.07 & 2.08 & 2.09 & 2.10 \\
5.60 & 7.07 & 7.18 & 7.31 & 23.31 & 6.93 & 6.42 & 5.94 & 5.47 & 5.01 & 4.57 & 1.95 & 1.97 & 1.99 & 2.01 & 2.02 & 2.04 & 2.05 & 2.07 & 2.08 & 2.09 \\
4.77 & 6.60 & 6.69 & 6.80 & 6.93 & 19.97 & 6.55 & 6.05 & 5.56 & 5.09 & 4.64 & 1.93 & 1.95 & 1.97 & 1.99 & 2.01 & 2.02 & 2.04 & 2.05 & 2.06 & 2.08 \\
3.89 & 6.14 & 6.22 & 6.31 & 6.42 & 6.55 & 29.89 & 6.18 & 5.67 & 5.19 & 4.72 & 1.91 & 1.94 & 1.96 & 1.97 & 1.99 & 2.01 & 2.02 & 2.04 & 2.05 & 2.06 \\
2.97 & 5.69 & 5.76 & 5.84 & 5.94 & 6.05 & 6.18 & 45.27 & 5.81 & 5.30 & 4.82 & 1.90 & 1.92 & 1.94 & 1.96 & 1.97 & 1.99 & 2.01 & 2.02 & 2.03 & 2.05 \\
2.01 & 5.25 & 5.31 & 5.38 & 5.47 & 5.56 & 5.67 & 5.81 & 59.61 & 5.44 & 4.94 & 1.88 & 1.90 & 1.92 & 1.94 & 1.96 & 1.97 & 1.99 & 2.00 & 2.01 & 2.03 \\
1.02 & 4.82 & 4.87 & 4.94 & 5.01 & 5.09 & 5.19 & 5.30 & 5.44 & 72.96 & 5.07 & 1.86 & 1.88 & 1.90 & 1.92 & 1.94 & 1.95 & 1.97 & 1.98 & 1.99 & 2.01 \\
0.85 & 4.39 & 4.44 & 4.50 & 4.57 & 4.64 & 4.72 & 4.82 & 4.94 & 5.07 & 85.35 & 1.83 & 1.86 & 1.88 & 1.90 & 1.92 & 1.93 & 1.95 & 1.96 & 1.97 & 1.99 \\
0.78 & 1.99 & 1.97 & 1.96 & 1.95 & 1.93 & 1.91 & 1.90 & 1.88 & 1.86 & 1.83 & 74.58 & 5.07 & 4.94 & 4.82 & 4.72 & 4.64 & 4.57 & 4.50 & 4.45 & 4.40 \\
1.02 & 2.01 & 1.99 & 1.98 & 1.97 & 1.95 & 1.94 & 1.92 & 1.90 & 1.88 & 1.86 & 5.07 & 61.21 & 5.44 & 5.30 & 5.19 & 5.09 & 5.01 & 4.94 & 4.87 & 4.82 \\
2.01 & 2.03 & 2.01 & 2.00 & 1.99 & 1.97 & 1.96 & 1.94 & 1.92 & 1.90 & 1.88 & 4.94 & 5.44 & 46.86 & 5.81 & 5.67 & 5.56 & 5.47 & 1.99 & 5.31 & 4.82 \\
2.97 & 2.05 & 2.03 & 2.02 & 2.01 & 1.99 & 1.97 & 1.96 & 1.94 & 1.92 & 1.90 & 4.82 & 5.30 & 5.81 & 31.45 & 6.18 & 6.05 & 5.94 & 5.84 & 5.76 & 5.69 \\
3.89 & 2.06 & 2.05 & 2.04 & 2.02 & 2.01 & 1.99 & 1.97 & 1.96 & 1.94 & 1.91 & 4.72 & 5.19 & 5.67 & 6.18 & 14.95 & 6.56 & 6.42 & 6.31 & 6.22 & 6.14 \\
4.77 & 2.08 & 2.06 & 2.05 & 2.04 & 2.02 & 2.01 & 1.99 & 1.97 & 1.95 & 1.93 & 4.64 & 5.09 & 5.56 & 6.05 & 6.56 & 27.09 & 6.93 & 6.80 & 6.69 & 6.60 \\
5.61 & 2.09 & 2.08 & 2.07 & 2.05 & 2.04 & 2.02 & 2.01 & 1.99 & 1.97 & 1.95 & 4.57 & 5.01 & 5.47 & 5.94 & 6.42 & 6.93 & 21.64 & 7.31 & 7.18 & 7.07 \\
6.40 & 2.10 & 2.09 & 2.08 & 2.07 & 2.05 & 2.04 & 2.02 & 2.00 & 1.98 & 1.96 & 4.50 & 4.94 & 1.99 & 5.84 & 6.31 & 6.80 & 7.31 & 41.94 & 7.69 & 7.56 \\
7.16 & 2.12 & 2.11 & 2.09 & 2.08 & 2.06 & 2.05 & 2.03 & 2.01 & 1.99 & 1.97 & 4.45 & 4.87 & 5.31 & 5.76 & 6.22 & 6.69 & 7.18 & 7.69 & 63.80 & 8.07 \\
7.87 & 2.13 & 2.12 & 2.10 & 2.09 & 2.08 & 2.06 & 2.05 & 2.03 & 2.01 & 1.99 & 4.40 & 4.82 & 4.82 & 5.69 & 6.14 & 6.60 & 7.07 & 7.56 & 8.07 & 50.74
\end{bmatrix} \mu H
$$

Figure 4.9: The leakage inductance matrix.

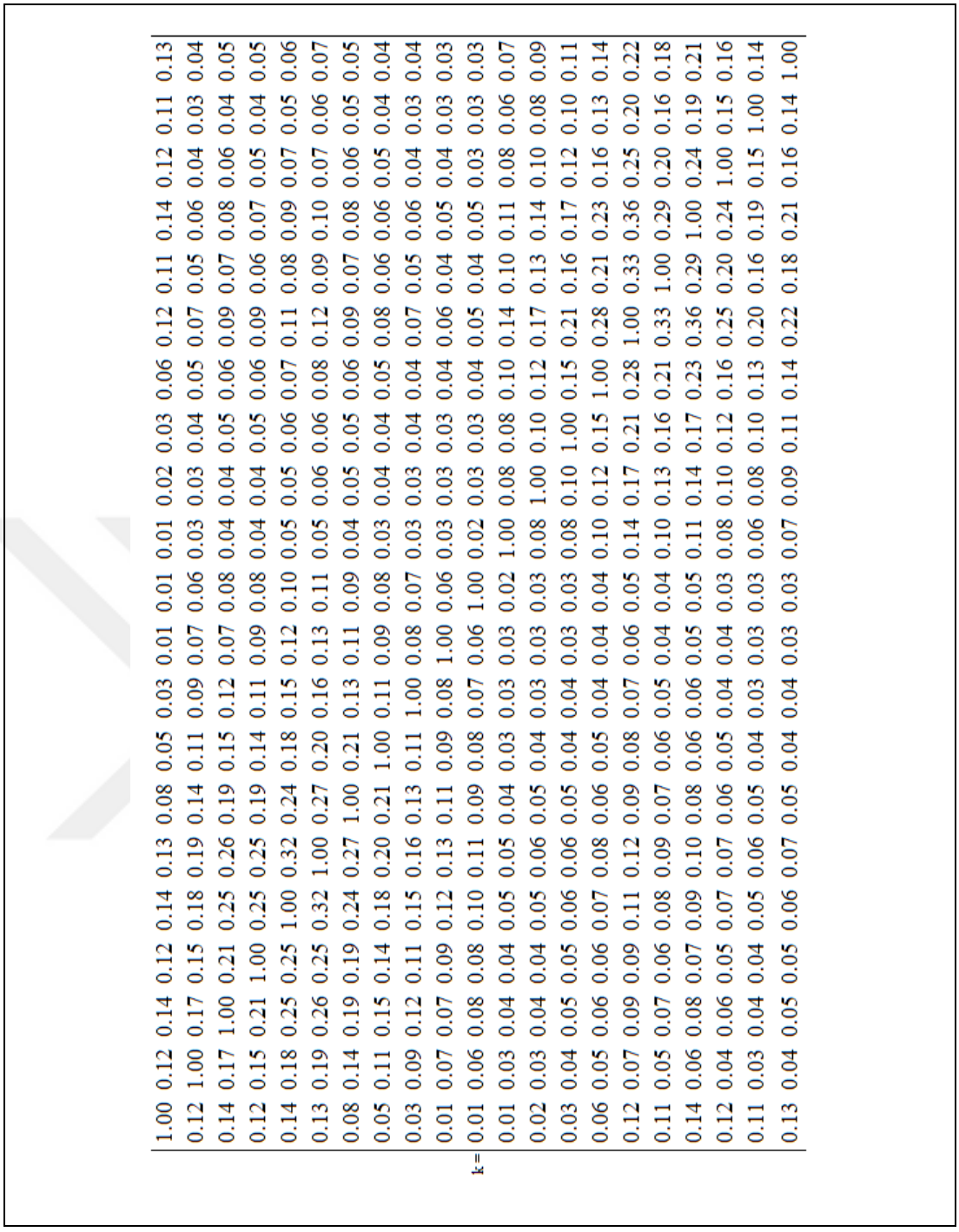


Figure 4.10: The leakage inductance coupling coefficient matrix.

The value the leakage inductance for each winding is presented in Figure 4.11. As shown in Figure 4.8, some winding resistances are decreased due to their position on the y-axis, and for the same windings, leakage inductances are increased. From the equations (3.29), (3.30), (3.31), the voltages of the leakage transformer are convergent. Thus, the voltage distribution of the secondary windings is convergent.

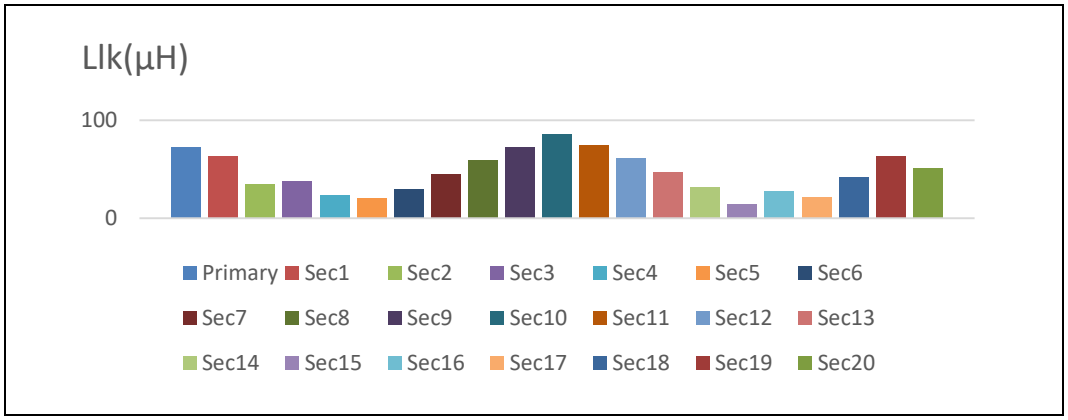


Figure 4.11: Simulation results for leakage inductance.

The electrostatic simulation results for winding capacitances and primary-secondary coupling capacitance are presented in Table 4.3. The comparison of winding capacitances and primary-secondary coupling capacitance is shown in Figure 4.12. The electrostatic solver of the FEA program uses the parallel plate method. Because of the winding arrangement, the solver solution method makes the winding capacitances at the edges higher, unlike others. For example, since the winding geometry is the same for all the secondary winding, the winding capacitance can not change with the its position.

Table 4.3: The simulation results for the transformer capacitances.

| **Winding Capacitance (pF)** | | | | **Coupling capacitance (pF)** | | | |
|---|---|---|---|---|---|---|---|
| $C_p$ | 12.754 | $C_{s11}$ | 20.82255 | $C_{p-s1}$ | 0.5329 | $C_{p-s11}$ | 0.3802 |
| $C_{s1}$ | 20.61191 | $C_{s12}$ | 36.94255 | $C_{p-s2}$ | 0.37301 | $C_{p-s12}$ | 0.36173 |
| $C_{s2}$ | 36.93404 | $C_{s13}$ | 36.96809 | $C_{p-s3}$ | 0.3035 | $C_{p-s13}$ | 0.29603 |
| $C_{s3}$ | 36.97149 | $C_{s14}$ | 36.96085 | $C_{p-s4}$ | 0.2861 | $C_{p-s14}$ | 0.28275 |
| $C_{s4}$ | 36.96426 | $C_{s15}$ | 36.96851 | $C_{p-s5}$ | 0.27999 | $C_{p-s15}$ | 0.2809 |
| $C_{s5}$ | 36.9634 | $C_{s16}$ | 36.96553 | $C_{p-s6}$ | 0.27964 | $C_{p-s16}$ | 0.28019 |
| $C_{s6}$ | 36.9634 | $C_{s17}$ | 36.96638 | $C_{p-s7}$ | 0.28319 | $C_{p-s17}$ | 0.28576 |
| $C_{s7}$ | 36.96043 | $C_{s18}$ | 36.97489 | $C_{p-s8}$ | 0.29615 | $C_{p-s18}$ | 0.30271 |
| $C_{s8}$ | 36.96511 | $C_{s19}$ | 36.94553 | $C_{p-s9}$ | 0.36356 | $C_{p-s19}$ | 0.37389 |
| $C_{s9}$ | 36.94043 | $C_{s20}$ | 20.61532 | $C_{p-s10}$ | 0.3791 | $C_{p-s20}$ | 0.5327 |
| $C_{s10}$ | 20.82213 | | | | | | |

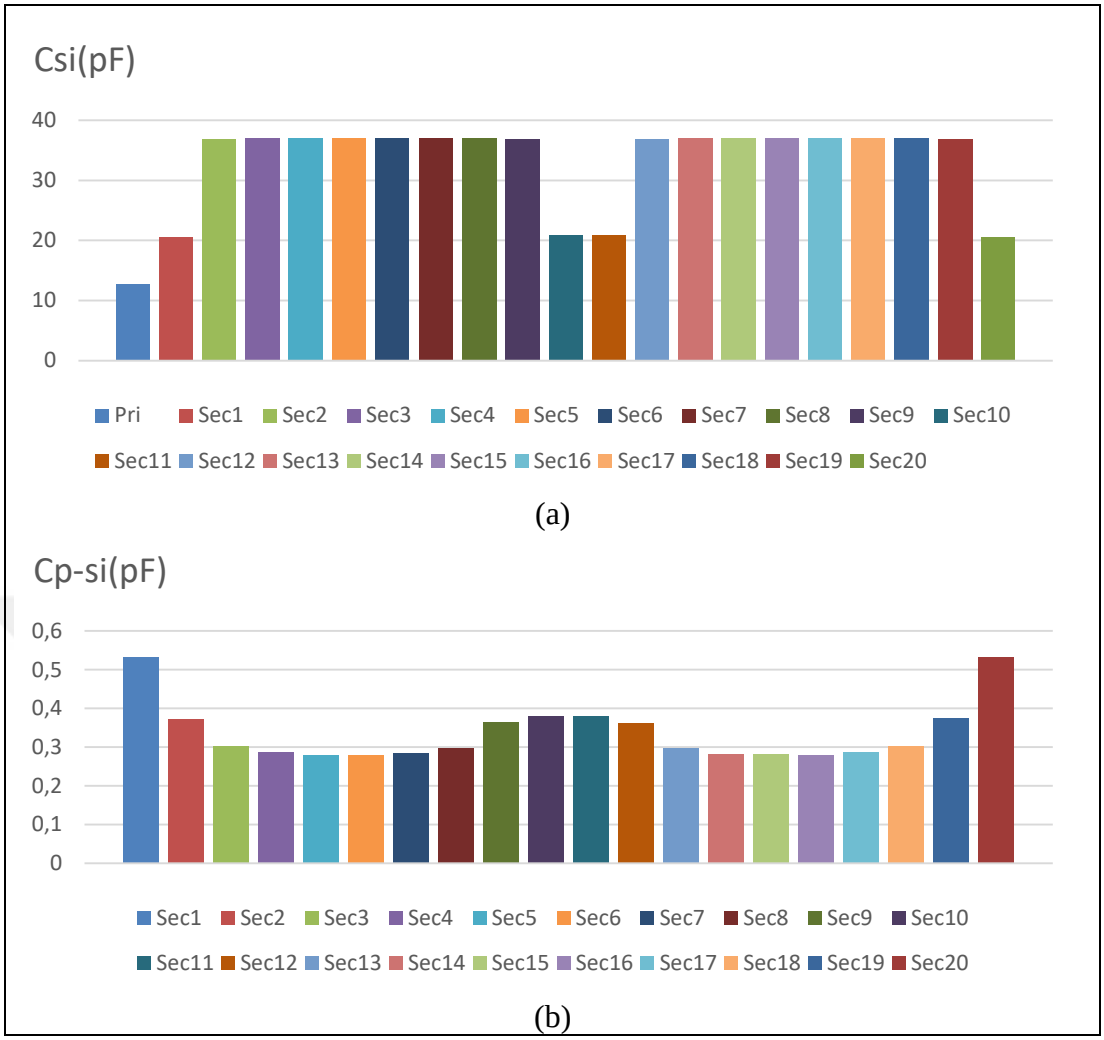


Figure 4.12: Simulation results for transformer capacitances: (a) Winding capacitances, (b) Primary-secondary coupling capacitance.

## 4.3. Summary

In this section, a winding arrangement that decreases the stray capacitance of the transformer by using a multi-winding transformer has been presented. The design concept and dividing the electric field effect into AC and DC parts have been described. The design concept for the proposed transformer is verified by FEA-based analysis. The impact of the leakage inductance, winding losses, and parasitic capacitances have also been analyzed.

The result of the simulation shows that $C_{stray}$ can be expressed as a linear function of the output number z. Thus $C_{stray}$ can be decreased significantly. The resistance of each layer is related to its location on the y-axis. The winding arrangement effect on winding loss and leakage inductance is limited.

# 5. EXPERIMENTAL RESULTS

In order to verify theoretical analysis different experiments have been performed. The objective of the first experiment has to validate the effects of the number of windings on $C_{stray}$ for a multi-winding transformer with an integrated rectifier while output is connected in series and parallel and to compare it with a multi-layer transformer. The second experiment has been performed to operate an LLC resonant converter designed with an FHA for high-voltage applications and to compare multi-layer high-voltage transformers and multi-winding transformers with integrated rectifiers.

## 5.1. The Comparison Stray Capacitance In High-Voltage Transformers

Two transformers have been designed with winding arrangements, as shown in Figure 4.1. The TR1 transformer is called a multi-layer transformer, and all the layers are connected in series before rectification. The TR2 transformer is called a multi-winding transformer with an integrated rectifier, and all adjacent layers are connected in series or parallel after the rectification circuit. The connection diagrams and prototypes for the TR1 and TR2 are shown in Figure 5.1. The transformer prototype parameters are listed in Table 5.1. The frequency response has been measured using a vector network analyzer Bode100 for all the experiments under the two conditions. The measurements have been first performed for the parallel resonance frequency and then for the open-circuit inductance from the primary side. Then, $C_{stray}$ and $C_{tr}$ have been calculated by using equation (3.15). $N_{S-Layer}$ and $Z_{S-Layer}$ are the number of turns in each layer and number of secondary windings, , respectively.

Table 5.1: The Transformer prototype parameters.

| | $N_p$ | $N_{S-Layer}$ | $Z_{S-Layer}$ | $t_s$ | $t_p$ | Air gap | $h_n$ | $h_s$ |
|---|---|---|---|---|---|---|---|---|
| **TR1** | 24 Turns | 24 Turns | 20 Layer | 0.035 mm | 0.1 mm | 1 mm | 5 mm | 1 mm |
| **TR2** | 24 Turns | 24 Turns | 20 Layer | 0.035 mm | 0.1 mm | 1 mm | 5 mm | 1 mm |

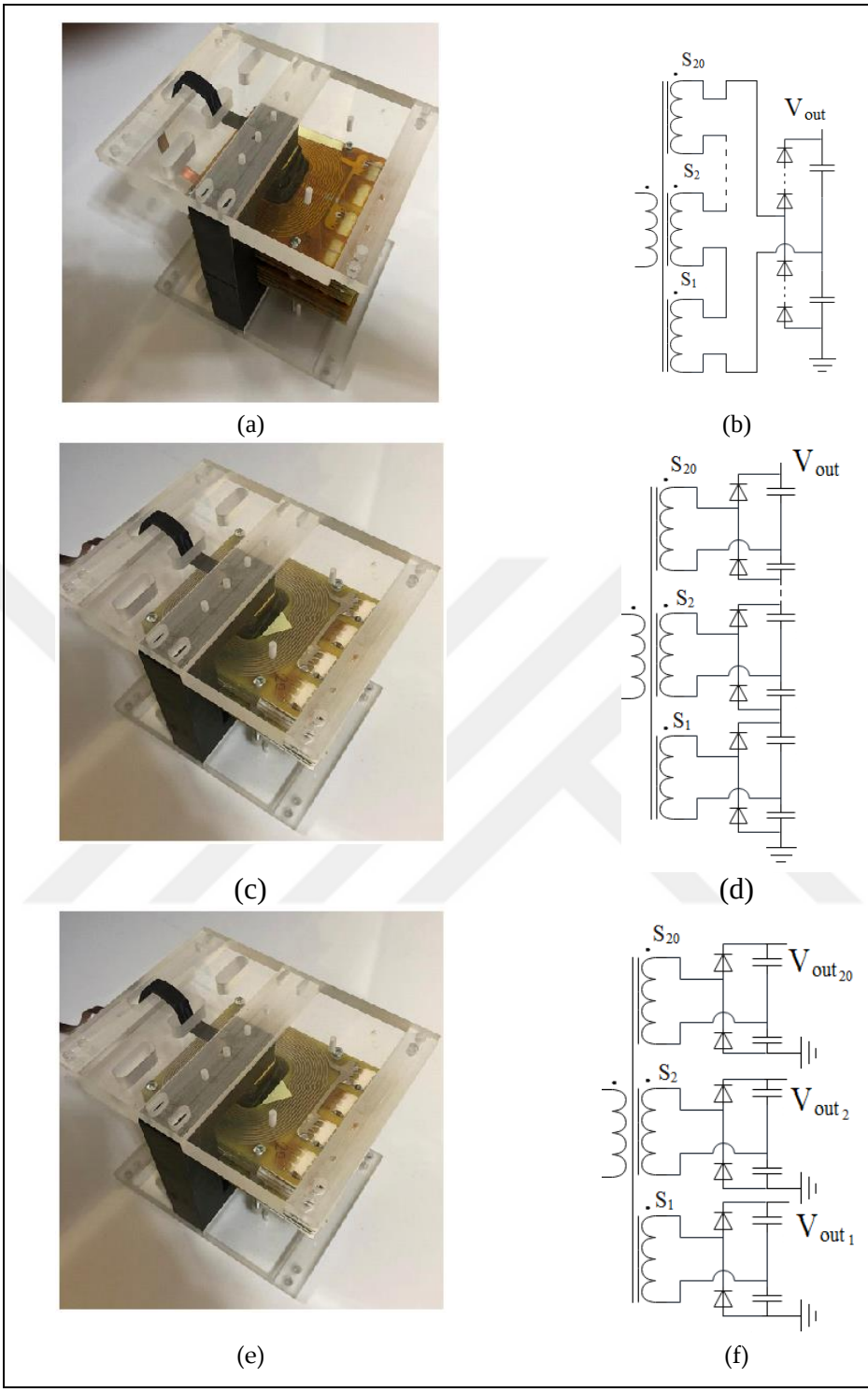


Figure 5.1: Prototype and connection diagram of TR1 (multi-layer) and TR2 (multi-winding): (a) prototype of TR1, (b) connection diagram of TR1, (c) prototype of TR2, (d) Serial connection diagram of TR2. (e) prototype of TR2, (f) Parallel connection diagram of TR2.

All measurements and calculations have been performed by increasing the number of layers from one to 20 for the TR1 with and without the rectifier connected and the TR2, respectively. $C_{tr}$ and $C_{stray}$ measurements for the TR1 are shown in Table 5.2. $C_{stray}$ calculations and results of measurements for the TR2 are shown in Table 5.3.

Table 5.2: The capacitance measurements for the TR1.

| **Layer** | **Multi-Layer Transformer (TR1)** | |
|---|---|---|
| | **Measurement $C_{tr}$ (nF)** | **Measurement $C_{stray}$ (nF)** |
| **1** | 0.111 | 0.147 |
| **2** | 0.278 | 0.413 |
| **3** | 0.435 | 0.757 |
| **4** | 0.620 | 1.098 |
| **5** | 0.864 | 1.601 |
| **6** | 1.117 | 2.160 |
| **7** | 1.283 | 2.503 |
| **8** | 1.591 | 3.251 |
| **9** | 1.890 | 3.947 |
| **10** | 2.072 | 4.618 |
| **11** | 2.415 | 5.394 |
| **12** | 2.673 | 5.962 |
| **13** | 2.944 | 6.873 |
| **14** | 3.259 | 7.755 |
| **15** | 3.609 | 8.770 |
| **16** | 3.880 | 9.303 |
| **17** | 4.384 | 10.452 |
| **18** | 4.750 | 11.467 |
| **19** | 5.216 | 12.554 |
| **20** | 5.612 | 13.540 |

Table 5.3: The capacitance calculations and measurements for the TR2.

| Layer | Multi-Winding Transformer (TR2) | | | | |
|---|---|---|---|---|---|
| | Calculated $C_{stray}$ (nF) | Serial Connected | | Parallel Connected | |
| | | Measurement $C_{stray}$ (nF) | Error (%) | Measurement $C_{stray}$ (nF) | Error (%) |
| **1** | 0.114 | 0.096 | 15.789% | 0.096 | 15.789% |
| **2** | 0.153 | 0.139 | 9.281% | 0.122 | 20.241% |
| **3** | 0.192 | 0.169 | 11.829% | 0.165 | 14.175% |
| **4** | 0.231 | 0.232 | −0.575% | 0.225 | 2.395% |
| **5** | 0.270 | 0.273 | −1.231% | 0.272 | -0.694% |
| **6** | 0.309 | 0.320 | −3.489% | 0.320 | -3.508% |
| **7** | 0.348 | 0.348 | 0.065% | 0.352 | -1.249% |
| **8** | 0.387 | 0.399 | −3.101% | 0.398 | -2.741% |
| **9** | 0.426 | 0.441 | −3.440% | 0.444 | -4.253% |
| **10** | 0.465 | 0.469 | −0.770% | 0.466 | -0.176% |
| **11** | 0.495 | 0.518 | −2.823% | 0.504 | 1.784% |
| **12** | 0.517 | 0.547 | −0.707% | 0.543 | 4.873% |
| **13** | 0.568 | 0.574 | 1.395% | 0,582 | 2.487% |
| **14** | 0.606 | 0.604 | 2.747% | 0.621 | 2.420% |
| **15** | 0.652 | 0.669 | −1.370% | 0.660 | 1.202% |
| **16** | 0.691 | 0.696 | 0.466% | 0.699 | 1.165% |
| **17** | 0,729 | 0.733 | 0.652% | 0.738 | 1.242% |
| **18** | 0,762 | 0.772 | 0.604% | 0.777 | 1.923% |
| **19** | 0,799 | 0.818 | −0.198% | 0.816 | 2.091% |
| **20** | 0,835 | 0.852 | 0.321% | 0.855 | 2.298% |

The frequency response measurements of serial and parallel connected TR2 are presented in Figure 5.2.

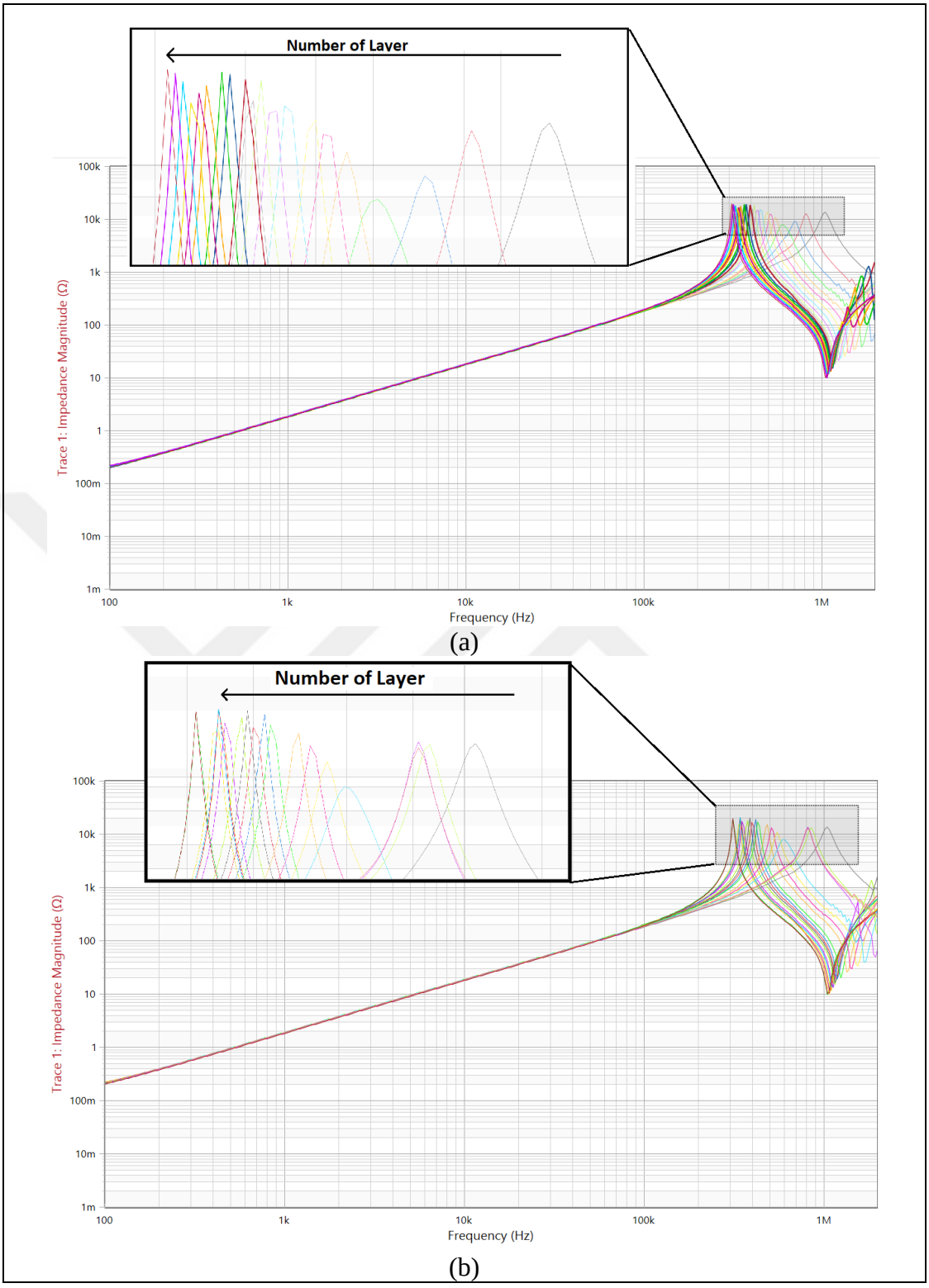


Figure 5.2: The frequency response measurement of the TR2: (a) serial connected TR2 (b) parallel connected.

The comparison of calculated and measured $C_{stray}$ for TR2 and the comparison of $C_{tr}$ and $C_{stray}$ measurements for the TR1 and TR2 are presented in Figure 5.3.

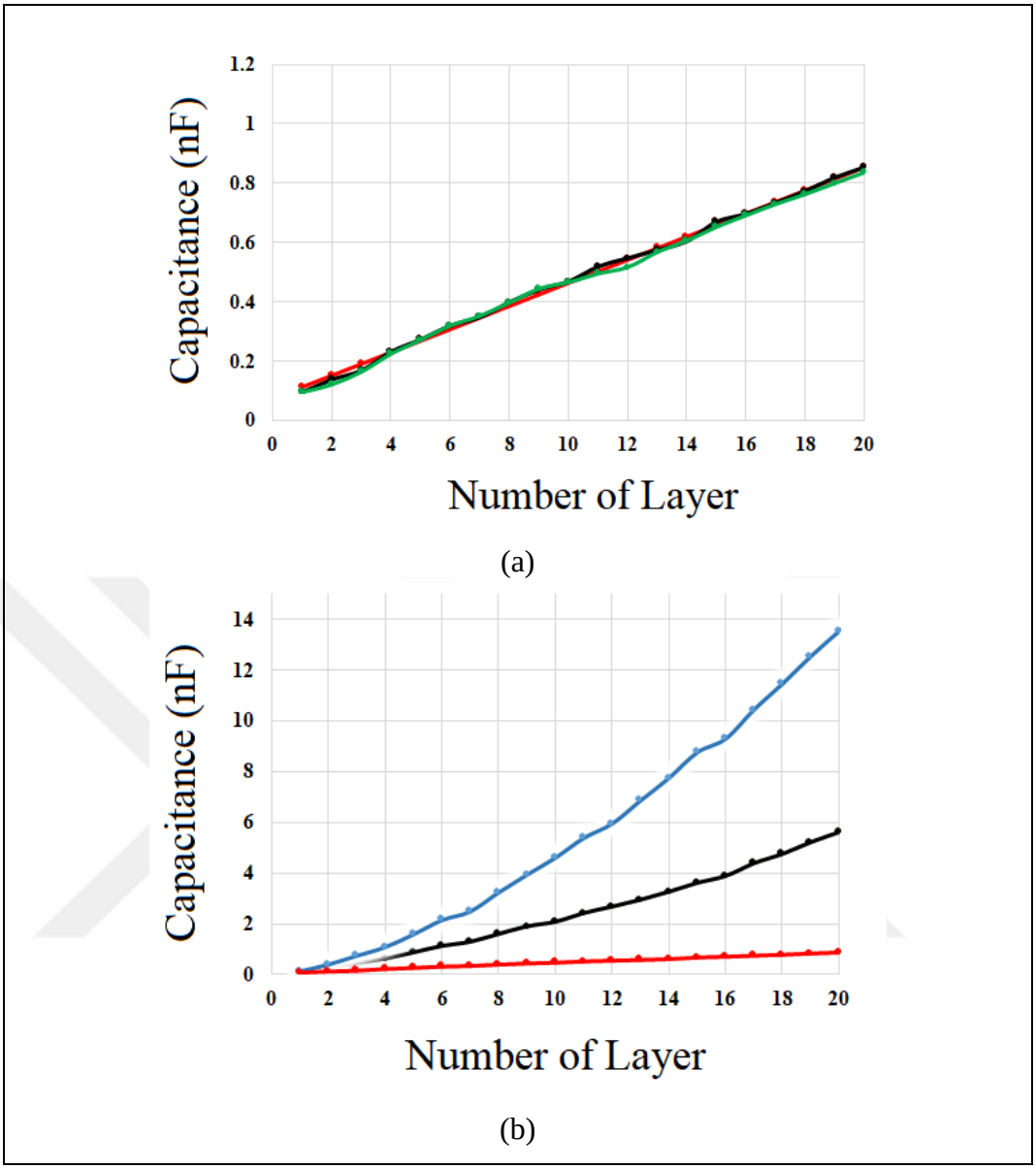


Figure 5.3: The comparison of capacitances: (a) The comparison of calculated and measured $C_{stray}$ for the TR2 (red—calculated, black—measured for serial connected, green—measured for parallel connected), (b)The comparison of $C_{tr}$ and $C_{stray}$ by layers (blue—TR1 $C_{stray}$, black—TR1 $C_{tr}$, red—TR2 $C_{stray}$).

Consequently, $C_{tr}$ and $C_{stray}$ increase exponentially for the TR1, as defined in Section 3. The effect of $C_j$ significantly increased $C_{stray}$ exponentially for the TR1. $C_{stray}$ increases proportionally with the number of layers z for the TR2 serial and parallel connection with the proposed winding arrangement, as simulated in Section 3. The frequency response measurements, while all the layers were installed on the transformers (z = 20) for the TR1 and TR2, are presented in Figure 5.4. The frequency response measurements and calculated $C_{tr}$ and $C_{stray}$ values are shown in Table 5.4.

Table 5.4: The frequency response measurements for prototypes.

| | **TR1** | **TR1** | **TR2** |
|---|---|---|---|
| $f_{paralel}$ | 120.12 kHz | 78.96 kHZ | 316.9 kHz |
| $C_{tr}$ | 5.94 nF | | |
| $C_{stray}$ | | 13.7 nF | 0.832 nF |

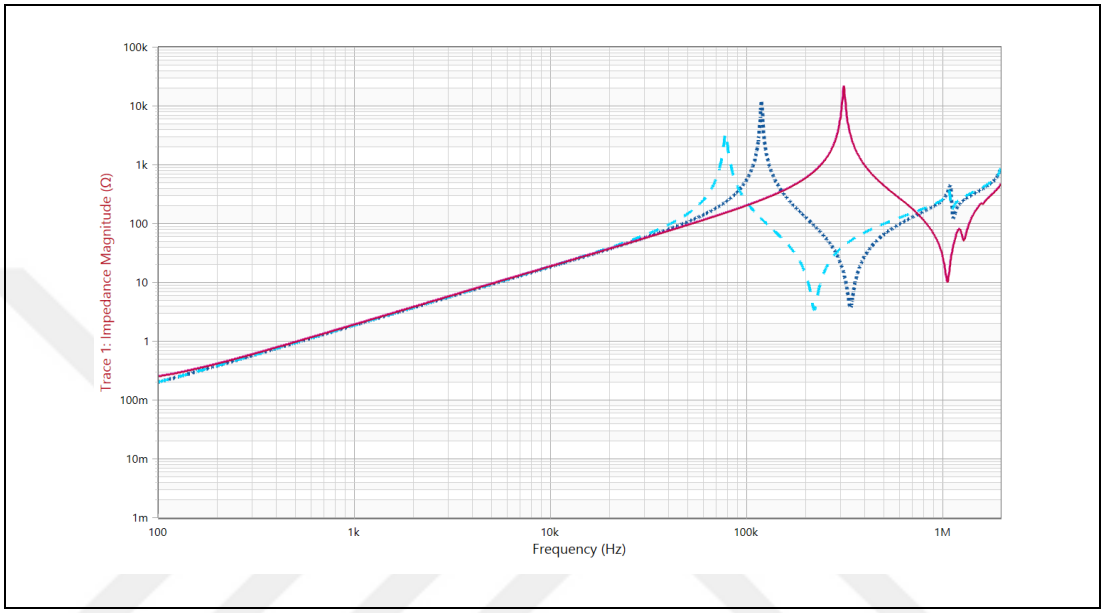


Figure 5.4: The frequency response measurement of the TR1 and TR2 for 20 layers: (dashed—TR1 $C_{tr}$, dotted—TR1 $C_{stray}$, solid—TR2).

The measurements indicated that the influence of serial or parallel connection of the layers to $C_{stray}$ is limited for TR2. Moreover, the impact of $C_{stray}$ is significantly reduced using the proposed method for the TR2. Therefore, using the proposed transformer prototype TR2 with serial connection, the LLC resonant converter is suitable for high-voltage applications.

## 5.2. LLC Resonant Converter Application

LLC resonant circuits have been designed using the FHA methodology and time domain analysis that $C_{stray}$ was not considered. An experiment has been performed to compare the LLC resonant circuits for TR1 and TR2, and all the layers were installed on the transformers. Detailed measurements are performed for the TR2. The design parameters of the LLC resonant circuit are listed in Table 5.4, and the test setup is shown in Figure 5.5.

Table 5.5: The LLC resonant converter parameters.

| Parameter | Value |
|---|---|
| $V_s$ | 360 V |
| $V_{out}$ | 12,000 V |
| $P_{out}$ | 1200 W |
| $L_r$ | 78.4 µH |
| $C_r$ | 66 nF |
| $L_m$ | 286 µH |
| $f_{res}$ | 70 kHz |
| $f_{SW}$ | 45–150 kHz |

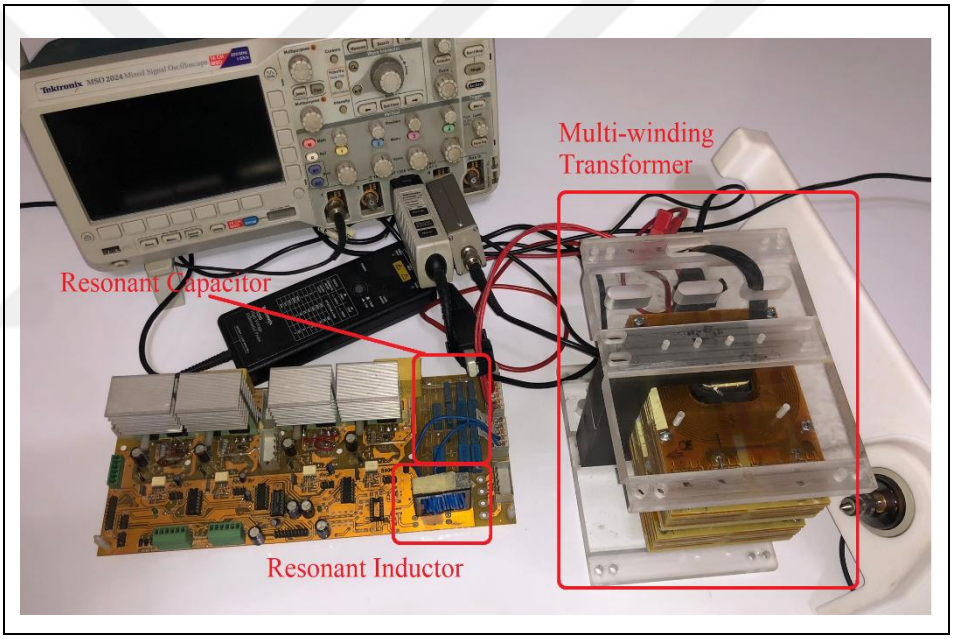


Figure 5.5: Test Setup.

Figure 5.6 shows the measurement results of the LLC resonant circuit for the TR1. The measurements show that a high $C_{stray}$ causes large distortions in the current and voltage waveforms for the entire operating frequency range. Distortions are expected under light-load conditions because of oscillations between $C_{stray}$ and $L_m$. However, a fairly high distortion has been observed at the resonant frequency. In addition, after the switching frequency reached 1,5 times the resonant frequency, the resonant tank passed to the inductive region, which is not suitable for the LLC resonant circuit and primary MOSFETs. Therefore, waveform disturbances are extremely high.


Figure 5.6: The LLC resonant converter with the TR1:
(a) full load at the resonant frequency $f_{SW}$ = 70 kHz, (b) light load at below resonant frequency $f_{SW}$=45 kHz, (c) light load at the above resonant frequency $f_{SW}$=150 kHz (ZVS loss), (d) open circuit at the above resonant frequency $f_{SW}$=120 kHz, ((1) $V_A$, (2) $I_R$, (3) $V_{OUT}$).

The LLC resonant circuit measurement at the resonant frequency, at below resonant frequency and above resonant frequency results for the TR2 are shown in Figures 5.7, 5.8 and 5.9, respectively. The measurements show that the LLC resonant converter operates by remaining in the inductive region under all load conditions and operating frequency ranges in compliance with the FHA. In addition, the LLC resonant tank progressed in the inductive region after the switching frequency reached twice the resonant frequency.

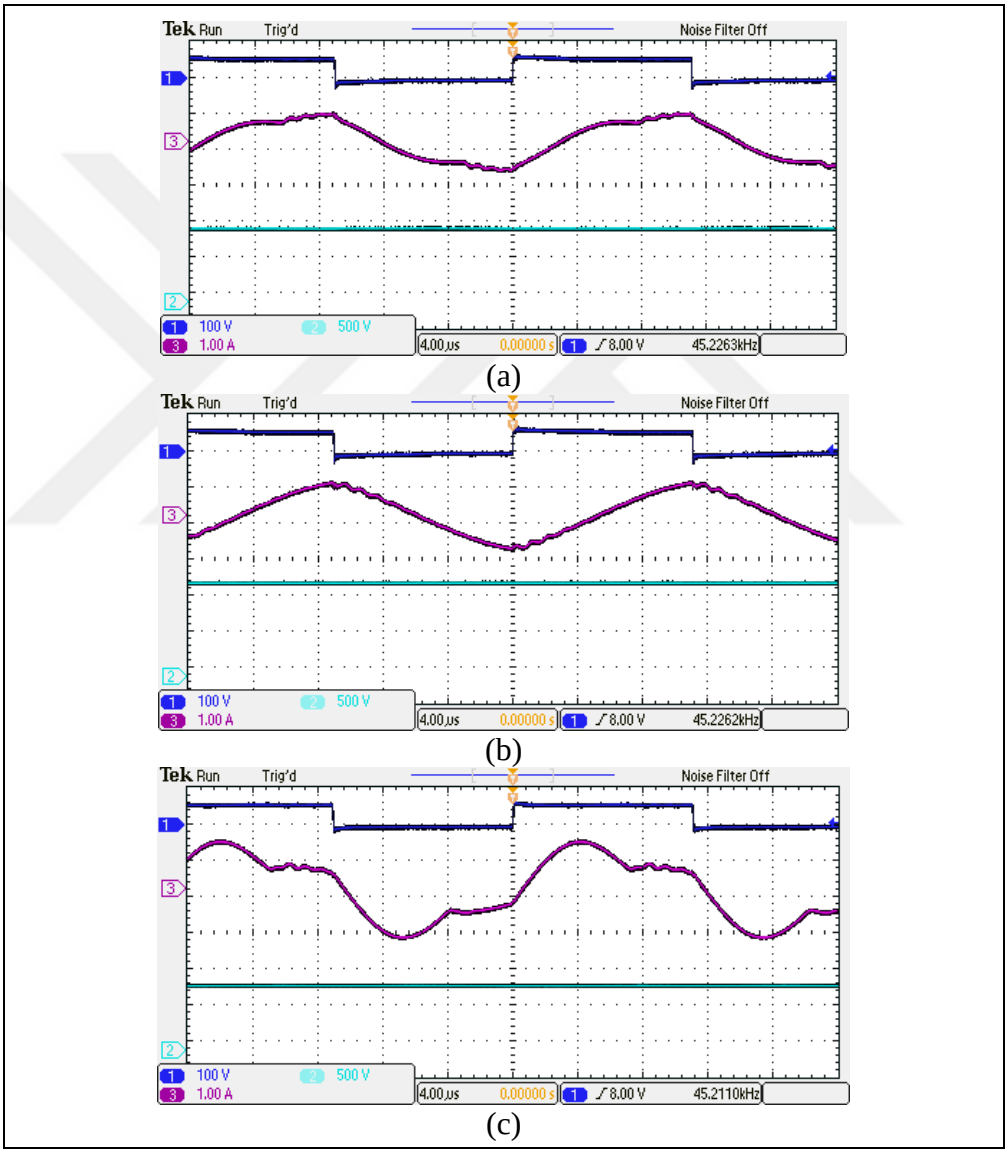


Figure 5.7: LLC resonant converter improvement for primary-side switches at below resonant frequency $f_{SW}$ = 45 kHz: (a) light load Q = 0.2, (b) open circuit, (c) heavy load Q = 0.8, ((1) $V_A$, (2) $I_R$, (3) $V_{OUT}$).

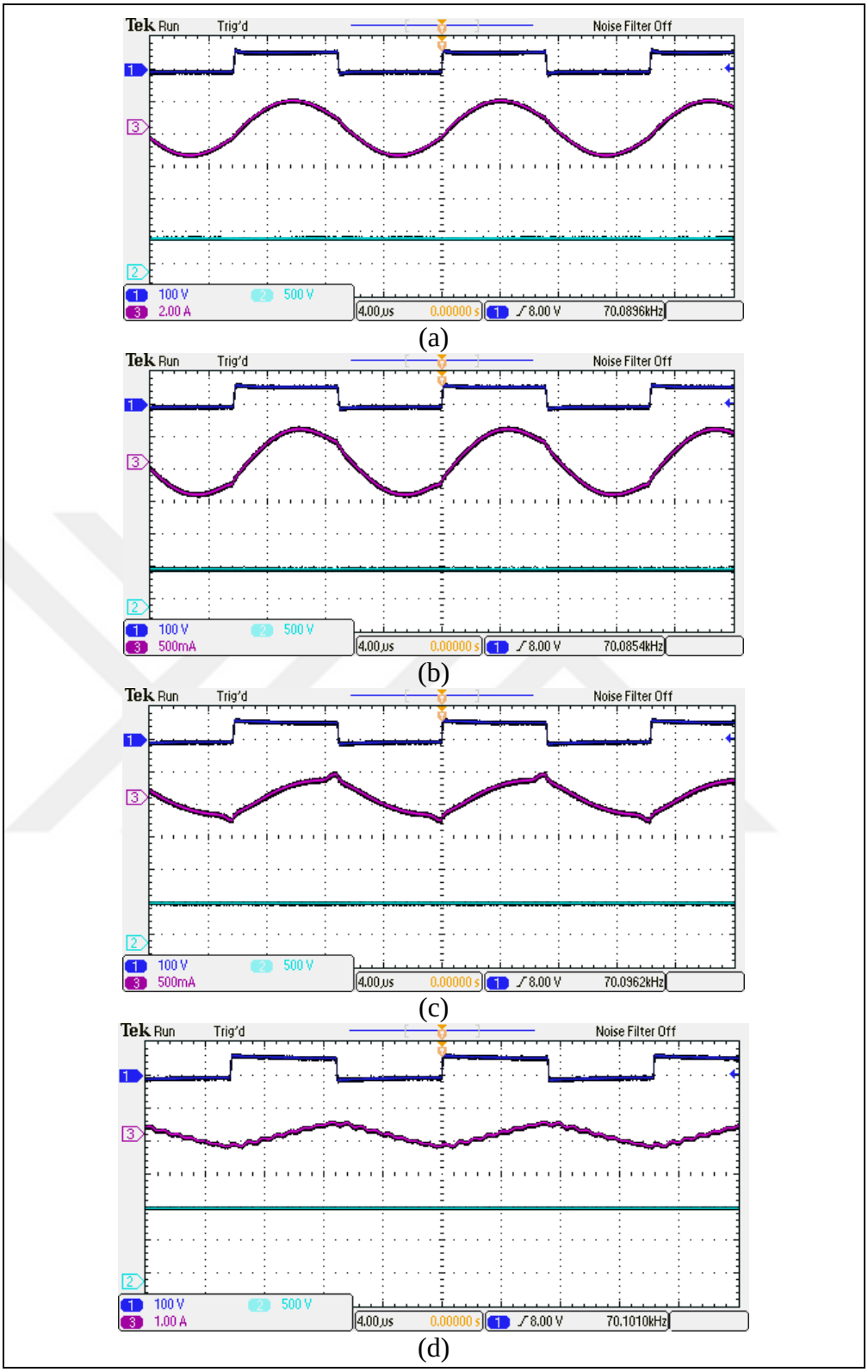


Figure 5.8: LLC resonant converter improvement for primary-side switches at the resonant frequency $f_{SW}$ = 70 kHz: (a) full load, (b) heavy load, (c) light load, (d) open circuit, ((1) $V_A$, (2) $I_R$, (3) $V_{OUT}$).

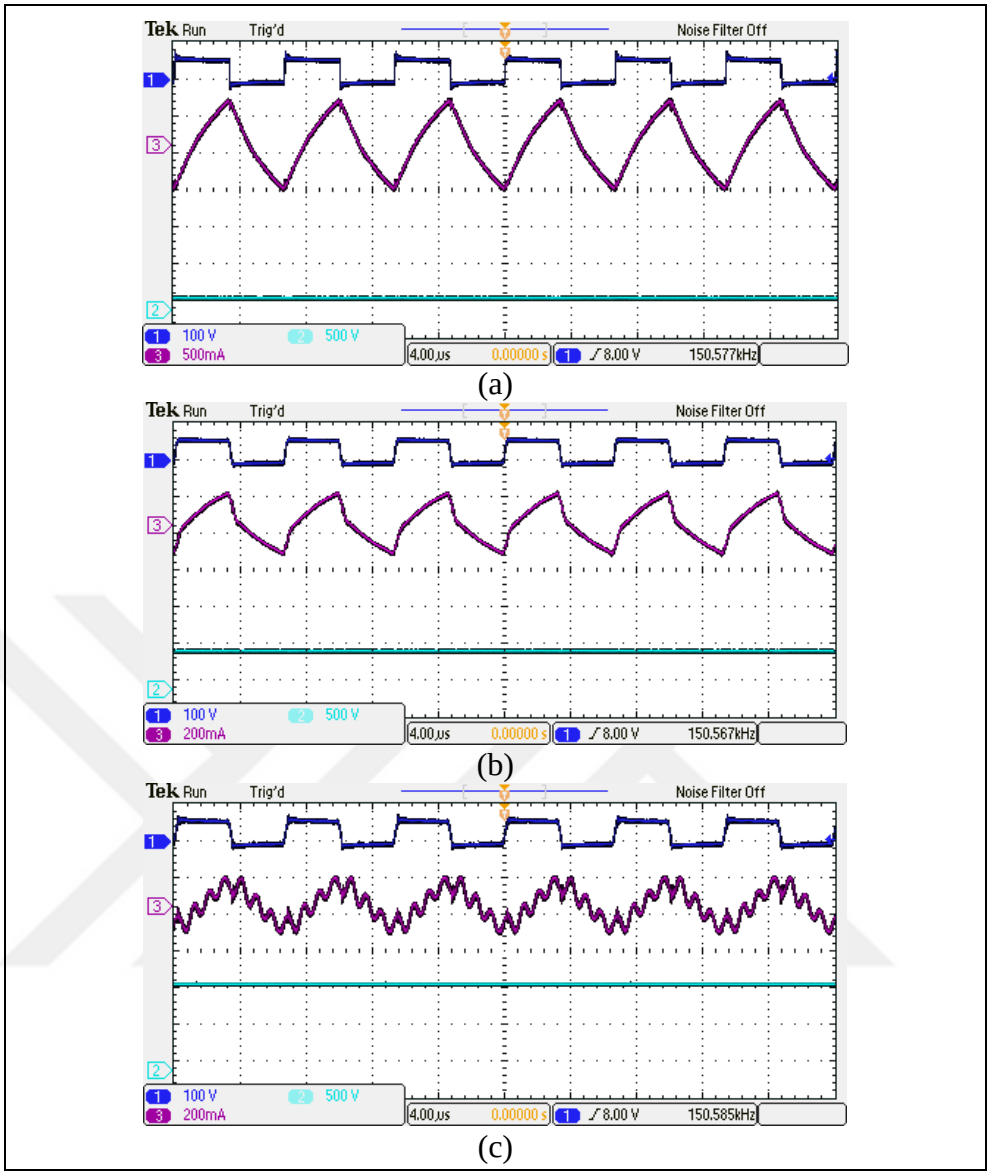


Figure 5.9: LLC resonant converter improvement for primary-side switches at the above resonant frequency $f_{SW}$ = 150 kHz: (a) full load, (b) light load Q = 0.2, (c) no load, ((1) $V_A$, (2) $I_R$, (3) $V_{OUT}$).

It is not sufficient for the designed LLC resonant circuit to operate only in the inductive region, within the operating range. However, all main switches must be provided to operate under soft-switching conditions. The measurements in Figures 5.10, 5.11 and 5.12 show that the main switches operate under soft-switching conditions in the LLC resonant circuit for the proposed TR2, the multi-output transformer with an integrated rectifier. Moreover, there are negligible disturbances of ZVS on the main switches in the secondary open-circuit condition. $V_{DS}$ and $I_{SW}$ are the drain-source voltage measurements for power switches and the main power switch current measurements, respectively.

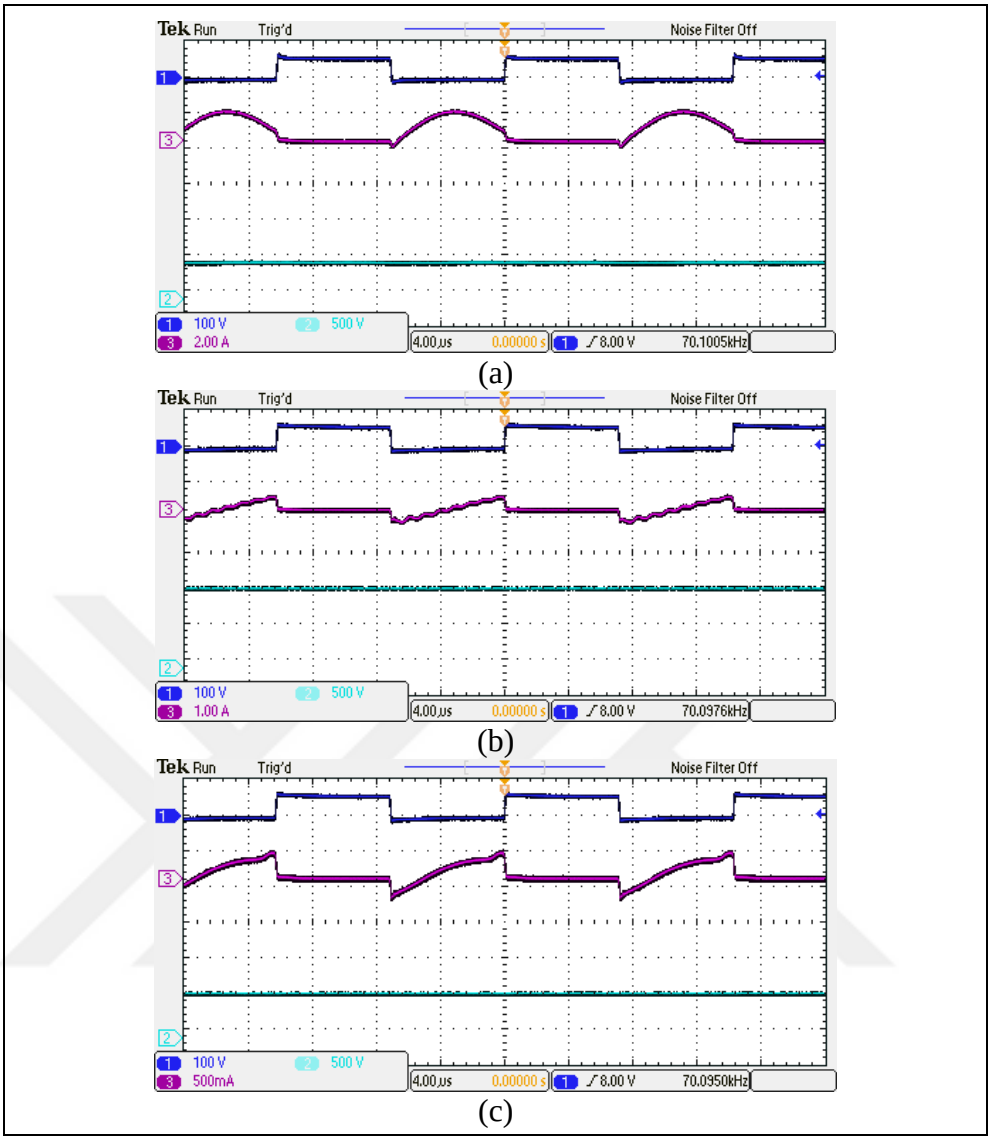


Figure 5.10: ZVS improvement for primary-side switches at the resonant frequency $f_{SW}$ = 70 kHz : (a) full load, (b) No load, (c) Light load Q=0.2 ((1) $V_{DS}$, (2) $I_{SW}$, (3) $V_{OUT}$).

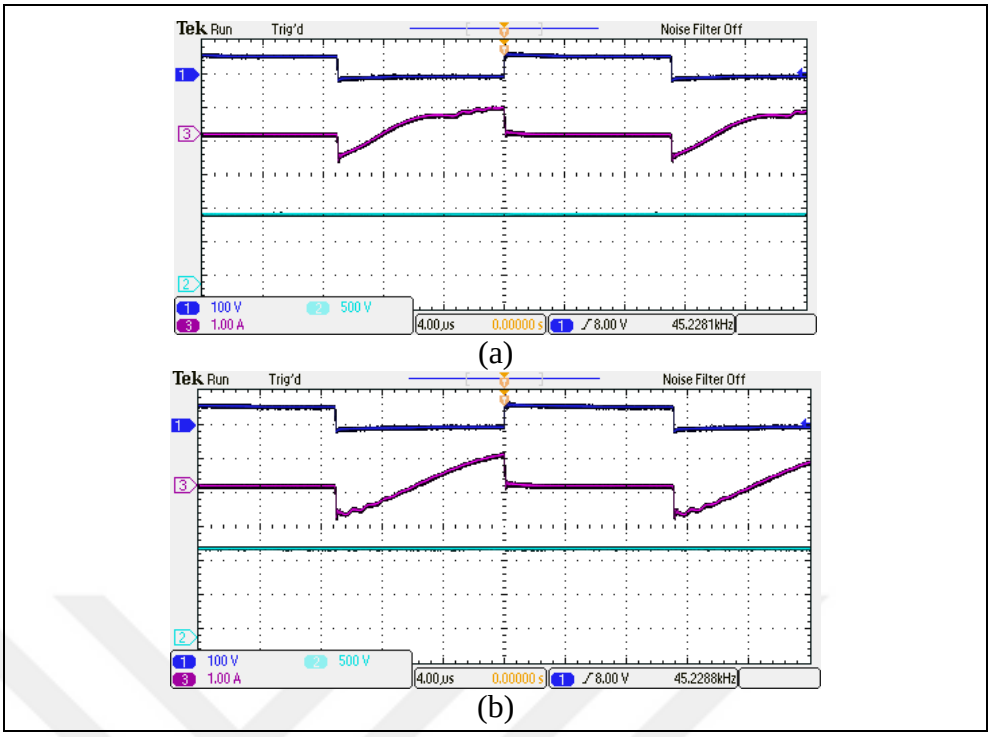


Figure 5.11: ZVS improvement for primary-side switches at below resonant frequency $f_{SW}$=45kHz: (a) Light load Q=0.2, (b) Open circuit ((1) $V_{DS}$, (2) $I_{SW}$, (3) $V_{OUT}$).

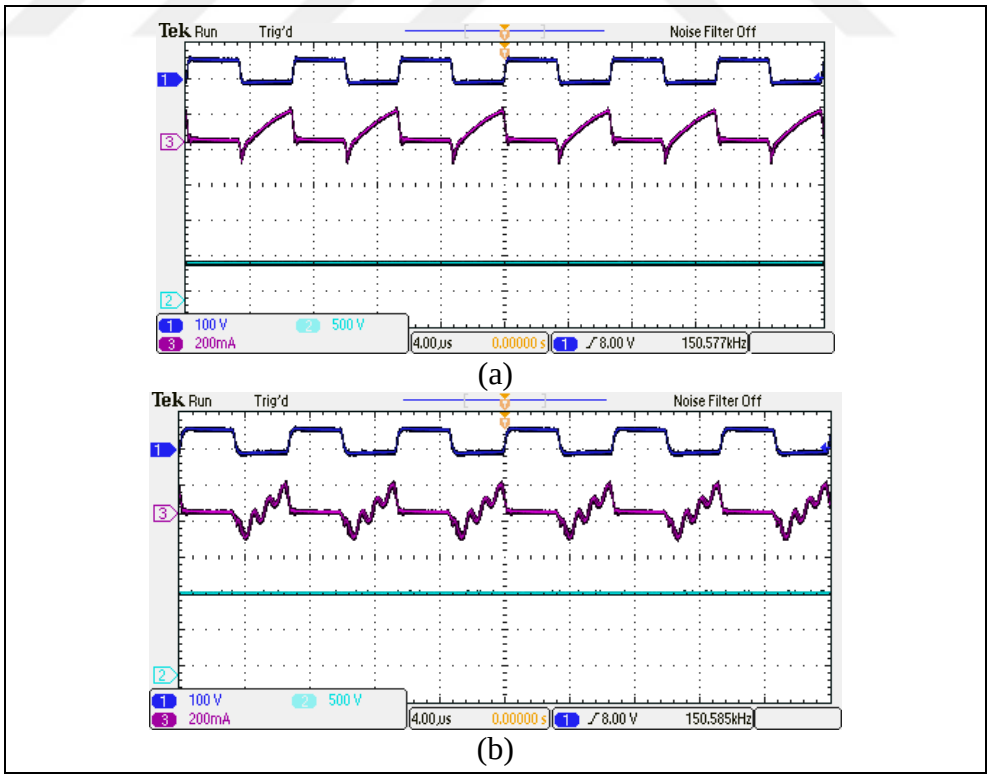


Figure 5.12: ZVS improvement for primary-side switches at the above resonant frequency $f_{SW}$=150kHz : (a) Light load Q=0.2, (b) Open circuit, ((1) $V_{DS}$, (2) $I_{SW}$, (3) $V_{OUT}$).

The LLC resonant circuit operates only in the inductive region, and the main switches operate in the ZVS condition. However, as defined in Section 3, in the multi-winding transformers, coupled inductance and coupling coefficient (k) affect power transfer in secondary windings. Leakage inductance matrix measurements are presented in Figure 5.13.

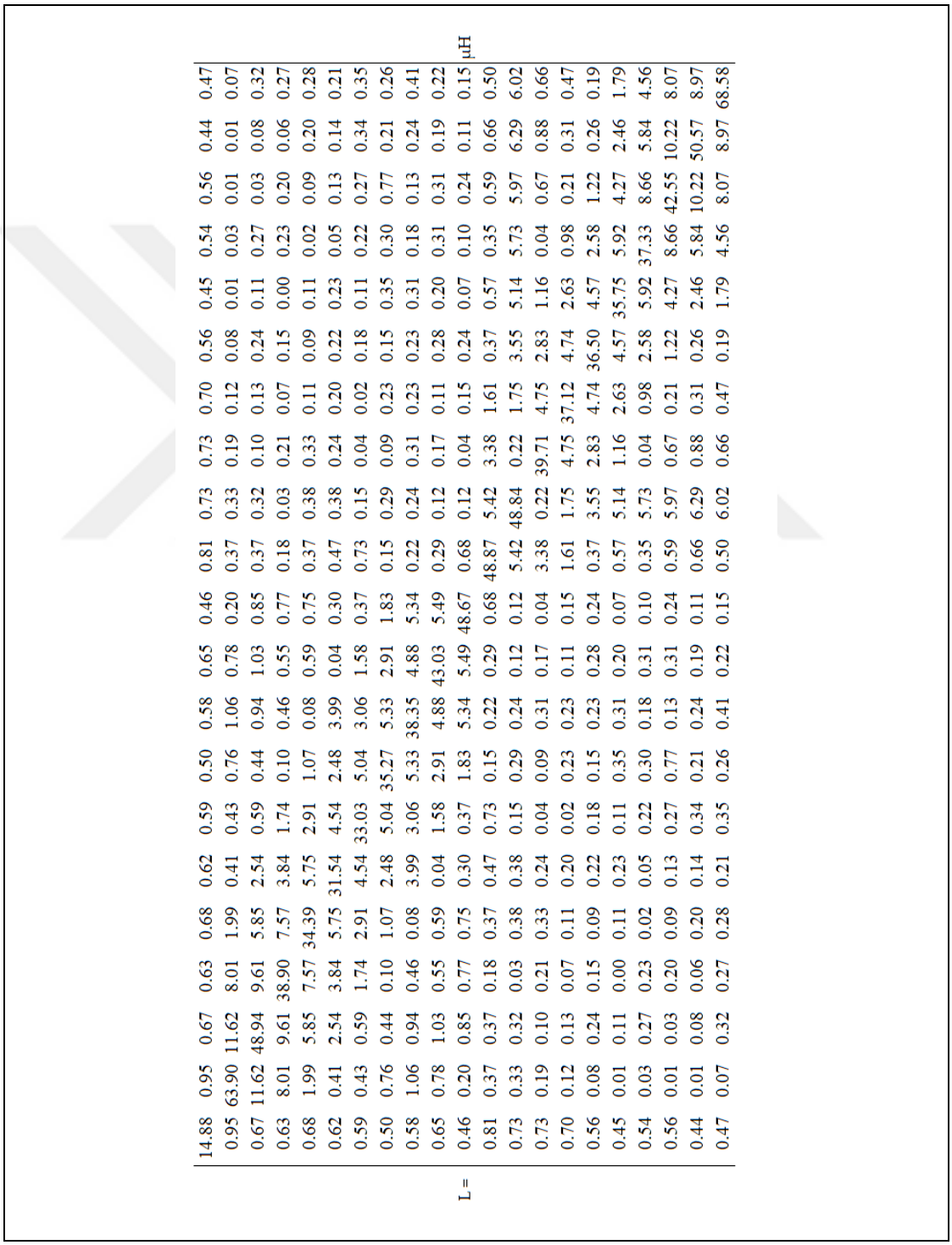


Figure 5.13: L Matrix for the TR2.

The coupling coefficient calculations for adjacent windings of the proposed winding arrangements are presented in Table 5.5. The maximum value of the coupling coefficient for primary to secondary windings is 0.03. The cross-coupling is very weak and convergent for primary to secondary windings, which is negligible. The maximum value of the coupling coefficient between adjacent secondary windings is 0.22. The rate of change for the coupling coefficient between adjacent secondary windings is quite high, but still, cross-couplings are very weak. $k_{p-si}$ is the cross-coupling coefficient between they primary winding and the secondary winding $i$. $k_{sj-si}$ is the cross-coupling coefficient between the secondary winding $j$ and the secondary winding $i$.

Table 5.6: Cross Coupling Coefficient (k) for Adjacent Layers for TR2.

| | | | | | | | |
|---|---|---|---|---|---|---|---|
| $\boldsymbol{k_{p-s1}}$ | 0.031 | $\boldsymbol{k_{p-s11}}$ | 0.030 | $\boldsymbol{k_{s1-s2}}$ | 0.208 | $\boldsymbol{k_{s11-s12}}$ | 0.111 |
| $\boldsymbol{k_{p-s2}}$ | 0.025 | $\boldsymbol{k_{p-s12}}$ | 0.027 | $\boldsymbol{k_{s2-s3}}$ | 0.220 | $\boldsymbol{k_{s12-s13}}$ | 0.005 |
| $\boldsymbol{k_{p-s3}}$ | 0.026 | $\boldsymbol{k_{p-s13}}$ | 0.030 | $\boldsymbol{k_{s3-s4}}$ | 0.207 | $\boldsymbol{k_{s13-s14}}$ | 0.124 |
| $\boldsymbol{k_{p-s4}}$ | 0.030 | $\boldsymbol{k_{p-s14}}$ | 0.030 | $\boldsymbol{k_{s4-s5}}$ | 0.174 | $\boldsymbol{k_{s14-s15}}$ | 0.129 |
| $\boldsymbol{k_{p-s5}}$ | 0.028 | $\boldsymbol{k_{p-s15}}$ | 0.024 | $\boldsymbol{k_{s5-s6}}$ | 0.141 | $\boldsymbol{k_{s15-s16}}$ | 0.126 |
| $\boldsymbol{k_{p-s6}}$ | 0.027 | $\boldsymbol{k_{p-s16}}$ | 0.019 | $\boldsymbol{k_{s6-s7}}$ | 0.148 | $\boldsymbol{k_{s16-s17}}$ | 0.162 |
| $\boldsymbol{k_{p-s7}}$ | 0.022 | $\boldsymbol{k_{p-s17}}$ | 0.023 | $\boldsymbol{k_{s7-s8}}$ | 0.145 | $\boldsymbol{k_{s17-s18}}$ | 0.217 |
| $\boldsymbol{k_{p-s8}}$ | 0.024 | $\boldsymbol{k_{p-s18}}$ | 0.022 | $\boldsymbol{k_{s8-s9}}$ | 0.120 | $\boldsymbol{k_{s18-s19}}$ | 0.126 |
| $\boldsymbol{k_{p-s9}}$ | 0.026 | $\boldsymbol{k_{p-s19}}$ | 0.016 | $\boldsymbol{k_{s9-s10}}$ | 0.120 | $\boldsymbol{k_{s19-s20}}$ | 0.137 |
| $\boldsymbol{k_{p-s10}}$ | 0.017 | $\boldsymbol{k_{p-s20}}$ | 0.015 | $\boldsymbol{k_{s10-s11}}$ | 0.014 | | |

Since the DC output current is the same for windings, the output voltage distribution (OVD) and the voltage distribution error (VDE) must be examined to ensure that power transfer is very close for all secondary windings. OVD and VDE measurements are shown in Table 5.7.

Table 5.7: OVD measurements and VDE calculations.

| Layer | OVD (V) | VDE (%) | Layer | OVD (V) | VDE (%) |
|---|---|---|---|---|---|
| **1** | 650.94 | 4.32% | **11** | 6,897.38 | −0.26% |
| **2** | 1,293.52 | 1.53% | **12** | 7,535.40 | 0.20% |
| **3** | 1,927.36 | 0.57% | **13** | 8,129.34 | −0.36% |
| **4** | 2,554.36 | 0.16% | **14** | 8,765.08 | 0.15% |
| **5** | 3,174.90 | −0.07% | **15** | 9,356.74 | −0.33% |
| **6** | 3,796.58 | −0.03% | **16** | 9,990.58 | 0.11% |
| **7** | 4,420.16 | 0.02% | **17** | 10,573.50 | −0.38% |
| **8** | 5,039.18 | −0.08% | **18** | 11,216.46 | 0.18% |
| **9** | 5,666.56 | 0.08% | **19** | 11,800.52 | −0.33% |
| **10** | 6,292.80 | 0.05% | **20** | 12,456.40 | 0.27% |

VDE is less than 5% and in the acceptable range. Secondary winding currents before the rectifier network must be evaluated to ensure that power transfer is very close for all the secondary windings. The secondary winding waveforms are given in Figure 5.14. $I_{pri}$ and $I_{seci}$ are the primary winding current measurement and the secondary winding i current measurement, respectively.

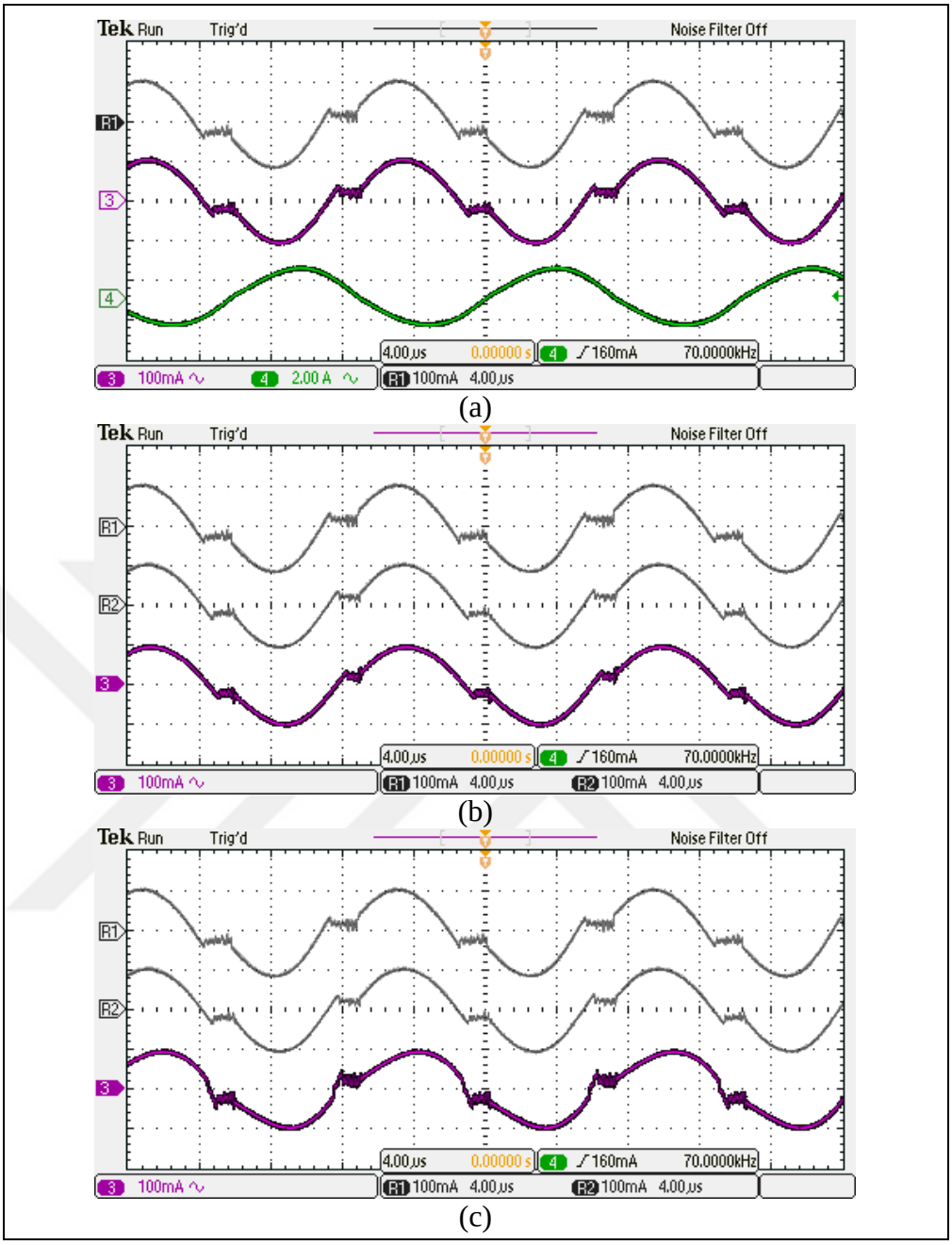


Figure 5.14: TR2 current measurements at the resonant frequency:
(a) $I_{pri}$ as green (4), $I_{sec1}$ as gray (R1), $I_{sec20}$ as purple (3),
(b) $I_{sec1}$ as gray (R1), $I_{sec20}$ as gray (R2), $I_{sec10}$ as purple (3),
(c) $I_{sec1}$ as gray (R1), $I_{sec20}$ as gray (R2), $I_{sec4}$ as purple (3).

There is a quite low phase shift observed at $I_{sec1}$, $I_{sec10}$, and $I_{sec20}$ but it is in an acceptable range. However, maximum distortion is measured at $I_{sec4}$ but it is in an acceptable range.

## 5.3. Summary

The experimental results show that:

- $C_{stray}$ increases exponentially with the number of layers z for the multi-layer transformer,
- $C_{stray}$ increases proportionally with the number of layers z for the multi-winding transformer,
- Proposed winding arrangement effects to coupling factor for the secondary windings is limited,
- $C_{stray}$ on high-voltage applications is significantly reduced using the proposed multi-winding transformer,
- The LLC resonant converter is suitable for use in high-voltage applications where $C_{stray}$ on high-voltage applications is significantly reduced,
- Since leakage transformer effects are limited, voltage distribution of the secondary winding is convergent.

# 6. CONCLUSIONS

In this thesis, an LLC resonant converter for high-voltage applications is proposed. The disruptive effect of the parasitic capacitance of the transformer and the rectifier network is analyzed. In order to adapt the LLC converter for high-voltage applications parasitic capacitance of the high-voltage transformer is reduced. A winding arrangement method for multi-winding transformer with an integrated rectifier scheme is proposed.

The analysis of the proposed multi-winding transformer is performed with FEA software Maxwell. The inductances, AC losses and capacitances of the transformer are simulated. The result of the simulation shows that the transformer parasitic capacitance can be expressed as a linear function of the the number of secondary winding. Thus the transformer parasitic capacitance can be decreased significantly.

The comparative experimental analyses are performed for the proposed multi-winding transformer and the multi-layer transformer designed in the same geometry. The result of the measurement shows that the transformer capacitance is significantly reduced by proposed multi-winding transformer.

The experimental analyses are performed using the proposed multi-winding transformer with an integrated rectifier in the LLC resonant converter. The experimental results indicate that the LLC resonant converter is suitable for high-voltage applications due to the minimized parasitic capacitances of the high-voltage transformer, which enhances its reliability. It is observed that the output voltage regulation is realized perfectly under any load condition in a wide operating range.

In future studies, the winding losses and leakage inductances should be examined. Also, high-voltage transformer efficiency and the resonant converter total losses should be investigated. A high-voltage pulse application may be realised effectively with the minimised parasitic capacitances in the high-voltage transformer.

# References


[1] Steigerwald R. L., (2001), "Power electronic converter technology", Proceedings of the IEEE, 89 (6), 890-897.

[2] Steigerwald R. L., (1988), "A comparison of half-bridge resonant converter topologies", IEEE Transactions on Power Electronics, 3 (2), 174-182.

[3] Duerbaum T., (1998), "First harmonic approximation including design constraints", INTELEC - Twentieth International Telecommunications Energy Conference, 321-328, San Francisco, CA, USA, 04-08 October.

[4] Outeiro M. T., Buja G., (2015), "Comparison of resonant power converters with two, three, and four energy storage elements", IECON- 41st Annual Conference of the IEEE Industrial Electronics Society, 1406-1411, Yokohama, Japan, 09-12 November.

[5] Johnson S. D., Witulski A. F., Erickson R. W., (1988), "Comparison of resonant topologies in high-voltage DC applications", IEEE Transactions on Aerospace and Electronic Systems, 24 (3), 263-274.

[6] Zheng J., Lu S., Li J., (2020), "LLC and LCC Analysis and Comparison of Resonant Converters", 35th Youth Academic Annual Conference of Chinese Association of Automation (YAC), 226-231, Zhanjiang, China, 16-18 October.

[7] Zhao B., Wang G., Wang D. -l., Hurley W. G., (2016), "Analysis of LCLC resonant converters for high-voltage high-frequency applications", IEEE Energy Conversion Congress and Exposition (ECCE), 1-8, Milwaukee, WI, USA, 18-22 September.

[8] Lin R. -L., Huang L-H., (2016), "Efficiency improvement on LLC resonant converter using integrated LCLC resonant transformer", IEEE Industry Applications Society Annual Meeting, 1-8, Portland, OR, USA, 02-06 October.

[9] Cheng J. H., Witulski A. F., (1998), "LLC parallel resonant converter design by scaling the LC converter", IEEE Transactions on Aerospace and Electronic Systems, 34 (3), 924-933.

[10] Biela J., Kolar J. W., (2005), "Using transformer parasitics for resonant converters - a review of the calculation of the stray capacitance of transformers", Fourtieth IAS Annual Meeting. Conference Record of the Industry Applications Conference, 3, 1868-1875, Hong Kong, China, 02-06 October.

[11] Blache F., Keradec J. -P., Cogitore B., (1994), "Stray capacitances of two winding transformers: equivalent circuit, measurements, calculation and

lowering", Proceedings of 1994 IEEE Industry Applications Society Annual Meeting, 2, 1211-1217, Denver, CO, USA, 02-06 October.

[12] Lu H. Y., Zhu J. G., Ramsden V. S., Hui S. Y. R., (1999), "Measurement and modeling of stray capacitances in high frequency transformers", 30th Annual IEEE Power Electronics Specialists Conference. Record. (Cat. No.99CH36321), 2, 763-768, Charleston, SC, USA, 01 July.

[13] Lu H. Y., Zhu J. G., Hui S. Y. R., (2003), "Experimental determination of stray capacitances in high frequency transformers", IEEE Transactions on Power Electronics, 18 (5), 1105-1112.

[14] Duerbaum T., Sauerlaender G., (2001), "Energy based capacitance model for magnetic devices", Sixteenth Annual IEEE Applied Power Electronics Conference and Exposition (Cat. No.01CH37181), 1, 109-115, Anaheim, CA, USA, 04-08 March.

[15] Dalessandro L., Cavalcante F. da S., Kolar J. W., (2007), "Self-Capacitance of High-Voltage Transformers", IEEE Transactions on Power Electronics, 22 (5), 2081-2092.

[16] Bagheri M., Vakilian M., Hekmati A., Heidarzadeh R., (2007), "Influence of Electrostatic Shielding of Disc Winding on Increasing the Series Capacitance in Transformer", IEEE Lausanne Power Tech, 1780-1784, Lausanne, Switzerland, 01-05 July.

[17] De Grève Z., Deblecker O., Lobry J., (2013), "Numerical Modeling of Capacitive Effects in HF Multiwinding Transformers—Part I: A Rigorous Formalism Based on the Electrostatic Equations", IEEE Transactions on Magnetics, 49 (5), 2017-2020.

[18] De Grève Z., Deblecker O., Lobry J., (2013), "Numerical Modeling of Capacitive Effects in HF Multiwinding Transformers—Part II: Identification Using the Finite-Element Method", IEEE Transactions on Magnetics, 49 (5), 2021-2024.

[19] Huang P., DianR., WangP., D. WangD., Liu Z., Wang Q., (2021), "Comprehensive Analysis of Electric Field Characteristics for Multi-Winding Medium Frequency Transformer", Energies, 14 (11), 3285.

[20] Farhangi B., Toliyat H. A., (2013), "Modeling isolation transformer capacitive components in a dual active bridge power conditioner", IEEE Energy Conversion Congress and Exposition, 5476-5480, Denver, CO, USA, 15-19 September.

[21] Farhangi B., Toliyat H. A., (2015), "Modeling and Analyzing Multiport Isolation Transformer Capacitive Components for Onboard Vehicular Power Conditioners", IEEE Transactions on Industrial Electronics, 62 (5), 3134-3142.

[22] Saket M. A., Shafiei N., Ordonez M., (2017), "LLC Converters With Planar Transformers: Issues and Mitigation", IEEE Transactions on Power Electronics, 32 (6), 4524-4542.

[23] Cove S. R., Ordonez M., Quaicoe J. E., (2010), "Applying Response Surface Methodology to planar transformer winding design", IEEE Energy Conversion Congress and Exposition, 2182-2187, Atlanta, GA, USA, 12-16 September.

[24] Ranstad P., Nee H. -P., (2011), "On the Distribution of AC and DC Winding Capacitances in High-Frequency Power Transformers With Rectifier Loads", IEEE Transactions on Industrial Electronics, 58 (5), 1789-1798.

[25] Dowell P. L., (1966), “Effects of eddy currents in transformer windings”, Proc. Inst. Elect. Eng., 113 (8), 1387–1394.

[26] Ferreira J. A., (1994), "Improved analytical modeling of conductive losses in magnetic components", IEEE Transactions on Power Electronics, 9 (1), 127-131.

[27] Nan X., Sullivan C. R., (2003), "An improved calculation of proximity-effect loss in high-frequency windings of round conductors", IEEE 34th Annual Conference on Power Electronics Specialist, PESC '03., 2, 853-860, Acapulco, Mexico, 15-19 June.

[28] Wojda R. P., Kazimierczuk M. K., (2013), "Analytical Optimization of Solid–Round-Wire Windings", IEEE Transactions on Industrial Electronics, 60 (3), 1033-1041.

[29] Iyer K. V., Robbins W. P., Mohan N., (2014), "Design and comparison of high frequency transformers using foil and round windings", International Power Electronics Conference (IPEC-Hiroshima 2014 - ECCE ASIA), 3037-3043, Hiroshima, Japan, 18-21 May.

[30] Iyer K. V., Robbins W. P., Mohan N., (2014), "Winding design of a high power medium frequency transformer", International Symposium on Power Electronics, Electrical Drives, Automation and Motion, 665-669, Ischia, Italy, 18-20 June.

[31] Wallmeier P., (2001), "Improved analytical modeling of conductive losses in gapped high-frequency inductors", IEEE Transactions on Industry Applications, 37 (4), 1045-1054.

[32] Pentz, D.C., Hofsajer, I.W, (2008), “Improved AC-resistance of multiple foil winding by varying of thickness of successive layers”, COMPEL Int. J. Comput. Math. Electr. Electron. Eng., 181–195.

[33] Pollock J. D., Sullivan C. R., (2005) "Modelling Foil Winding Configurations with Low AC and DC Resistance", IEEE 36th Power Electronics Specialists Conference, 1507-1512, Dresden, Germany, 16 June.

[34] Hurley W. G., Gath E., Breslin J. G., (2000), "Optimizing the AC resistance of multilayer transformer windings with arbitrary current waveforms", IEEE Transactions on Power Electronics, 15 (2), 369-376.

[35] Ouyang Z., Thomsen O. C., Andersen M. A. E., (2009), "The analysis and comparison of leakage inductance in different winding arrangements for planar transformer", International Conference on Power Electronics and Drive Systems (PEDS), 1143-1148, Taipei, Taiwan, 02-05 November.

[36] Ouyang Z., Thomsen O. C., Andersen M. A. E., (2012), "Optimal Design and Tradeoff Analysis of Planar Transformer in High-Power DC–DC Converters", IEEE Transactions on Industrial Electronics, 59 (7), 2800-2810.

[37] Aicher L. C., (1943), "A Useful Equivalent Circuit for a Five-Winding Transformer", Transactions of the American Institute of Electrical Engineers, 62 (2), 66-70.

[38] Margueron X., Keradec J. P., (2007), "Identifying the Magnetic Part of the Equivalent Circuit of n-Winding Transformers", IEEE Transactions on Instrumentation and Measurement, 56 (1), 146-152.

[39] Lambert M., Martínez-Duró M., Mahseredjian J., de León F., Sirois F.,(2014), "Transformer Leakage Flux Models for Electromagnetic Transients: Critical Review and Validation of a New Model", IEEE Transactions on Power Delivery, 29 (2), 2180-2188.

[40] de Leon F., Martinez J. A., (2009), "Dual Three-Winding Transformer Equivalent Circuit Matching Leakage Measurements", IEEE Transactions on Power Delivery, 24 (1), 160-168.

[41] Margueron X., Keradec J. -P., (2007), "Design of Equivalent Circuits and Characterization Strategy for n-Input Coupled Inductors", IEEE Transactions on Industry Applications, 43 (1), 14-22.

[42] de Leon F., Semlyen A., (1994), "Detailed modeling of eddy current effects for transformer transients", IEEE Transactions on Power Delivery, 9 (2), 1143-1150.

[43] Deswal D., de León F., (2019), "Generalized Circuit Model for Eddy Current Effects in Multi-Winding Transformers", IEEE Transactions on Power Delivery, 34 (2), 638-650.

[44] Zhang Z., He B., Hu D. -D., Ren X., Chen Q., (2019), "Multi-Winding Configuration Optimization of Multi-Output Planar Transformers in GaN Active Forward Converters for Satellite Applications", IEEE Transactions on Power Electronics, 34 (5), 4465-4479.

[45] Alvarez-Marino C., de Leon F., Lopez-Fernandez X. M., (2012), "Equivalent Circuit for the Leakage Inductance of Multiwinding Transformers:

Unification of Terminal and Duality Models", IEEE Transactions on Power Delivery, 27 (1), 353-361.

[46] Lopera J. M., Prieto M. J., Pernia A. M., Nuno F., (2003), "A multiwinding modeling method for high frequency transformers and inductors", IEEE Transactions on Power Electronics, 18 (3), 896-906.

[47] Hayes J. G., O'Donovan N., Egan M. G., O'Donnell T., (2003), "Inductance characterization of high-leakage transformers", Eighteenth Annual IEEE Applied Power Electronics Conference and Exposition, APEC '03, 2, 1150-1156, Miami Beach, FL, USA, 09-13 February.

[48] Hayes J. G., O'Donovan N., Egan M. G., (2004), "The extended T model of the multiwinding transformer", IEEE 35th Annual Power Electronics Specialists Conference (IEEE Cat. No.04CH37551), 3, 1812-1817, Aachen, Germany, 20-25 June.

[49] Pereira T., Hoffmann F., Zhu R., Liserre M., (2021), "A Comprehensive Assessment of Multiwinding Transformer-Based DC–DC Converters", IEEE Transactions on Power Electronics, 36 (9), pp. 10020-10036.

[50] Du Y., Wang G., Wang J., Bhattacharya S., Huang A. Q., (2010), "Modeling of the impact of diode junction capacitance on high voltage high frequency rectifiers based on 10kV SiC JBS diodes", IEEE Energy Conversion Congress and Exposition, 105-111, Atlanta, GA, USA, 12-16 September.

[51] Lee B. -H., Kim M. -Y., Kim C. -E., Park K. -B., Moon G. -W., (2009), "Analysis of LLC Resonant Converter considering effects of parasitic components", INTELEC 31st International Telecommunications Energy Conference, 1-6, Incheon, Korea (South), 18-22 October.

[52] Sun J., Nakaoka M., Takano H., (1997), "High-voltage transformer parasitic resonant PWM DC-DC high-power converters and their performance evaluations", ISIE '97 Proceeding of the IEEE International Symposium on Industrial Electronics, 2, 572-577, Guimaraes, Portugal, 07-11 July.

[53] Sun J., Konishi H., Ogino Y., Chu E., Nakaoka M., (2000), "Series resonant high-voltage PFM DC-DC converter with voltage multiplier based a two-step frequency switching control for medical-use X ray power generator", Proceedings IPEMC 2000. Third International Power Electronics and Motion Control Conference (IEEE Cat. No.00EX435), 2, 596-601, Beijing, China, 15-18 August.

[54] Sun J., Konishi H., Ogino Y., Nakaoka M., (2000), "Series resonant high-voltage ZCS-PFM DC-DC converter for medical power electronics", IEEE 31st Annual Power Electronics Specialists Conference. Conference Proceedings (Cat. No.00CH37018), 3, 1247-1252, Galway, Ireland, 23 June.

[55] Cavalcante F. da S., Kolar J. W., "Design of a 5 kW high output voltage series-parallel resonant DC-DC converter", IEEE 34th Annual Conference on Power

Electronics Specialist, PESC '03., 4, 1807-1814, Acapulco, Mexico, 15-19 June.

[56] Liu J., Sheng L., Shi J., Zhang Z., He X., (2009), "Design of High Voltage, High Power and High Frequency Transformer in LCC Resonant Converter", Twenty-Fourth Annual IEEE Applied Power Electronics Conference and Exposition, 1034-1038, Washington, DC, USA, 15-19 February.

[57] Piazza G. L., Alves R. L., Font C. H. I., Barbi I., (2009), "Resonant circuit model and design for a high frequency high voltage switched-mode power supply", Brazilian Power Electronics Conference, 326-331, Bonito-Mato Grosso do Sul, Brazil, 27 Sep.-01 October.

[58] Batarseh I., Liu R., Ortiz-Conde A., Yacoub A., Siri K., (1994), "Steady state analysis and performance characteristics of the LLC-type parallel resonant converter", Proceedings of 1994 Power Electronics Specialist Conference - PESC'94, 1, 597-606, Taipei, Taiwan, 20-25 June.

[59] Beiranvand R., Rashidian B., Zolghadri M. R., Hossein Alavi S. M., (2012), "A Design Procedure for Optimizing the LLC Resonant Converter as a Wide Output Range Voltage Source", IEEE Transactions on Power Electronics, 27 (8), 3749-3763.

[60] Zhao Z., Xu Q., Dai Y., Luo A., (2018), "Minimum resonant capacitor design of high-power LLC resonant converter for comprehensive efficiency improvement in battery charging application," IET Power Electronics,11 (11), 1866-1874.

[61] Lee I. -O., Moon G. -W., (2014), "The k-Q Analysis for an LLC Series Resonant Converter", IEEE Transactions on Power Electronics, 29 (1), 13-16.

[62] Yoo J.-S., Gil Y.-M., Ahn T.-Y., (2022), “Steady-State Analysis and Optimal Design of an LLC Resonant Converter Considering Internal Loss Resistance”, Energies, 15 (21), 8144.

[63] Li F., Hao R., Lei H., Zhang X., You X., (2019), “The Influence of Parasitic Components on LLC Resonant Converter”, Energies, 12 (22), 4305.

[64] Hu Z., Wang L., Wang H., Liu Y. -F., Sen P. C., (2016), "An Accurate Design Algorithm for LLC Resonant Converters—Part I", IEEE Transactions on Power Electronics, 31 (8), 5435-5447.

[65] Hu Z., Wang L., Wang H., Liu Y. -F., Sen P. C., (2016), "An Accurate Design Algorithm for LLC Resonant Converters—Part II", IEEE Transactions on Power Electronics, 31 (8), 5448-5460.

[66] Kim D. -K., Moon S., Yeon C. -O., Moon G. -W., (2016), "High-Efficiency LLC Resonant Converter With High Voltage Gain Using an Auxiliary LC

Resonant Circuit", IEEE Transactions on Power Electronics, 31 (10), 6901-6909.

[67] Xu H., Yin Z., Zhao Y., Huang Y., (2017), "Accurate Design of High-Efficiency LLC Resonant Converter With Wide Output Voltage", IEEE Access, 5, 26653-26665.

[68] Luo J., Wang J., Fang Z., Shao J., Li J., (2018), “Optimal Design of a High Efficiency LLC Resonant Converter with a Narrow Frequency Range for Voltage Regulation”, Energies, 11 (5), 1124.

[69] Azura N., Iqbal S., Taib S., (2014), "LLC resonant DC-DC converter for high voltage applications", IEEE Conference on Energy Conversion (CENCON), 90-95, Johor Bahru, Malaysia, 13-14 October.

[70] Zhang Z., Tang Z., "Pulse frequency modulation LLC series resonant X-ray power supply", International Conference on Consumer Electronics, Communications and Networks (CECNet), 1532-1535, Xianning, China, 16-18 April.

[71] Ondin U., Balikci A.,(2023), “A Transformer Design for High-Voltage Application Using LLC Resonant Converter”, Energies, 16 (3), 1377.

# BIOGRAPHY

Umut Öndin received the B.Sc. degree from Marmara University, İstanbul, in 2005. He has the M.Sc. degree from the Department of Electronics Engineering, Graduate School of Natural and Applied Sciences, Gebze Institute of Technology, in 2009. Since 2008 he works as a specialist researcher in 4 U systems ltd. His research interests include soft-switching techniques in power electronics, resonant circuit dc-dc converters, photovoltaic inverters.

# APPENDICES

## APPENDIX A: List of publications during this study

Ondin U., Balikci A.,(2023), “A Transformer Design for High-Voltage Application Using LLC Resonant Converter”, Energies, 16 (3), 1377.